Design of a Thermal Contact Liquid Cooling System for Military Server Electronics

by

Ali C. Kheirabadi

Submitted in partial fulfilment of the requirements
for the degree of Master of Applied Science

at

Dalhousie University
Halifax, Nova Scotia
November 2016

Table of Contents

List of Tables

List of Figures

Abstract

The objective of this project was to design and experimentally evaluate a thermal contact liquid cooling system for military applications. The proposed system replaces fluidic connectors found in conventional water cooling systems with a thermal contact heat exchanger. This approach enhances reliability by eliminating leakage risks; however, it also undermines thermal performance by adding thermally resistive heat transfer interfaces. Experiments were conducted to quantify the downgraded thermal performance and to establish whether it is a viable trade-off for enhanced reliability. An experimental setup was constructed in order to simulate heat generation by a single processor. Results showed that the proposed system requires inlet water as warm as 53.2 ºC at a maximum heat load of 300 W. For comparison, it was also shown that a conventional water cooling system would incur refrigeration cost savings of 30 % relative to the proposed system at ambient temperatures sufficiently higher than 50 ºC.

List of Abbreviations and Symbols Used

a	Geometric mesh sequence scaling factor (m)
A_{hs}	Heat spreader area (m^2)
A_r	Ratio of unit cell base area to total heatsink or heat exchanger base area
A_s	Convective heat transfer surface area (m^2)
c_p	Specific heat capacity (J/kg·K)
D_h	Hydraulic diameter (m)
h_1	Enthalpy at refrigeration cycle location 1 (J/kg·K)
h_{2s}	Isentropic enthalpy at refrigeration cycle location 2 (J/kg·K)
H_{ch}	Heatsink or heat exchanger channel height (m)
h_{eff}	Effective heat transfer coefficient ($W/m^2 \cdot K$)
h_{hs}	Heat sink heat transfer coefficient ($W/m^2 \cdot K$)
I	Current (A)
k	Thermal conductivity (W/m·K)
L_{ch}	Heatsink or heat exchanger channel length (m)
N_{ch}	Number of channels in heat sink or heat exchanger plates
N_{Ew}	Number of mesh elements along channel widths
N_f	Number of fins in heatsink or heat exchanger
P	Pressure (Pa)
q	Heat load or rate of heat generated by the heat source (W)
Q	Volumetric flowrate (m^3/s)
Q_{ext}	Volumetric flowrate within the external loop (m^3/s)
Q_{hs}	Volumetric flowrate through heatsink in numerical simulations (m^3/s)
q_{in}	Rate of heat transferred to fluid from heat source (W)
Q_{int}	Volumetric flowrate within the internal loop (m^3/s)
q_{loss}	Rate of heat loss to surroundings from heat source (W)
q_{out}	Rate of heat transferred through thermal contact heat exchanger (W)
q_{pump}	Pump heat load (W)
q_{source}	Rate of heat generated by heat source in numerical simulations (W)
q_{total}	Total rate of heat generation in numerical simulations (W)

r	Geometric mesh sequence common ratio
R_{chf}	Ratio of channel width to fin width
Re	Reynolds number
R_{hs}	Heatsink thermal resistance (K/W)
R_{TCHx}	Thermal resistance of thermal contact heat exchanger (K/W)
R''_{TIM}	Thermal resistance of thermal interface material ($K \cdot m^2/W$)
R_{sys}	Overall thermal resistance of thermal contact liquid cooling system (K/W)
T	Temperature (K)
T_{air}	Ambient air temperature (K)
t_b	Heatsink or heat exchanger base thickness (m)
$T_{in,ext}$	System inlet temperature or external heat exchanger inlet temperature (K)
$T_{in,hs}$	Heatsink inlet temperature (K)
$T_{in,int}$	Internal heat exchanger inlet temperature (K)
T_{out}	Outlet temperature in numerical simulations (K)
$T_{out,ext}$	External heat exchanger outlet temperature (K)
$T_{out,int}$	Internal heat exchanger outlet temperature (K)
T_w	Maximum wall temperature or heated surface temperature (K)
t_{source}	Heat source thickness in numerical simulations (m)
u	Fluid velocity in the x direction (m/s)
v	Fluid velocity in the y direction (m/s)
V	Voltage (V)
$V_{in,ext}$	External heat exchanger inlet velocity (m/s)
$V_{in,hs}$	Heatsink inlet velocity (m/s)
$V_{in,int}$	Internal heat exchanger inlet velocity (m/s)
V_{out}	Outlet velocity in numerical simulations (m/s)
$V_{out,ext}$	External heat exchanger outlet velocity (m/s)
$V_{out,int}$	Internal heat exchanger outlet velocity (m/s)
w	Fluid velocity in the z direction (m/s)
W_b	Overall heatsink or heat exchanger width (m)
W_{ch}	Heatsink or heat exchanger channel width (m)
W_f	Heatsink or heat exchanger fin width (m)

$\dot{W}_{pump}$	Pumping power (W)
w_r	Refrigeration cycle compressor work ratio (%)

Greek symbols

δ	Represents the uncertainty or error in a variable
Δ	Represents the relative change in a particular variable
μ	Dynamic viscosity (Pa·s)
ρ	Density (kg/m^3)

Acronyms

CDU	Coolant distribution unit
CMOS	Complementary metal oxide semiconductor
CRAC	Computer room air conditioning
CRAH	Computer room air handling
FPHE	Flat plate heat exchanger
LHP	Loop heat pipe
RDHx	Rear door heat exchanger
SCHx	Side car heat exchanger
TCHx	Thermal contact heat exchanger
TIM	Thermal interface material

Acknowledgements

First and foremost, I am immeasurably grateful to my supervisor Dominic Groulx for offering a perfect balance of support and autonomy to myself and all of his graduate students. It is not just technical expertise with which his students walk way, but also an unparalleled work ethic that will never fade.

I am also thankful to my committee members Dr. Robert Bauer and Dr. Kamal El-Sankary for their efforts in aiding me to improve this work. This appreciation is extended to Dr. Andrew Warkentin and Dr. Adam Donaldson for their voluntary support and assistance in dealing with certain technical aspects of this project.

Finally, I am indebted to my office mates with whom I've had the pleasure of collaborating and associating over the past two years. Ben, Louis, Maha, Moe, Ral, Tousif, Florent, Jonas, Azad, and Tanguy, thank you.

Chapter 1 - Introduction

The following body of work outlines the conception, design, and evaluation of a thermal contact liquid cooling solution for remote military data centers. The specific direction of research was established based upon guidance and requirements provided by Raytheon Canada in regards to a new generation of ship self-defence radar systems considered for future development.

1.1 Thermal Management in Data Centers

In the broadest sense of the word, a data center is a facility whose primary function is to process, store, and communicate digital information (Geng, 2015). These facilities exist all over the world in a spectrum of sizes and arrangements, each fulfilling a unique purpose in society. On one end of this spectrum are server rooms no larger than 500 ft^2 containing less than a few hundred servers (Geng, 2015). These facilities may be tasked with local data handling or security operations for businesses, government organizations, and academic institutions. On the other end of the spectrum are enterprise-class data centers larger than 5000 ft^2 containing several thousand individual servers (Geng, 2015). These facilities may be employed by multinational corporations, such as Google, Facebook, or Amazon, who offer online services to an international customer base. Regardless of their scale and capacity, data centers will play an increasingly vital role in the 21st century as the dependence of social, economic, political, and military functions upon digital information intensifies (Geng, 2015; Kant, 2009).

One of the major challenges of data center operation is thermal management of electronic components (Garimella et al., 2012). Simply put, all heat generated by server electronics must be removed from the facility and dissipated to the atmosphere in order to maintain component temperatures below acceptable limits (Kheirabadi & Groulx, 2016b). The most widely implemented solution for achieving this since the 1990s has been air cooling and this has primarily been due to the emergence of low power complementary metal oxide semiconductor (CMOS) technology (Geng, 2015). Although it is a very convenient and practical solution, air cooling relies heavily upon vapor-compression processes and thus appropriates a large portion of data center energy consumption; roughly

one third of total data center power usage (Garimella et al., 2012; Geng, 2015; Zhang et al., 2014).

Moreover, server manufacturers are continuously adopting newer generations of processors that offer improved computational performance and capabilities; thus generating larger amounts of heat within denser packaging (Garimella et al., 2012). This further exacerbates the challenge of thermal management by not only increasing the required facility cooling load, but also necessitating lower air temperatures and higher flowrates to deal with rising heat fluxes; all of which increase the strain and cost of vapor-compression cooling (Kheirabadi & Groulx, 2016b). Altogether, these trends have motivated a vast amount of research dealing with alternative liquid cooling strategies aimed at reducing the energy consumption, operating cost, and overall carbon footprint of the world's data centers (Kheirabadi & Groulx, 2016b).

1.2 The Supplementary Problems of Military Data Center Cooling

The primary objective of this research project was to develop a liquid cooling solution that is suitable for remote military data centers. These facilities may consist of server rooms onboard ships, aircraft, and ground vehicles, or server rooms located within remote military bases. Regardless of the context, there are two factors that render military data centers distinct from other facilities: environmental conditions and reliability constraints.

Military environments are often subject to extreme temperatures (Johnston et al., 2008). Raytheon Canada has suggested atmospheric temperatures as high as 50 °C and as low as -40 °C for military applications. One of the major objectives of this project was to minimize cooling costs at the higher end of this spectrum. In general, warmer climates increase the power requirement and cost of vapor-compression cooling. As atmospheric temperatures rise, heat must be transferred from a lower temperature coolant to a higher temperature environment. Maximizing coolant temperatures, which minimizes dependency upon vapor-compression cooling, is therefore an effective method for achieving cost reductions in warmer climates. Additionally, server rooms located onboard ships, aircraft, and ground vehicles are subject to fluctuating orientations and accelerations (Brown, 2003; Geisler & Straznicky, 2004); these conditions will have an impact on cooling solutions that are driven by gravity. Finally, military environments may harbor

contaminants such as salt, humidity, dust, and other particulate matter from which components and coolants must be shielded (Geisler & Straznicky, 2004).

Military and defense electronics are subject to harsh reliability constraints as system failures or blackouts may culminate in loss of human lives or undermine national security (Suhir, 2013). As a result, it is a requirement that such systems remain operational 100 % of the time with absolutely no interruptions. In order to meet such demands, individual servers and their electronic components must be hot swappable with limited maintenance requirements and absolutely no risk of leakage. Hot swapping is the process of replacing faulty electronic components or servers while the overall system remains operational. In consequence, the cooling system must also remain active while such replacements are taking place; thus ensuring heat dissipation from operational subsystems while faulty subsystems are being hot swapped.

The research presented in this thesis was motivated by the fact that cooling strategies capable of tackling these environmental and reliability constraints have not been present in existing research or industry based literature.

1.3 Thesis Objectives and Outline

This section outlines the various stages undertaken throughout this project in order to deliver the following research and design objectives:

- To identify a cooling strategy ideal for military applications
- To design a specific embodiment of such a cooling system
- To numerically and experimentally evaluate its performance
- To recommend methods of industry implementation

The first stage of this project involved a thorough review of existing and proposed cooling technologies presented by both the research community and members of industry. This review included qualitative and quantitative comparisons between these technologies; thus clearly outlining the benefits and drawbacks of each cooling solution. Based upon the conclusions of this review, the ideal cooling solution for military data centers was conceived and justified. A literature review pertaining specifically to the proposed solution was then conducted.

The second stage involved numerical design and optimization of the proposed cooling system. The aim here was to predict performance characteristics with varying

operating conditions, material properties, and dimensions; thus ensuring a robust and efficient design for subsequent experimental work. Moreover, the numerical model used will serve as an effective design tool for future studies.

The third stage involved experimental evaluation of the proposed cooling solution. The aim here was to quantify its heat transfer and flow characterises at various operating conditions and configurations and to compare its performance to conventional air and liquid cooling strategies. More specifically, it was expected that the proposed cooling system would underperform relative to a conventional water cooling system. The purpose of experimentation was to quantify this relative deficiency and to ascertain whether it would be a practical trade-off for the added reliability.

Since the experimental setup was designed to facilitate measurement and testing, the final stage involved recommending various design configurations suitable for industry implementation. These recommendations included potential methods for integrating the new technology into existing server rack designs as well as combining the new technology with existing cooling systems in order to further augment its capabilities.

Chapter 2 - Literature Review: Existing Cooling Technologies

In order to select the ideal cooling approach for remote military applications, a thorough review of available and proposed cooling strategies in server cooling applications was performed. This review focused upon qualitative and quantitative comparisons between these technologies. Heat transfer and flow characteristics from various experimental studies were compared using a set of fixed evaluation criteria. Industry examples were also examined in order to identify difficulties related to implementation, maintenance, and reliability. This review process culminated in a review article published in *Applied Thermal Engineering* titled *Cooling of server electronics: A design review of existing technologies* (Kheirabadi & Groulx, 2016b). The current chapter summarizes the relevant conclusions of this work so as to validate the cooling solution selected for experimental study. For a more detailed discussion on the various strategies considered, the reader is directed to the aforementioned review article.

2.1 Server Power Trends and Thermal Limits

Prior to discussing existing cooling strategies, a brief summary is presented on server power trends and heat loads. Major heat generating electronics within servers include processors, memory modules, voltage regulators, chipsets, and power supplies (ASHRAE, 2012). With respect to thermal management, processors are deemed the most problematic of these components due to their high heat flux. They account for as much as 50 % of total server power consumption while taking up minimal server area (ASHRAE, 2012).

ASHRAE predicts that, by the year 2020, the rate of heat generated by a single general purpose processor will range between 140 and 190 W while the heat load of a single high performance computing (HPC) processor will range between 210 and 300 W (ASHRAE, 2012). Due to these trends, the cooling solution proposed in this work was evaluated at heat loads up to 300 W. Additionally, the maximum allowable temperature for server components is typically recommended to be 85 °C (Ebrahimi et al., 2014). Both of these constraints are crucial for evaluating a given cooling system and their significance within the current work is addressed in subsequent chapters.

2.2 Existing Technologies

At the current state of available technologies, there are four cooling solutions that may be considered practical in server cooling applications: air cooling, single-phase water cooling, heat pipe cooling, and open bath immersion cooling. Their major benefits and drawbacks, as they relate to the current work, are discussed below. A quantitative comparison between the heat transfer capabilities of these strategies is provided in the next chapter.

2.2.1 Air Cooling

Air cooling is currently the most widely implemented cooling solution in data centers around the world primarily due to its ease of implementation and low maintenance requirements (Tuma, 2010). The process of data center air cooling is visualized in Fig. 2.1. Heated facility air is cooled by either computer room air conditioning or air handling units (CRAC/CRAH) and delivered to allocated cold aisles through an underfloor plenum (Geng, 2015). The difference here is that CRAH units utilize water-air heat exchangers to cool facility air while CRAC units use refrigerant-filled evaporators (Geng, 2015). At the server level, all electronics are cooled through direct forced air convection with heat sink attachments required for high heat flux components (Geng, 2015). Dedicated server fans drive cold aisle air through individual servers and release the heated exhaust air back into the facility through allocated hot aisles (Fakhim et al., 2011).

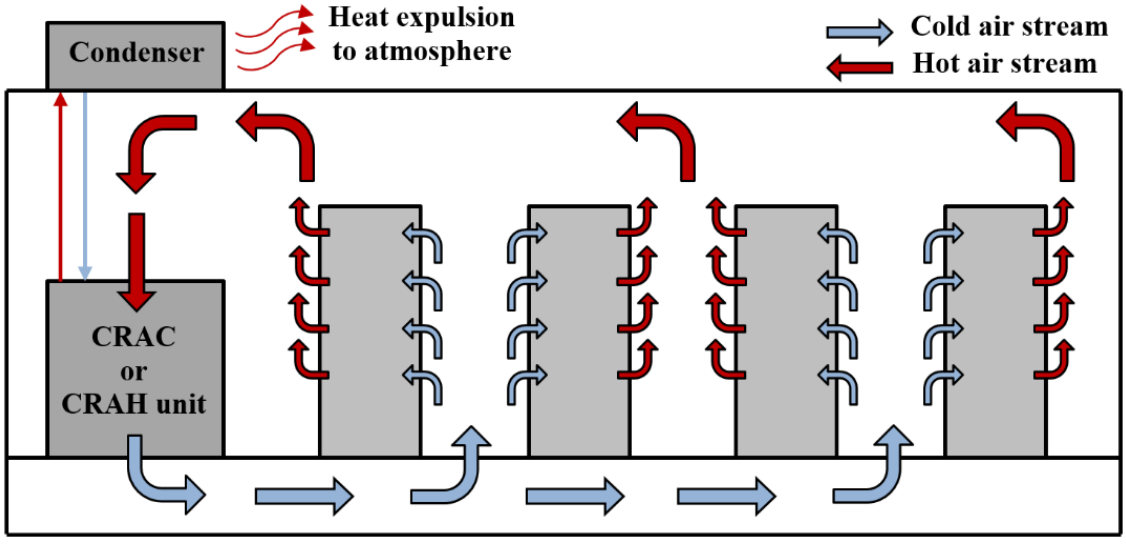

Fig. 2.1 – Schematic of an air cooling system within data centers

Due to the absence of liquid coolants, air cooling systems do not require piping, fluidic connectors, or sealed enclosures of any kind in their application; thus substantially facilitating installation, maintenance, and hot swapping procedures (Garimella et al., 2012). Thus in terms of reliability, accessibility, and practicality, air cooling is unequivocally the most pragmatic solution in both enterprise-class data centers and in-house server rooms.

The major drawback to air cooling, is its poor heat transfer performance. Air possesses inferior thermophysical properties (*i.e.* lower specific heat capacity, thermal conductivity, and density) relative to common liquid coolants which ultimately leads to reduced convective heat transfer coefficients (Kheirabadi & Groulx, 2016b). As a result, air cooling systems require lower inlet temperatures and higher flowrates; the former increases the dependence upon vapor-compression cooling while the latter increases fan power requirements (Kheirabadi & Groulx, 2016b). In addition to its high operating cost, the actual heat transfer limitation of air cooling is also problematic. Considering the current operating conditions employed in air cooling systems, the rate of heat generated by processors in high performance computing applications (HPC) has approached the heat transfer limitation of air cooled heatsinks (Kheirabadi & Groulx, 2016b). This limitation in air cooling systems is of concern to the current research project as military electronics are often classified as HPC systems.

2.2.2 Water Cooling

Single phase water cooling systems replace air cooled heatsinks with some type of liquid cooled cold plate. A typical water cooled data center is visualized in Fig. 2.2. Coolant distribution units (CDU) exchange heat between an external cooling source (*i.e.* supply water, water tower, chiller, etc.) and fluid circulating internal to the facility (Goth, 2012). Within the facility, water is delivered to individual racks and servers where heat is extracted through forced convection inside liquid cooled heatsinks. Typically, only processors are water cooled due to their high heat flux and simplified geometries while remaining server components are air cooled (Tuma, 2010). Nonetheless, certain cooling solutions, such as Asetek's RackCDU D2C™ and IBM's Power 775 Supercomputer (Goth, 2012), have extended liquid cooling to additional server components.

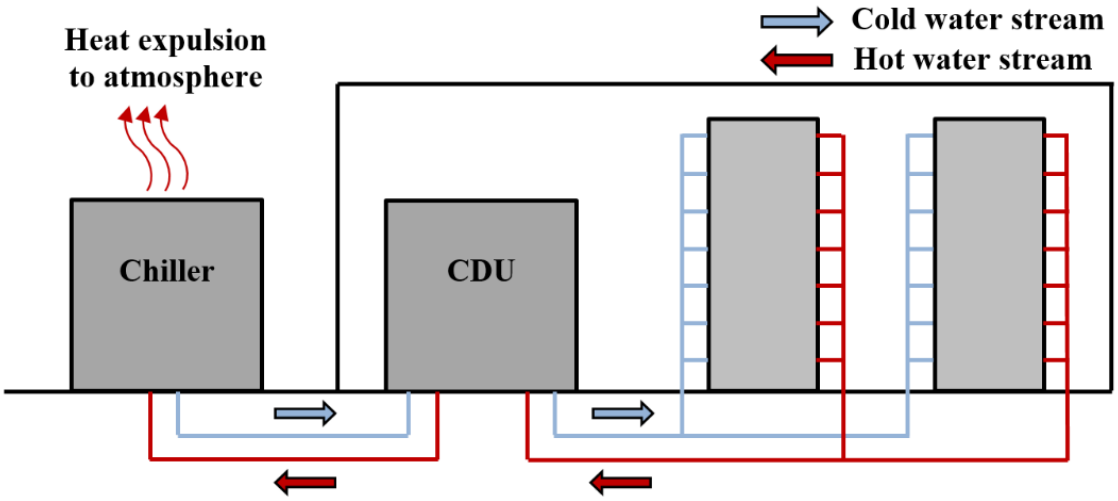

Fig. 2.2 – Schematic of water cooling system within data centers

The primary benefit of water cooling relative to air cooling is its enhanced heat transfer and flow performances. The superior thermophysical properties of water immediately eradicate the heat transfer challenges faced by air cooling systems (Gao et al., 2015). Namely, water at higher inlet temperatures and lower flowrates may be circulated within the cooling system; thus significantly reducing or eliminating dependence upon vapor-compression cooling (Zimmermann, Tiwari, et al., 2012). These high coolant temperatures not only reduce cooling costs but also present ample opportunity for waste heat recovery (Carbó et al., 2016).

In terms of drawbacks, water cooling does not possess the versatility of air cooling and is thus arduous to implement and maintain (Tuma, 2010). The presence of sealed enclosures, facility level piping, and server level tubing implies that cooling solutions must now be tailored to specific facility and server layouts (Tuma, 2010); thus rendering water cooling unpractical in enterprise-class data centers where hundreds of servers and racks are installed or replaced on a daily basis. Water cooling does, however, remain a viable option for smaller server rooms. As a further drawback, disconnecting fluidic connections poses reliability risks when hot swapping servers or components due to the possibility of leakage (Garimella et al., 2012). This potential for leakage was one of the main concerns identified by the Raytheon Company.

2.2.3 Heat Pipe Cooling

A heat pipe is a passive two-phase heat transfer device driven strictly by a temperature difference across its terminals. Vapor formed at the heat pipe evaporator effectively transports energy to the condenser by means of pressure driven advection; while condensed fluid formed at the condenser is driven back to the evaporator through either capillary action (wicked heat pipe) or gravity (thermosyphon) (Siedel et al., 2015). The near-vacuum pressure within the sealed assembly maintains coolants in a consistently saturated state; thus permitting the use of water as a two-phase coolant in electronics cooling applications (Maydanik et al., 2014).

Loop heat pipes (LHP) with flat evaporators in particular have gained precedence in cooling applications due to their compatibility with processor geometries as well as their effectiveness in transferring heat over large distances relative to traditional heat pipes (Maydanik et al., 2014). The operational characteristics of loop heat pipes are demonstrated in Fig. 2.3.

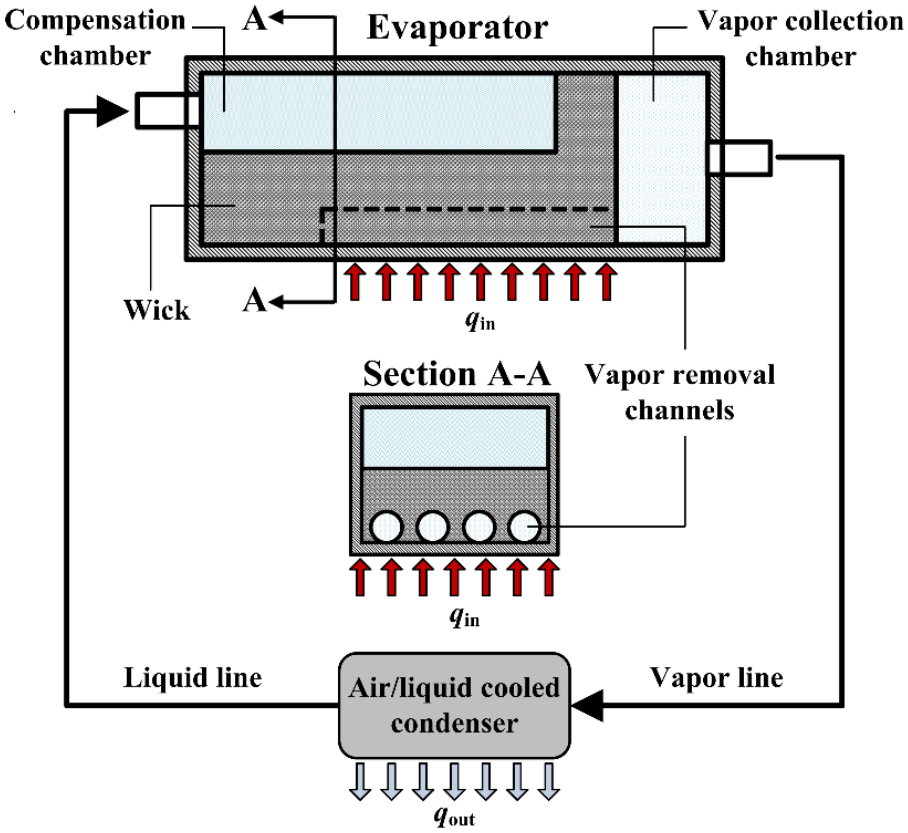

Fig. 2.3 – Schematic of a loop heat pipe cooling system

Heat transferred to the evaporator base (q_{in}) vaporizes the liquid coolant preserved within the porous wick structure in the vicinity of the vapor removal channels. This process in turn produces the pressure necessary to drive the newly formed vapor out of the evaporator (Ku, 1999). Due to a combination of surface tension and adhesive forces between the liquid and wick pores, the menisci formed at the liquid-vapor interface generate sufficient capillary pressure to prevent vapor incursion into the wicked structure (Ku, 1999). The result is vapor accumulation within the vapor collection chamber until there is sufficient pressure to drive the vapor through the vapor line and to the condenser (Siedel et al., 2015). Heat extraction at the condenser (q_{out}) condenses the vapor flow, allowing liquid coolant to return to the compensation chamber located near or within the evaporator assembly (Ku, 1999). The purpose of the compensation chamber is to store excess liquid and uncondensed vapor much like a reservoir in two-phase cooling applications (Ku, 1999).

Since heat pipes are passive cooling devices, no pumps or moving components are necessary within individual servers which improves reliability (McGlen et al., 2004). Furthermore, heat pipes are hermetically sealed devices with no fluidic connections to pose leakage risks (McGlen et al., 2004). Heat may be extracted from heat pipe condensers through forced air convection, traditional heat exchangers, or thermal contact heat exchangers.

Despite these advantages, heat pipes face similar if not exacerbated versatility challenges as do water cooling systems. Like water cooling systems, heat pipe systems must be tailored to specific server layouts. In fact, they are generally more difficult to manufacture due to the requirement of porous structures, metal tubing, and vacuum sealing (Shabgard et al., 2015). As a result, these systems are similarly only practical in smaller server rooms. In addition to these drawbacks, heat pipe systems are inferior in terms of heat transfer performance relative to water cooling (Kheirabadi & Groulx, 2016b). This point will be addressed in the next chapter.

2.2.4 Open Bath Immersion Cooling

Open bath immersion cooling, also referred to as pool boiling, is rapidly gaining popularity in server cooling applications as it combines the benefits of air and liquid cooling while overcoming their disadvantages (Kheirabadi & Groulx, 2016b). As shown

in Fig. 2.4, electronic components are immersed within a bath of dielectric coolant. The temperature rise of high heat flux surfaces above the saturation temperature of the coolant induces nucleate boiling within the dielectric bath; thus cooling components through latent heat transfer, bubble induced flow mixing, and gravity driven two-phase convection (Qiu et al., 2015). Vapor bubbles that are formed at heated surfaces rise to an allocated vapor space above the dielectric bath where the coolant is condensed through a water-cooled heat exchanger (Tuma, 2010).

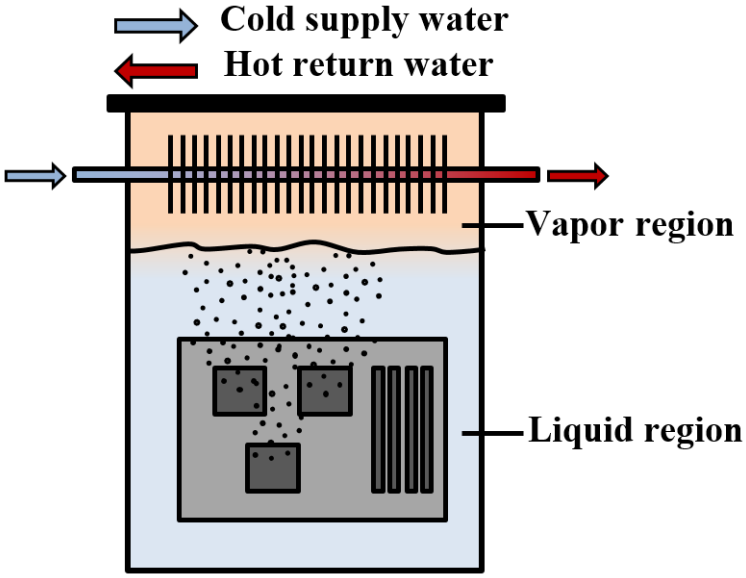

Fig. 2.4 – Schematic of an open bath passive immersion cooling system

A primary benefit of open bath immersion cooling is the absence of hermetically sealed enclosures, server level piping, and fluidic connectors; thus yielding a highly versatile solution that also permits low-maintenance hot swapping of server components (Tuma, 2010). Additionally, the passive heat transfer characteristics eliminate chip level pumping power requirements while improving reliability (Tuma, 2010); essentially emulating heat pipes while operating at atmospheric pressure. Although its heat transfer performance remains inferior to water cooling, pool boiling is nevertheless substantially superior to air cooling (Kheirabadi & Groulx, 2016b).

Drawbacks to open bath immersion cooling include vapor loss and the requirement of degassing (Tuma, 2011). Since these systems must remain open to the atmosphere for boiling to ensue, they require degassing systems to extract infiltrating air and humidity (for which dielectric coolants have a high affinity); this process results in vapor losses that must

be accounted for over time (Tuma, 2011). More specific to military environments, fluctuating accelerations and orientations present obvious maintenance difficulties for an open bath liquid cooling system. Additionally, boiling heat transfer performance is dependent upon the direction of gravity (Ali & El-Genk, 2012).

2.2.5 Other Cooling Strategies

Other cooling strategies reviewed include two-phase liquid cooling, spray cooling, and jet impingement. Indirect two-phase liquid cooling is implemented in a similar fashion to water cooling in that refrigerants or dielectric coolants are driven through liquid cooled heatsinks instead of water. The latent heat transfer and isothermal vaporization processes reduce temperature gradients along heated surfaces and slightly increase heat transfer performance relative to water cooling (Asadi et al., 2014). However, two-phase flow systems suffer from flow instabilities which induce pressure and temperature fluctuations, flow reversal, and other phenomena that may cause electronics to overheat (Kadam & Kumar, 2014).

Spray cooling and jet impingement offer the most superior heat transfer performance of all methods reviewed (Kheirabadi & Groulx, 2016b). Nevertheless, they also suffer from significant implementation challenges. If applied in a direct manner (*i.e.* the coolant comes into direct contact with electronics), server electronics must be sealed within a vapor chamber that maintains two-phase flow (Tuma, 2010). Such vapor chambers will require additional maintenance procedures when hot swapping components as they must be evacuated and then refilled with coolant prior to the electronics being re-commissioned (Tuma, 2010). These arduous maintenance requirements are likely the reason why direct spray cooling and jet impingement systems are non-existent within the server cooling industry (Kheirabadi & Groulx, 2016b).

Chapter 3 - Thermal Contact Liquid Cooling System

This chapter first provides a description of the cooling approach proposed for military applications. The cooling method is referred to as a thermal contact liquid cooling system. Subsequently, the selection of this particular design is justified based upon the benefits and drawbacks presented in the review information from the previous chapter. Finally, a technology review more specific to thermal contact liquid cooling systems is presented.

3.1 Overview of Proposed Design

Given the considerations from the previous chapter, the thermal management solution which was deemed most practical for remote military applications is a thermal contact water cooling system. This solution differs from a conventional water cooling system illustrated in Fig. 3.1. In both cases, server level pumps circulate water through liquid cooled heatsinks attached to the server's processors. In the case of a conventional water cooling system, quick-disconnect fluidic connectors are necessary to terminate flow when the server is being hot swapped. As mentioned in the previous chapter, this process engenders leakage risks in the case of connector malfunction and Raytheon Canada has emphasized this risk as a major obstacle to improving reliability.

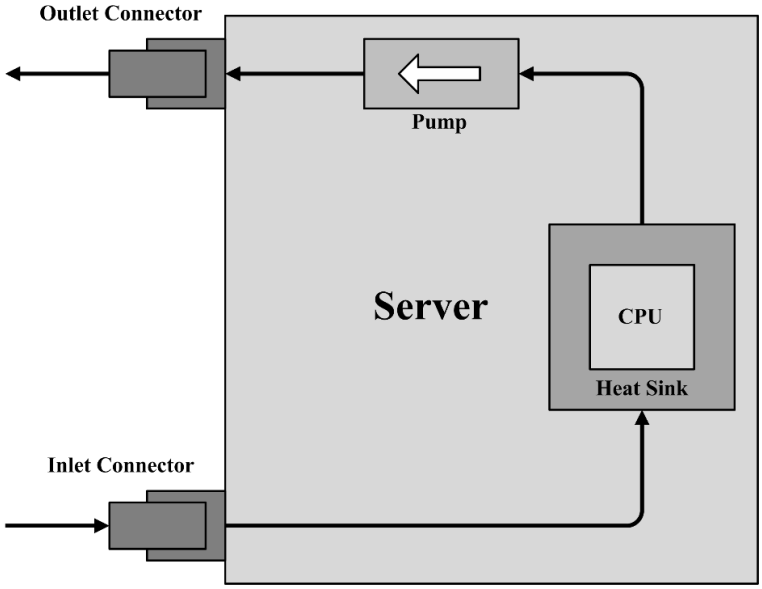

Fig. 3.1 – Schematic of a conventional liquid cooling system with fluidic connectors

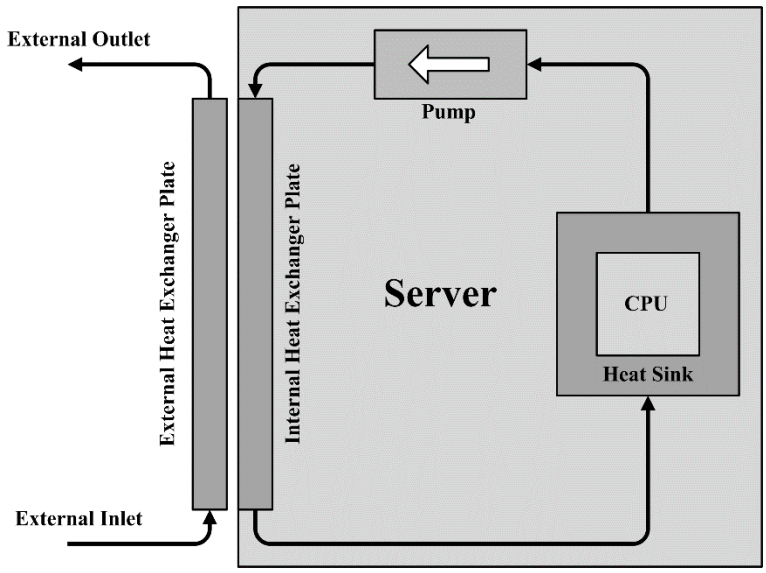

Fig. 3.2 – Schematic of a thermal contact liquid cooling system with no fluidic connectors

As a remedy, the proposed solution was simply to replace these fluidic connectors with a thermal contact heat exchanger (TCHx) as shown in Fig. 3.2. A TCHx is essentially a flat plate heat exchanger (FPHE) in which the two heat exchanger plates are easily separated without terminating flow. This feature is achieved due to the fact that only heat, and not fluid, is transferred across the contacting heat exchanger plates; hence the name thermal contact heat exchanger. The TCHx consists of internal and external heat exchanger plates. The internal plate is physically attached to the server and is permanently part of the closed liquid cooling loop within the server itself. The external plate is attached to the server rack and is permanently part of the facility level liquid cooling loop. Heat transfer occurs only when the server is mounted onto the server rack causing the two heat exchanger plates to come into contact.

The immediately obvious advantage of such a system over a conventional water cooling system is that fluid flow is never terminated when hot swapping servers. The liquid cooling loop within the server remains closed at all times. As a result, the reliability risk associated with connector leakage is eliminated and the cooling system may remain operational 100 % of the time. The drawback, however, is that the TCHx adds additional thermal interfaces which are accompanied by additional thermal resistances. The outcome here, which was and should be apparent prior to any numerical or experimental work, is that the thermal performance of the proposed cooling system is inferior to that of a

conventional water cooling system. Specifically, inlet water at a lower temperature is required by the proposed cooling system relative to a conventional system in order to maintain the processor at the same temperature for any given heat load. As mentioned in the introduction, the primary aim of experimentation was to quantify this inferiority and to determine whether it is a practical trade-off for the added reliability.

3.2 Justification of the Proposed Cooling Strategy

The previous section described the cooling solution proposed for remote military applications. The current section justifies the selection of this solution based on the review information presented in the previous chapter. In addition to this qualitative information, the cooling strategies are also quantitatively compared in Fig. 3.3. This figure plots effective heat transfer coefficients calculated from each experimental study that was reviewed in preparation for this work. The horizontal grey bars indicate the range of effective heat transfer coefficients observed for each cooling strategy while the vertical black lines represent the effective heat transfer coefficients from individual studies. The figure has been taken directly from the more comprehensive review article mentioned at the start of the previous chapter (Kheirabadi & Groulx, 2016b).

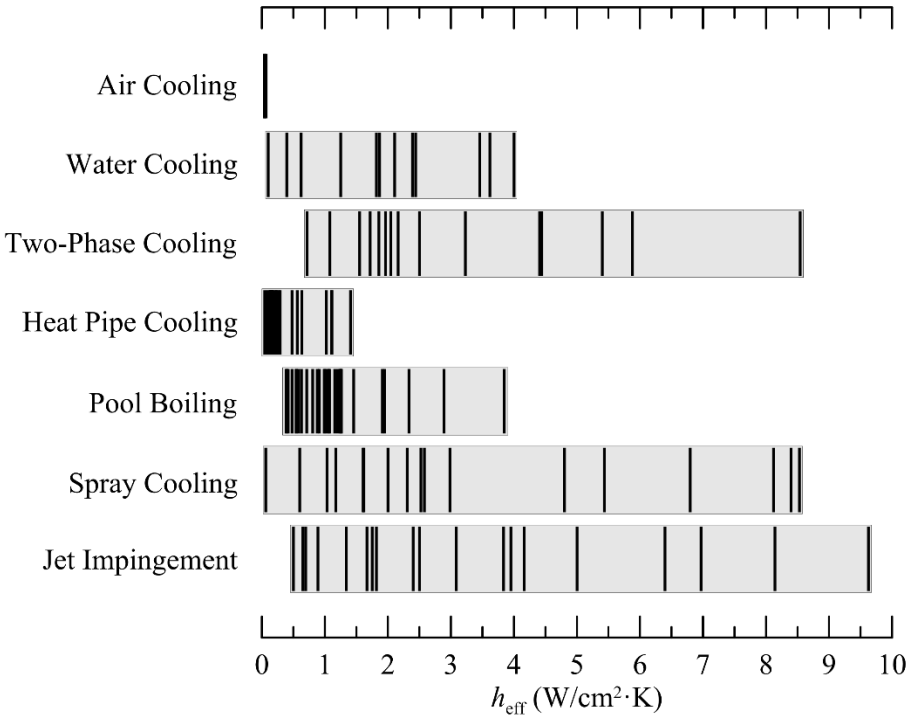

Fig. 3.3 – Effective heat transfer coefficients from reviewed experimental studies on electronics cooling

The effective heat transfer coefficient h_{eff} is defined as follows:

$$h_{\text{eff}} = \frac{q}{A_{\text{hs}}(T_{\text{w}} - T_{\text{in}})} \tag{3.1}$$

where q is the rate of heat generated by the heat source, T_{w} is the heat source temperature, and T_{in} is the inlet temperature of the coolant. If a particular cooling system contains a heatsink or heat spreader, then the base area of this component is represented by A_{hs}. If no such component exists, then A_{hs} simply represents the heat source area.

The reader is referred to the review article (Kheirabadi & Groulx, 2016b) for a more detailed explanation of the effective heat transfer coefficient. Given the current context, it suffices to say that a cooling system with a higher effective heat transfer coefficient consumes less server area (smaller heatsink area A_{hs}), has higher thermal limits (higher heat load q), and permits warmer coolants (higher inlet temperature T_{in}). In other words, a higher effective heat transfer coefficient is advantageous from every standpoint.

In the previous chapter, the cooling strategies that were considered practical for server cooling applications were air cooling, water cooling, heat pipe cooling, and pool boiling. Two-phase liquid cooling, spray cooling, and jet impingement were omitted from this list. Even though these three strategies possess the highest effective heat transfer coefficients according to Fig. 3.3, they suffer from a variety of implementation issues as described in the previous chapter.

Of the strategies considered practical, air cooling was immediately deemed inadequate due its low heat transfer limits and high cost of operation; the latter of which was recognized as a major concern by Raytheon Canada. A brief look at Fig. 3.3 shows that the range of effective heat transfer coefficients from air cooling experimental studies are virtually negligible relative to all other liquid cooling strategies. Therefore, despite the many advantages of air cooling such as the absence of sealed enclosures and facilitated hot swapping, a transition from air to liquid cooling was necessary for improved thermal performance.

Of the remaining strategies, which were water cooling, heat pipe cooling, and pool boiling, the heat transfer performance was no longer the deciding factor. As shown in Fig. 3.3, the effective heat transfer coefficients associated with these systems substantially exceed those associated with air cooling. Water cooling and pool boiling systems exhibit effective heat transfer coefficients as high as 4 W/cm^2·K while heat pipe cooling systems

fall short with effective heat transfer coefficients as high as 1.5 $W/cm^2 \cdot K$. For comparison, the effective heat transfer coefficients of air cooling systems range from 0.04 to 0.07 $W/cm^2 \cdot K$.

Consequently, one should examine the practicality, reliability, and implementation challenges of these liquid cooling solutions when determining the ideal strategy for a given application. Although pool boiling systems combine the thermal performance of liquid cooling systems with the simplicity and practicality of air cooling systems, they are not ideal for military applications. Military data centers located aboard ships, aircraft, and ground vehicles are subject to acceleration and orientation fluctuations which are problematic for an open bath liquid cooling system. Additionally, a cooling system which is open to the atmosphere cannot withstand contaminated or corrosive environments. For these reasons, it is the opinion of the author that pool boiling systems are ideal for enterprise-class data centers such as those located in Silicon Valley. Military data centers require more robust systems; thus leaving heat pipe and water cooling systems as potential candidates.

Heat pipes are passive heat transfer devices and therefore do not require server level pumps for operation. Although this passivity certainly improves reliability, it comes with the cost of inferior heat transfer performance, as shown in Fig. 3.3, and manufacturing challenges due to porous structures and vacuum sealing procedures. Water cooling systems on the other hand are less arduous to manufacture as they contain less intricate components. Water cooling systems also deliver improved thermal performance as shown in Fig. 3.3; thus providing the best opportunity for waste heat recovery and operating cost reductions. The presence of a server level pump is a fair trade-off for these characteristics. Furthermore, the integration of miniature centrifugal pumps within servers is common practice among developers of water cooling systems such as Asetek and CoolIT Systems. Given these considerations and the current state of cooling technologies, water cooling was deemed the ideal cooling solution for military applications; however, not in its conventional form.

Conventional water cooling systems utilize fluidic connectors to deliver water to and from servers. These connectors present an opportunity for leakage when hot swapping servers which, to reiterate, was a major, if not the primary, concern brought to light by

Raytheon Canada. The simplest solution to this problem was therefore to replace the fluidic connectors with a thermal contact heat exchanger and to eliminate the potential for leakage altogether. The details of this proposed design have been adequately detailed in the previous section. The aim of the current section has been to justify why water cooling was preferred over the remaining cooling strategies discussed.

On a final note, one of the drawbacks of water cooling systems discussed is a lack of versatility which renders water cooling unpractical in large enterprise-class data centers. This lack of versatility is equally, if not especially, true for the proposed cooling system. A thermal contact liquid cooling system requires a heatsink, a miniature pump, and two plate heat exchangers per server. Furthermore, the location and scale of these components must be tailored to each unique server layout. It is therefore not difficult to see how installing and maintaining such a cooling system would be problematic in data centers containing several thousand servers. As a result, it should be noted that the proposed cooling solution is only practical in smaller server rooms with strict reliability constraints.

3.3 Literature Review: Thermal Contact Liquid Cooling Systems

The aim of this section is to offer a more specific review of literature related to thermal contact water cooling systems. To the author's best knowledge at the time of writing, there exists no literature pertaining to an experimental evaluation of such systems; thus indicating that there has been little to no interest in this topic within the research community and the reasons for this are understandable. A thermal contact water cooling system consists of a liquid cooled heatsink, of which there is and continues to appear enormous volumes of experimental research, operating in conjunction with a thermal contact heat exchanger.

The thermal contact heat exchanger is technically nothing more than two larger and simpler heatsinks coupled together. Although evaluating the performance of such a system is of interest to Raytheon Canada and is therefore central to this research project, there is little potential for innovation and discovery by pursuing such research. This mundanity is likely the reason why experimental studies on thermal contact water cooling systems are nonexistent. On the contrary, experimental studies on thermal contact heat pipe cooling systems are abundant. The reason being that heat pipe flow and heat transfer characteristics

are quite complex and, as a result, the influence of heat exchanger geometries on heat pipe performance is not as well understood.

Despite the lack of interest from the research community, thermal contact water cooling systems are quite popular within the electronics cooling industry. Table 3.1 lists a number of patents filed over the past decade and a half which the author has deemed most relevant to the current research. This table lists the assignee of the intellectual property as well as a brief description of the patented technology. Patents concerning thermal contact heat pipe cooling systems have also been included in this table wherever the thermal contact mechanisms described are relevant to the current research.

The aim here is not to describe in detail the technologies presented in each of these patents. The focus of the current work is to carry out an experimental evaluation of the proposed cooling system and an in-depth review of these patents would be a wasted effort. Furthermore, patents are written in annoyingly broad and generalized legal terms which renders a review even more fruitless. The purpose of Table 3.1 is chiefly to demonstrate that there clearly exists interest in such technology from major industry players such as Hewlett-Packard, IBM, Dell, and Asetek. Secondly, Table 3.1 provides a number of sources which would be useful to any thermal engineers who may be tasked with further developing the proposed cooling system.

As a very brief review, certain patents describe elaborate and promising coupling mechanisms for thermal contact heat exchangers. A 2012 patent assigned to the Liebert Corporation (Spearing & Schrader, 2012) describes various coupling mechanisms employing cams, spring-loaded joints, and dovetail joints to ensure firm thermal contact between the internal and external heat exchanger plates as the server is mounted onto a server rack. A 2002 patent assigned to Hewlett-Packard (Koenen, 2002) describes a spring-loaded bracing mechanism which involves two plates wrapping around a third as the server is mounted onto a server rack. In this case, the two plates are fixed to the server rack and serve as external heat exchanger plates while the third plate is fixed to the server and serves as the internal heat exchanger plate. The mechanisms from both of these patents have been designed such that server may be hot swapped without the use of tools.

Another 2014 patent assigned to Asetek (Branton, 2014) highlights the use of an air-water heat exchanger within the server to cool the circulating air. In other words, the water

circulating within the internal loop (within the server) would be cooling high heat flux components such as processors directly while also indirectly cooling low heat flux components by cooling the air flowing through the server. This approach of cooling server room air using air-water heat exchangers rather than CRAC units has been shown to reduce overall capital and operating costs by 30 to 40 % (Grimshaw et al., 2011).

Although interesting, the intellectual properties claimed within these patents focus upon either the general concept of thermal contact liquid cooling or coupling mechanisms for the heat exchanger plates. Neither of these elements are pertinent to the current work for which the aim is to evaluate the thermal performance of thermal contact liquid cooling systems as a whole. Rather, this objective requires focus upon the geometric layouts of the heat exchangers and their impact upon heat transfer and flow characteristics.

Table 3.1 – Patents consisting of thermal contact liquid cooling systems

Ref.	Assignee	Description
(Branton, 2014)	Asetek	TCHx cooling system with air-water heat exchanger
(Spearing & Schrader, 2012)	Liebert Corp.	Coupling mechanisms for TCHx assemblies
(Campbell et al., 2012)	IBM Corp.	Mounting method for servers with TCHx assemblies
(Fried, 2011)	-	Loop heat pipe cooling system with TCHx assembly
(Martin et al., 2010)	Liebert Corp.	TCHx system for uninterruptible power supplies
(Brewer et al., 2010)	Cooligy, Inc.	TCHx water cooling system for servers
(Upadhya et al., 2009)	Cooligy, Inc.	TCHx water cooling system for servers
(McCoy, 2009)	Hewlett-Packard	Heat pipe cooling system with TCHx assembly
(Hom et al., 2009)	-	Heat pipe cooling system with TCHx assembly
(Ishimine, 2008)	Fujitsu, Ltd.	TCHx water cooling system for servers
(Pflueger, 2008)	Dell	Heat pipe cooling system with TCHx assembly
(Konshak, 2007)	Sun Microsys.	Coupling mechanisms for TCHx assemblies
(Chu et al., 2006)	IBM Corp.	TCHx water cooling system for servers
(Belady & Womack, 2004)	Hewlett-Packard	Coupling mechanisms for TCHx assemblies
(Kondo et al., 2004)	Hitachi, Ltd.	TCHx water cooling system for servers
(Bear, 2004)	Liebert Corp.	Heat pipe cooling system with TCHx assembly
(Phillips et al., 2004)	Thermal Corp.	Heat pipe cooling system with TCHx assembly
(Memory et al., 2004)	-	Heat pipe cooling system with TCHx assembly
(Garner, 2003)	Thermal Corp.	Heat pipe cooling system with TCHx assembly
(Koenen, 2002)	Compaq	Coupling mechanisms for TCHx assemblies

Chapter 4 - Numerical Design and Optimization of Heat Exchangers

The current chapter outlines the numerical method used to design and optimize the liquid cooled heatsink and thermal contact heat exchanger for experimental study. The heatsink design employed was a simple straight channel heatsink due to its popularity in existing literature and its manufacturability relative to pin finned heatsinks or other exotic designs. This chapter first describes the numerical method in the context of optimizing the heatsink then extends the approach to the thermal contact heat exchanger design. Some brief discussion is first necessary on the general structure of the TCHx.

4.1 TCHx Plate Designs

The most effective design for a thermal contact heat exchanger would undoubtedly involve coupling two plate heat exchangers. As shown in Fig. 4.1, fins should be located on the liquid side of each plate heat exchanger in order to maximize convective heat transfer. Contrary to some of the patents reviewed, there should not exist any type of extended surfaces on the thermal contact side. The two flat surfaces should come into direct contact with thermal interface materials in between minimizing contact resistance. This design maximizes conductive heat transfer at the base of each plate heat exchanger by minimizing the length over which heat is conducted. The only question that remains pertains to the design and dimensioning of the fins on the liquid side of each plate heat exchanger.

As shown in Fig. 4.2, three fin layouts were considered for experimental study: straight parallel channels, a single serpentine channel, and mixed serpentine-parallel channels. A numerical model of these designs is beneficial for a number of reasons. First, it enables optimization of the heat exchangers prior to construction for experimentation. Second, validation of the numerical model with experimental results provides a reliable means of designing and optimizing such systems in future applications. Given its quasi-symmetric nature, however, the straight channel plate heat exchanger was the only layout fit for parametric numerical studies (the reasons for which are explained in subsequent

sections). The remaining designs must be modelled in full and would require greater computational resources; thus rendering parametric numerical studies unpractical.

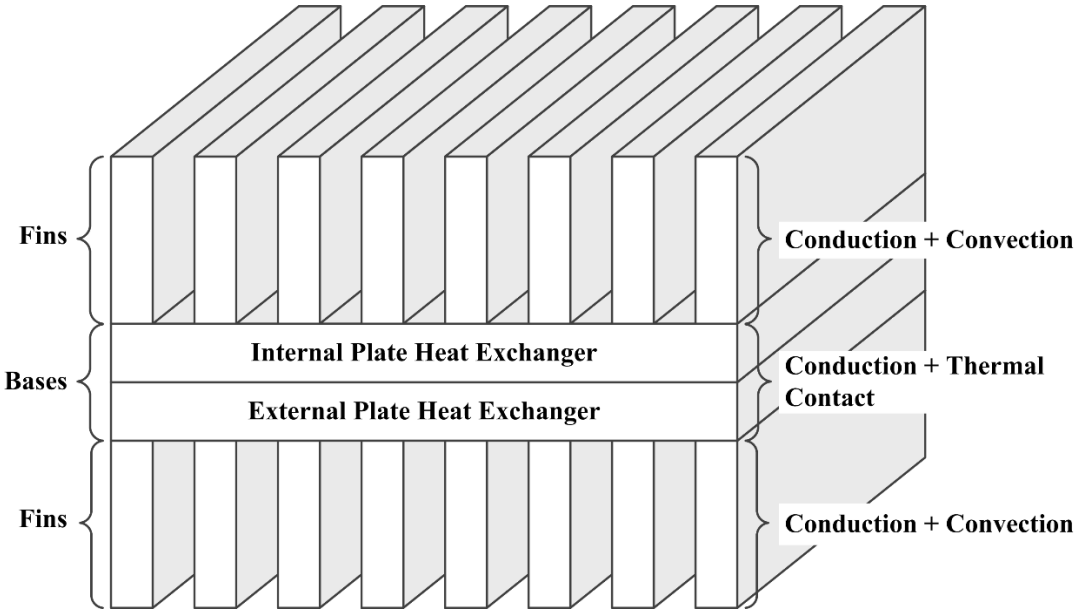

Fig. 4.1 – Schematic of ideal TCHx structure

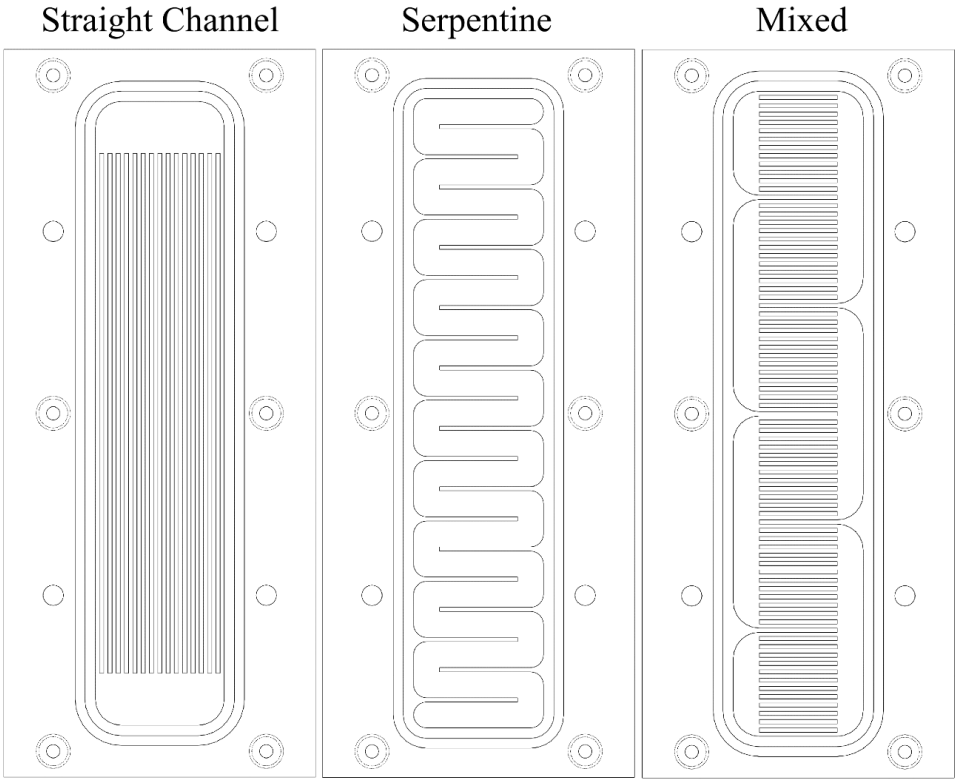

Fig. 4.2 – Schematic of three plate heat exchanger designs tested experimentally

4.2 Unit Cell Method vs. Full Three Dimensional Modelling

Heat transfer and flow phenomena within straight channel heatsinks are most commonly simulated using the unit cell approach. This method involves modelling a single channel along with its corresponding base and surrounding fins. The primary benefit of this technique is its computational expediency. By omitting the inlet and outlet manifolds of the heatsink, the size and complexity of the numerical model are greatly reduced. This simplification permits large quantities of parametric studies within a short time span; although, the validity of this technique is highly dependent upon temperature and flow distributions across a given heatsink.

The unit cell method presumes that temperature and flow are identically distributed across each channel within a heatsink; hence enabling the use of a single quasi-symmetric unit cell to represent the entire heatsink. A numerical investigation has been carried out by the authors investigating the legitimacy of this presumption (Kheirabadi & Groulx, 2016a). The results of this study have been presented at the 2016 ASME Summer Heat Transfer Conference and will only be summarized in the current study.

The study simulated water flow through a copper heatsink with varying channel widths (and thus a varying number of overall channels). Two methods were employed and compared: the unit cell approach and a full three dimensional approach which included the heatsink inlet and outlet manifolds. The primary objective was to identify the channel width at which these models began to produce similar results. More simply put, the aim was to identify the point at which the unit cell approach becomes a valid approximation (assuming that the full three dimensional approach is completely accurate). It was expected that at large channel widths (*i.e.* fewer channels), flow would not be identically distributed among the various channels; resulting in higher convection coefficients in certain channels which would invalidate the unit cell approximation at large channel widths. It was also expected that at lower channels widths (*i.e.* more channels), the impedance to flow resulting from wall friction would force the flow to more equally distribute among the various channels. This uniform distribution would render the unit cell method a valid approximation at smaller channel widths.

These speculations were strikingly confirmed with numerical results. The maximum heatsink wall temperatures as a function of channel size predicted by both methods are

shown in Fig. 4.3. The maximum wall temperature is the highest temperature along the heated surface (*i.e.* the surface of a heat source which contacts the heatsink). This parameter is typically used in experimental studies to evaluate the performance of a heatsink. As the figure shows, the maximum wall temperature predicted by the unit cell method is 32.8 % larger than that predicted by the full three dimensional method at a channel size of 1 mm (*i.e.* 11 channels). At a channel size of 0.25 mm (*i.e.* 41 channels), this difference has reduced to 5.44 %; hence confirming the validity of the unit cell method at smaller channels widths.

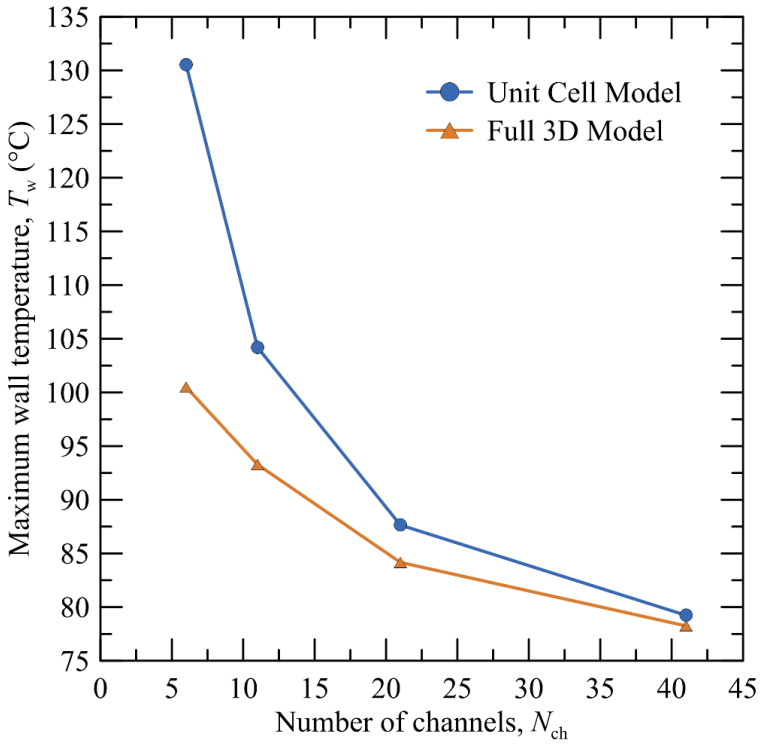

Fig. 4.3 – A comparison of heat source temperatures predicted by unit cell and full three dimensional models (Kheirabadi & Groulx, 2016a)

When determining the range of channel widths over which the unit cell approximation may be applied, it is important to observe that this method always overestimates the maximum wall temperature. In other words, it underestimates the heat transfer coefficient which results in a more conservative prediction of thermal performance. Given the current application, the author deems it practical to utilize this technique in performing parametric studies for channel widths equal to or smaller than 1 mm. Although this method is inaccurate at the larger end of this spectrum, its

computational expediency and conservative estimation offer a more pragmatic solution than the full three dimensional approach.

4.3 Heatsink Design and Optimization

The following subsections outline the numerical procedure for designing and optimizing the heatsink channel geometry. This method is later used to design and optimize the straight channel TCHx plate.

4.3.1 Geometry

The dimensions necessary for modelling a unit cell are outlined in Fig. 4.4. As shown, only a single channel of width W_{ch}, height H_{ch}, and length L_{ch} is modelled. This channel is enclosed at its vertical sides by half of each surrounding fin; with the width of each fin being denoted by W_f. The bottom surface of the channel is enclosed by the corresponding portions of the heatsink base (thickness denoted by t_b) and the heat source (thickness denoted by t_{source}). Additional parameters of importance not shown in the figure include the ratio of channel-to-fin widths, R_{chf}, and the heatsink base width, W_b.

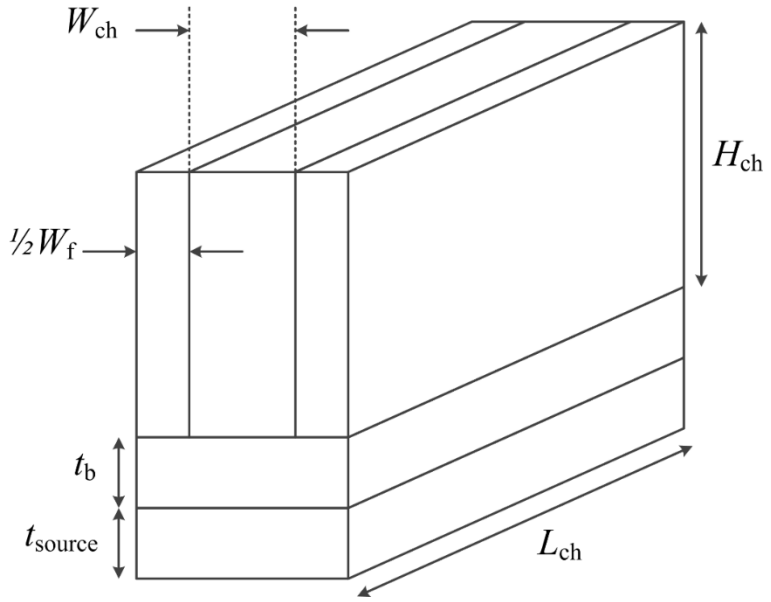

Fig. 4.4 – Schematic of unit cell geometry for numerically modelling heatsink

When constructing a heatsink, the designer will typically have a heatsink base width and a channel width in mind; however, these dimensions do not always conform to one another. For instance, a 4 mm wide heatsink with 1 mm channels and fins is not a possible combination of parameters. The first millimeter consists of a channel, the second a fin, the

third a channel, and the fourth a fin. The problem is that the final millimeter must consist of a channel. Therefore, in order to accommodate 1 mm wide channels and fins, this specific heatsink must be either 3 or 5 mm wide. This geometric constraint is an important issue to address when conducting parametric studies in which the channel width is varied.

The solution involves specifying the desired heatsink base width and then recalculating this width based on the current channel and fin widths. The relationship between the heatsink base width and the channel and fin widths is first defined as follows:

$$W_{\mathrm{b}} = N_{\mathrm{ch}} W_{\mathrm{ch}} + N_{\mathrm{f}} W_{\mathrm{f}} \tag{4.1}$$

where N_{ch} and N_{f} represent the number channels and fins, respectively. The ratio of channel-to-fin widths is simply defined as follows:

$$R_{\mathrm{chf}} = \frac{W_{\mathrm{ch}}}{W_{\mathrm{f}}} \tag{4.2}$$

Since the first and last spaces within a heatsink must contain channels, the relationship between the number of channels and fins is defined as follows:

$$N_{\mathrm{ch}} = N_{\mathrm{f}} + 1 \tag{4.3}$$

After compiling these equations, the heatsink base width may be redefined as follows:

$$W_{\mathrm{b}} = W_{\mathrm{ch}} \left[N_{\mathrm{ch}} \left(1 + \frac{1}{R_{\mathrm{chf}}} \right) - \frac{1}{R_{\mathrm{chf}}} \right] \tag{4.4}$$

Solving this equation for N_{ch} and rounding gives:

$$N_{\mathrm{ch}} = \mathrm{round} \left(\frac{\frac{W_{\mathrm{b}}}{W_{\mathrm{ch}}} + \frac{1}{R_{\mathrm{chf}}}}{1 + \frac{1}{R_{\mathrm{chf}}}} \right) \tag{4.5}$$

The above equation calculates the number of channels based upon the desired heatsink base width, channel width, and channel-to-fin width ratio and then rounds the answer to the closest integer. When constructing the heatsink, the actual heatsink base width may be calculated by substituting N_{ch} calculated from Eq. (4.5) back into Eq. (4.4).

4.3.2 Boundary Conditions

The boundary conditions imposed within the numerical model are shown in Fig. 4.5. These include the heatsink inlet water temperature and velocity, $T_{\mathrm{in,hs}}$ and $V_{\mathrm{in,hs}}$, the rate of heat generated by the heat source, q_{source}, and the thermal contact resistant between the heat source and the heatsink base, R''_{TIM}. The values of these parameters are discussed in subsequent sections. A symmetry boundary condition was imposed along the side while all remaining faces were assumed to be insulated.

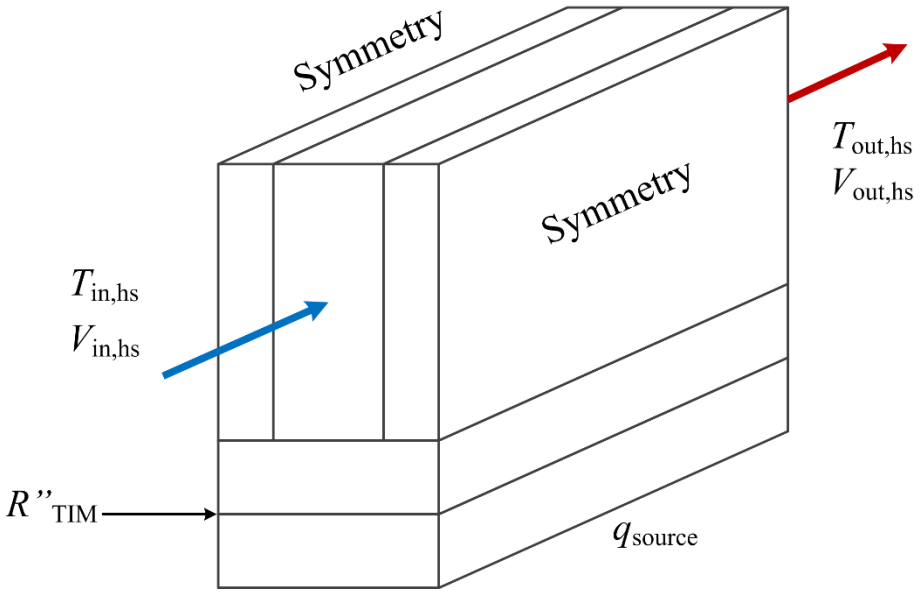

Fig. 4.5 – Schematic of boundary conditions imposed upon the heatsink unit cell model

Since the number of channels as a function of the channel width has been calculated, the mean inlet velocity within each channel may by defined as:

$$V_{\text{in,hs}} = \frac{Q_{\text{hs}}}{N_{\text{ch}} W_{\text{ch}} H_{\text{ch}}} \tag{4.6}$$

where Q_{hs} represents the total flowrate of water through the heatsink. The heat source heat generation rate for the unit cell may be calculated by first defining the following area ratio:

$$A_{\text{r}} = \frac{L_{\text{ch}}(W_{\text{ch}}+W_{\text{f}})}{L_{\text{ch}} W_{\text{b}}} = \frac{W_{\text{ch}}+W_{\text{f}}}{W_{\text{b}}} \tag{4.7}$$

The denominator in the above equation represents the base area of the heatsink while the numerator represents the base area of a single unit cell. This equation thus calculates the portion of the heatsink base area accounted for by the unit cell. This ratio may be used to determine the heat source heat generation rate for the unit cell as follows:

$$q_{\text{source}} = q_{\text{total}} A_{\text{r}} \tag{4.8}$$

where q_{total} is the total rate of heat generated by the entire heat source and q_{source} is solely the amount generated at the unit section shown in Fig. 4.5.

4.3.3 Material Properties

All numerical work was completed using the finite element package COMSOL Multiphysics 5.0 and its built-in material properties of copper and water were used across all simulations; these properties are listed in Table 4.1. It should be noted that the built-in

properties of water were temperature dependent and the listed values correspond to a water temperature of 60 °C.

Table 4.1 – Material properties based on COMSOL built in properties

Property	Copper	Water (60 °C)
Density, ρ (kg/m^3)	8700	985
Specific Heat Capacity, c_p (J/kg·K)	385	4180
Thermal Conductivity, k (W/m·K)	400	0.65
Dynamic Viscosity, μ (Pa·s)	-	4.7×10^{-4}

Copper domains consisted of the fins, the heatsink base, and the heat source. All simulations were run at steady state and the heat source was insulated on all sides except for that which contacted the heatsink base; thus all heat generated was transferred to the heatsink and the heat source material was irrelevant. Experimental studies concerning heatsink design also typically employ copper heat sources rather silicon (which is more representative of a chip package).

4.3.4 Governing Equations

All simulations modelled single-phase water flow as laminar, steady state, and incompressible with negligible viscous dissipation. Laminar flow is justified by the fact that Reynolds numbers for channel widths smaller than 2 mm did not exceed 2300. Furthermore, laminar flow is unanimously used in existing literature. The addition of viscous dissipation altered the wall temperature predictions by less than 0.03 %; hence it was also neglected to maintain consistency with existing literature. Moreover, studies have shown that viscous dissipation in channels is negligible at hydraulic diameters greater than 100 μm (Koo & Kleinstreuer, 2004; Morini, 2005). The smallest hydraulic diameter modelled numerically was roughly 60 μm. This diameter corresponded to a channel width of 0.03 mm which, practically speaking, is too miniscule for CNC machining. The resulting continuity, momentum, and energy conservation equations used to model flow and heat transfer within the fluid channel are:

$$\frac{\partial u}{\partial x} + \frac{\partial v}{\partial y} + \frac{\partial w}{\partial z} = 0 \tag{4.9}$$

$$\rho\left(u\frac{\partial u}{\partial x} + v\frac{\partial u}{\partial y} + w\frac{\partial u}{\partial z}\right) = -\frac{\partial P}{\partial x} + \mu\left(\frac{\partial^2 u}{\partial x^2} + \frac{\partial^2 u}{\partial y^2} + \frac{\partial^2 u}{\partial z^2}\right) \tag{4.10}$$

$$\rho\left(u\frac{\partial v}{\partial x}+v\frac{\partial v}{\partial y}+w\frac{\partial v}{\partial z}\right)=-\frac{\partial P}{\partial y}+\mu\left(\frac{\partial^2 v}{\partial x^2}+\frac{\partial^2 v}{\partial y^2}+\frac{\partial^2 v}{\partial z^2}\right) \quad (4.11)$$

$$\rho\left(u\frac{\partial w}{\partial x}+v\frac{\partial w}{\partial y}+w\frac{\partial w}{\partial z}\right)=-\frac{\partial P}{\partial z}+\mu\left(\frac{\partial^2 w}{\partial x^2}+\frac{\partial^2 w}{\partial y^2}+\frac{\partial^2 w}{\partial z^2}\right) \quad (4.12)$$

$$\rho c_{\mathrm{p}}\left(u\frac{\partial T}{\partial x}+v\frac{\partial T}{\partial y}+w\frac{\partial T}{\partial z}\right)=k\left(\frac{\partial^2 T}{\partial x^2}+\frac{\partial^2 T}{\partial y^2}+\frac{\partial^2 T}{\partial z^2}\right) \quad (4.13)$$

where ρ, μ, c_{p}, and k are the density, dynamic viscosity, specific heat capacity, and thermal conductivity of water, u, v, and w are the velocity components in the x, y, and z directions, and P and T are the local fluid pressure and temperature. The energy conservation equation used to model heat transfer within the solid copper regions is:

$$\frac{\partial^2 T}{\partial x^2}+\frac{\partial^2 T}{\partial y^2}+\frac{\partial^2 T}{\partial z^2}=0 \quad (4.14)$$

4.3.5 Domain Discretization

One additional advantage of the unit cell approach is that its simplified geometry offers the potential for a structured mesh. This mesh type is preferable to a free tetrahedral type mesh as it reduces the number of mesh elements, facilitates the incorporation of boundary layer elements, and permits higher order domain discretization.

The mesh layout used in the current numerical study is shown in Fig. 4.6. The most important parameters are the number and distribution of elements along the channel width. Rather than creating boundary layer elements along the channel walls to accurately capture velocity profiles, a symmetric geometric sequence was utilized to define the size of consecutive elements. In other words, the specified number of elements were geometrically sequenced along the channel width such that the smallest elements fell closer to the channel walls.

In COMSOL, this geometric sequence is dependent upon a parameter referred to as the elemental ratio r. The elemental ratio is defined as the ratio of the largest element size within a domain to the smallest. Referring to the sample symmetric geometric sequence in Fig. 4.7, the elemental ratio would be E_3 divided by E_1. The software then uses this condition to calculate the common ratio r and scaling factor a which are commonly used to define a geometric sequence as follows:

$$a\,, ar\,, ar^2\,, ar^3\,, ar^4\,, \ldots\ ar^{n-1} \quad (4.15)$$

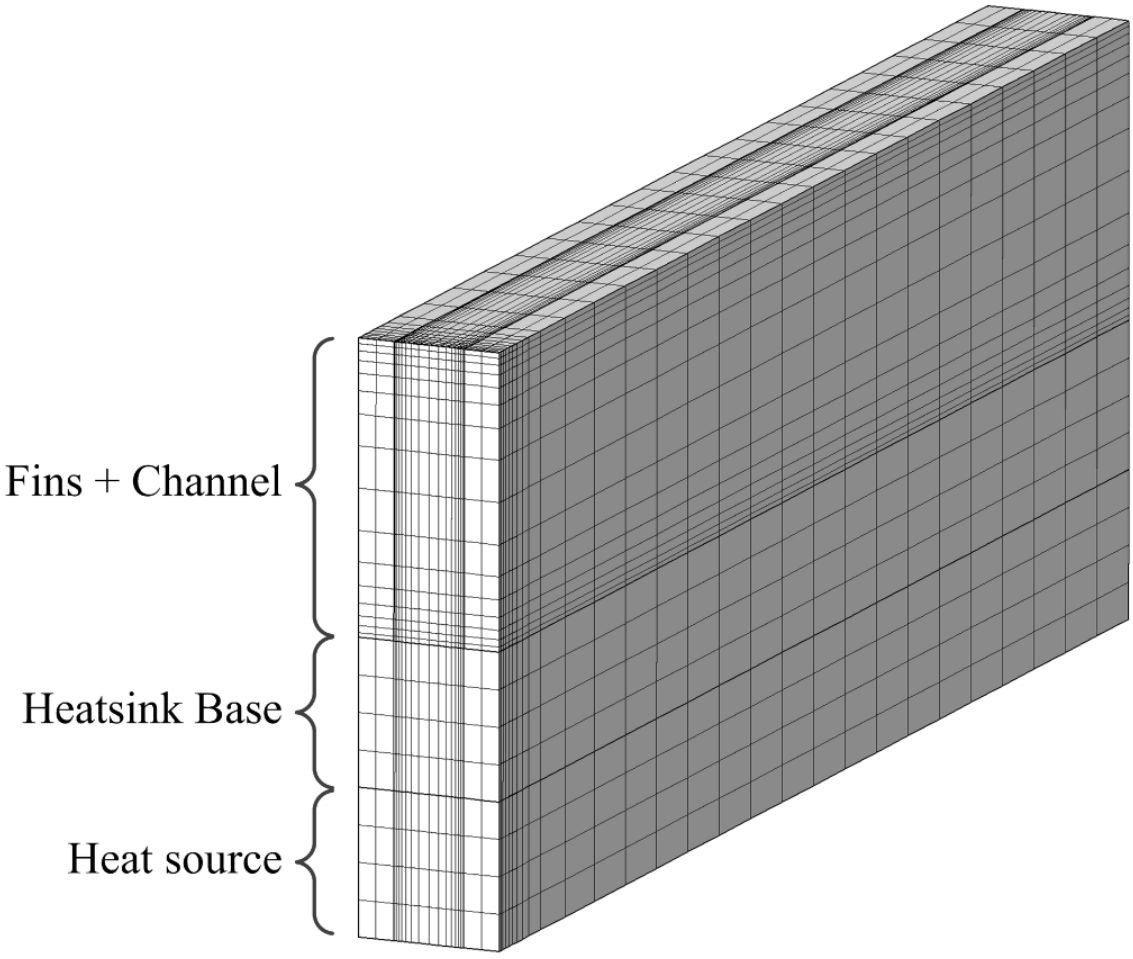

Fig. 4.6 – Mesh layout for unit cell numerical model

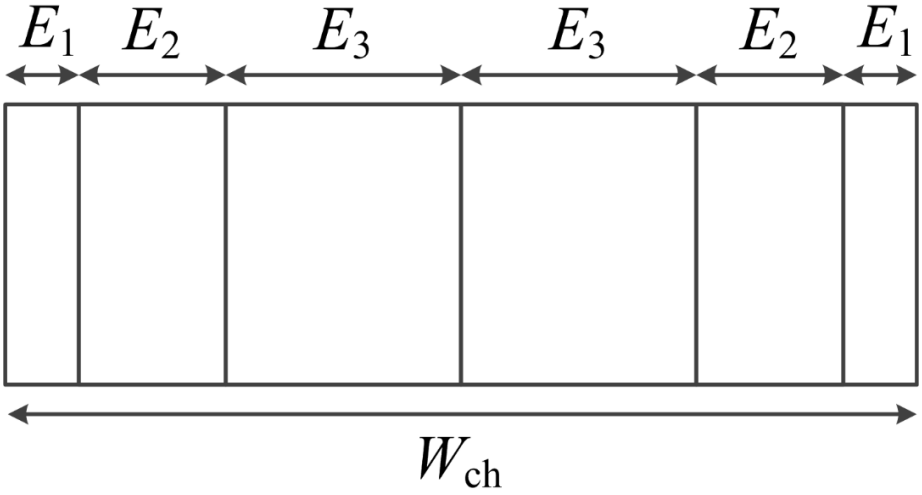

Fig. 4.7 – Distribution of geometric mesh elements

The above sequence defines the size of each element along the channel width up until the center of the channel; after which the element size reduces symmetrically as seen in Fig. 4.7. Based on a convergence study examining the maximum wall temperature and channel pressure drop, an elemental ratio *r* of 8 was deemed acceptable. The convergence plots associated with this study are shown in Appendix A.

This alternative to boundary layer elements provides more control over the mesh structure and thus facilitates parametric studies in which the channel width varies. A similar structure was used to generate mesh elements along the channel height. Elements along the channel length were equally sized as no steep velocity profiles were expected in the direction of flow. Boundary layer elements were added at the inlet side of the channel such that the solver would better capture phenomena within the entrance region. These elements may be observed upon close examination of Fig. 4.6.

With regards to the copper domains, two mesh elements were generated across the fin widths and four were generated across the base and heat source heights. This low mesh density is acceptable as only conductive heat transfer is modelled within these regions. This phenomenon can be accurately captured by a small number of linearly discretized elements. The procedure for generating the complete mesh involved first creating a two dimensional surface mesh of the top surface (*i.e.* the top surface of the channel and fins) and then sweeping this layout down to create a three dimensional mesh based on the constraints highlighted above.

Various mesh convergence studies were performed in order to identify the ideal number of elements along each channel dimension. These studies also provided insight into how these mesh parameters must be adjusted as the channel dimensions themselves are varied. In other words, eight elements along a 1 mm wide channel may yield a mesh independent solution; however, will this condition hold for 2 mm wide or 0.5 mm wide channels? These studies utilized the maximum wall temperature and the pressure drop across the channel as indicators of convergence. The definition of the maximum wall temperature will be reiterated: it is the maximum temperature along the top surface of the heat source (*i.e.* the surface that contacts the heatsink base).

The results for the mesh convergence study along the channel width are shown in Fig. 4.8. Referring to the maximum wall temperature convergence plot in Fig. 4.8a),

convergence is observed for all channel widths as the number of elements along the channel width increases; although, the specific number of elements required for convergence varies significantly. In the case of a 2 mm channel, there is a 2.02 % relative difference between the maximum wall temperatures at 32 and 64 elements. Whereas in the case of a 0.5 mm channel, this difference is 0.78 % and the relative difference between maximum wall temperatures at 16 and 32 elements is 1.73 %. In the case of a 0.125 mm channel, the relative differences are even lower; 0.15 % between 8 and 16 elements and 1.21 % between 4 and 8 elements.

This pattern is also evident by simply observing the figure. At smaller channel widths, the predicted maximum wall temperature converges at a lower number of elements compared to larger channel widths. The same pattern is observed when examining the pressure drop convergence plot shown in Fig. 4.8b). The variation between the predicted pressure drops at 2 and 8 elements gradually decreases as the channel width shrinks. Clearly, the requisite number of elements for a mesh independent solution reduces as the channel width is decreased.

This outcome may be explained by examining the velocity distribution across the channel width. A minimum number of elements are necessary near each side wall in order to accurately model velocity and temperature profiles within boundary layers. The remainder of the elements are necessary to model flow and heat transfer within the central region where the fluid velocity and temperature are virtually uniform. As the channel width decreases, so does the width of this central region; hence reducing the overall number of elements required.

Regardless of the reasons, channels as large as 2 mm require more than 64 elements along their widths for a converged solution; while the smallest channels yield mesh independent solutions with as low as 8 elements across their widths. In order to incorporate this variance within the parametric solver, the number of elements along the channel width was defined as follows:

$$N_{\mathrm{Ew}} = 2 \cdot \mathrm{round}\left(\frac{8+16W_{\mathrm{ch}}}{2}\right) \tag{4.16}$$

where the unit of the channel width W_{ch} is in millimeters. This equation has no physical significance. It simply yields larger values at higher channels widths and a minimum value of 8 elements as the channel width approaches zero.

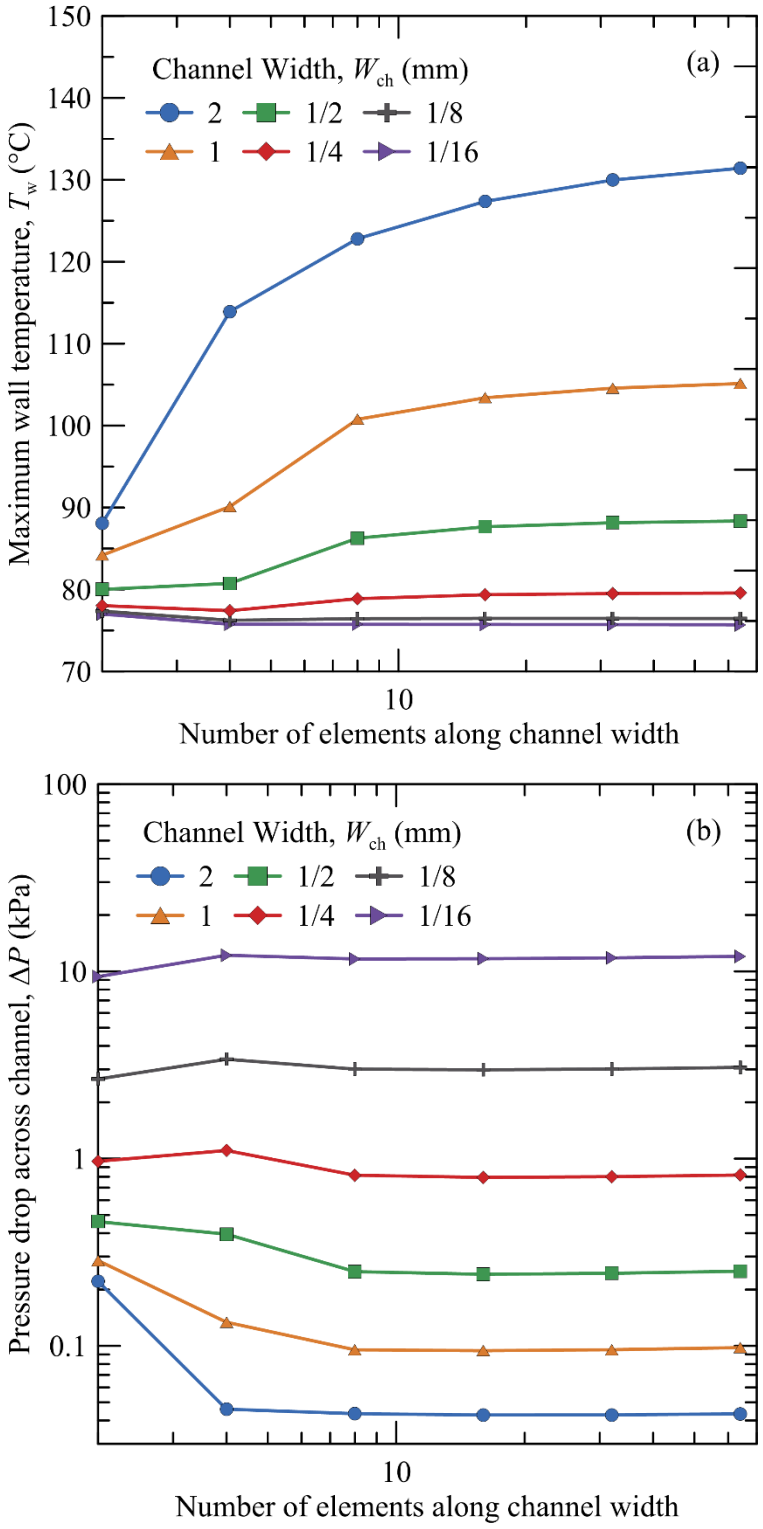

Fig. 4.8 – Mesh convergence study along channel width, H_{ch} = 4 mm, L_{ch} = 2 cm, $T_{in,hs}$ = 60 °C, q_{total} = 300 W, Q_{hs} = 1 L/min, R''_{TIM} = 0.1 K·cm²/W

Similar mesh convergence studies have been performed along the channel height and length. Solely the conclusions of these studies are presented here; the convergence plots are provided in Appendix A. Along the channel height, 16 elements were sufficient for acquiring mesh independent wall temperatures and pressures for all channel heights examined. Along the channel length, an elements size of 1 mm was sufficient for acquiring a converged solution. A summary of the mesh properties is provided in Table 4.2.

Table 4.2 – Properties of mesh used in numerical simulations

Dimension	No. of Elements	Element Size
Channel Width, W_{ch}	8 - 40	-
Channel Height, H_{ch}	16	-
Channel Length, L_{ch}	-	1 mm
Fin Width, W_f	2	-
Base/Source Thickness, t_b & t_{source}	4	-
Full Mesh	**8,064 – 29,568**	**-**

4.3.6 Parametric Study Results and Discussion

With a convergent numerical model established, the process of designing and optimizing a liquid cooled heatsink culminated in Fig. 4.9. These plots simply exhibit the predicted maximum wall temperature and channel pressure drop associated with various combinations of channel width and height. Remaining geometric and boundary parameters were held constant at either their most conservative or most commonly used values.

A heat generation rate q_{total} of 300 W corresponds to the maximum heat load of a high performance computing processor expected by the year 2020 (ASHRAE, 2012). An inlet water temperature $T_{in,hs}$ of 60 °C corresponds to the highest temperatures used in recent industry applications (Zimmermann, Meijer, et al., 2012). A volumetric flowrate, Q_{hs}, of 1 L/min is commonly used in experimental studies of a similar scope. The thermal interface material thermal resistance R''_{TIM} was actually liberally maintained at a low value of 0.1 K·cm^2/W. The thermal resistance of the TIM used in experimental studies (TGREASE 880 from Laird Technologies®) is 0.09 K·cm^2/W at a contact pressure of 10 psi. Finally, the channel length L_{ch} and the overall heatsink base width W_b were set equal to the anticipated heat source width of 2 cm.

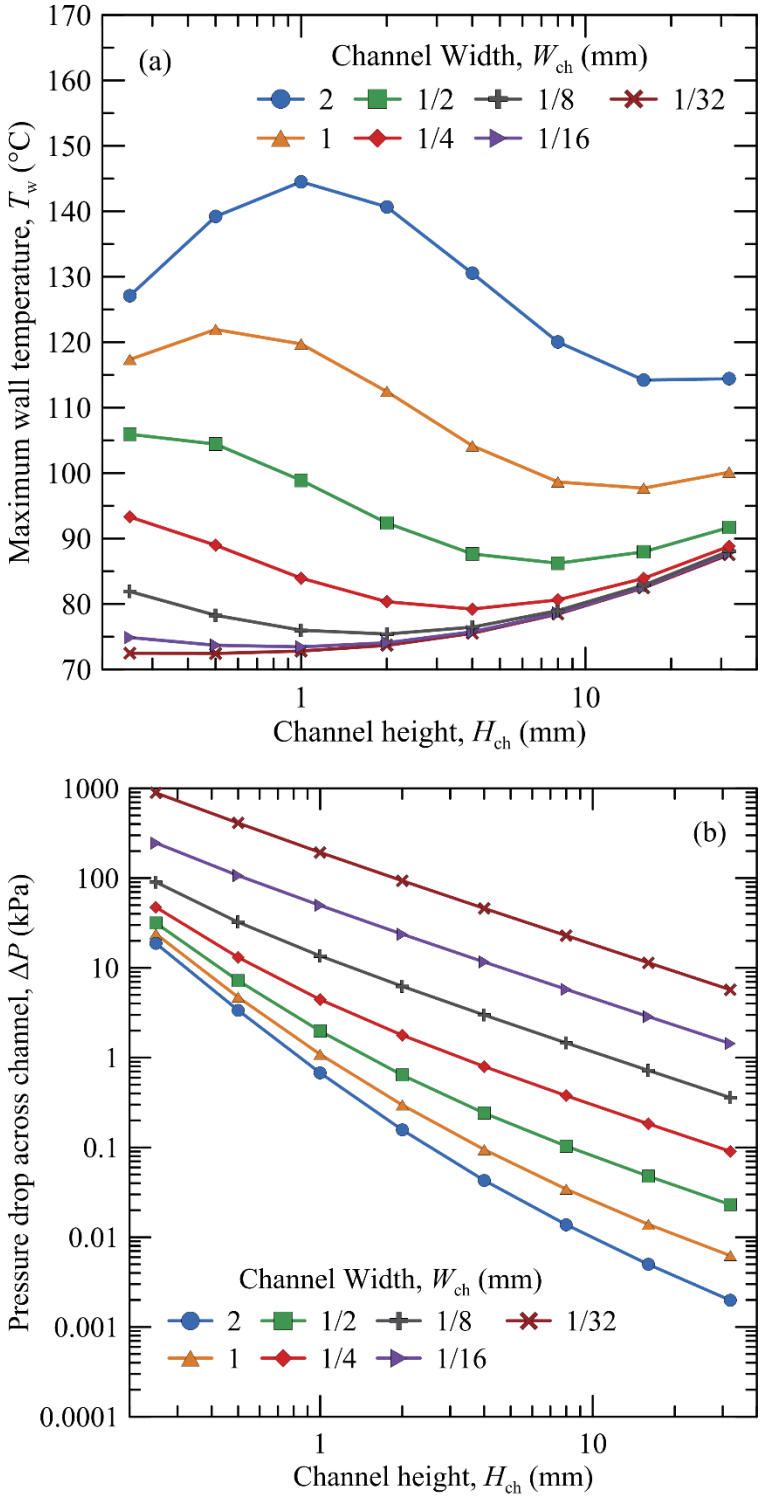

Fig. 4.9 – Parametric study of heatsink channel width and height, L_{ch} = 2 cm, $T_{in,hs}$ = 60 °C, q_{total} = 300 W, Q_{hs} = 1 L/min, R''_{TIM} = 0.1 K·cm²/W

Focusing first upon Fig. 4.9a), the predicted maximum wall temperature curves shift downward as the channel width is reduced regardless of their specific variation with

channel height; this was of course expected. As the channel width is reduced and the number of channels are consequently increased, the convective heat transfer surface area increases proportionally to the number of channels; thus reducing the overall thermal resistance of the heatsink as well as the maximum wall temperature.

In addition to the heat transfer area, it would be interesting to see how the average fluid velocity contributes to this downward shift in temperature. It may seem intuitive that the average fluid velocity within a single channel should increase as the channel width is reduced. However, since the overall flowrate through the heatsink Q_{hs} is maintained constant, the average channel velocity actually converges on a maximum value. This outcome is demonstrated by redefining the average channel velocity solely as a function of the number of channels:

$$V_{\mathrm{in,hs}} = \left(2 - \frac{1}{N_{\mathrm{ch}}}\right)\frac{Q_{\mathrm{hs}}}{W_{\mathrm{b}}H_{\mathrm{ch}}},\ N_{\mathrm{ch}} = 3, 5, 7, 9 \ldots \tag{4.17}$$

There is little explanation necessary here. As the number of channels increases, the coefficient of the above equation quickly approaches a maximum value of 2 while all other parameters remain constant. This indicates that at initially larger channels widths (*i.e.* fewer channels), a reduction in the channel width not only enlarges the heat transfer area but also increases the average fluid velocity within each channel; thus further reducing the overall thermal resistance of the heatsink by increasing the convective heat transfer coefficient. At lower channel widths (*i.e.* more channels), a further reduction in the channel width merely serves to increase the heat transfer area.

The preceding arguments have been related to the downward shift in temperature resulting from changes in the channel widths. It is also interesting to address the predicted variations in temperature resulting from changes in the channel height. Starting on one extreme end of the spectrum with a channel width of 2 mm and a channel height of 0.25 mm (*i.e.* the left-most point on the curve), it is predicted that an increase in the channel height initially raises the maximum wall temperature while, beyond a channel height of 2 mm, the wall temperature is reduced.

One possible explanation for this outcome may be that, initially, the large channel width (*i.e.* fewer channels) implicates a small heat transfer area while the miniscule channel height implicates a high fluid velocity. Consequently, a slight increase in the channel height geometrically reduces the fluid velocity (*i.e.* velocity is inversely proportional to the

channel height) while only linearly increasing the convective heat transfer area. The result is an exponential reduction in the heat transfer coefficient due to decreasing velocity and a linear expansion of the heat transfer area that is insufficient to prevent an overall rise in the heatsink thermal resistance. Beyond a height of 2 mm, the fluid velocity is reducing at a slower rate than that with which it was initially while the convective heat transfer area is now sufficiently large to overcome the negative effects of low velocities.

These claims may be justified by examining the variation of the heat transfer coefficient of the heatsink as plotted in Fig. 4.10. This heat transfer coefficient was calculated based on the area and heat load corresponding to a single unit cell as follows:

$$h_{\mathrm{hs}} = \frac{q_{\mathrm{source}}}{A_{\mathrm{s}}(T_{\mathrm{w}} - T_{\mathrm{in,hs}})} \tag{4.18}$$

where q_{source} is the heat load corresponding to a single unit cell, A_{s} is the convective surface area of a unit cell, T_{w} is the maximum wall temperature predicted numerically, and $T_{\mathrm{in,hs}}$ is the inlet temperature of the heatsink. The convective surface area A_{s} was calculated as follows:

$$A_{\mathrm{s}} = L_{\mathrm{ch}}(W_{\mathrm{ch}} + 2H_{\mathrm{ch}}) \tag{4.19}$$

where L_{ch}, W_{ch}, and H_{ch} are the length, width, and height of a single heatsink channel.

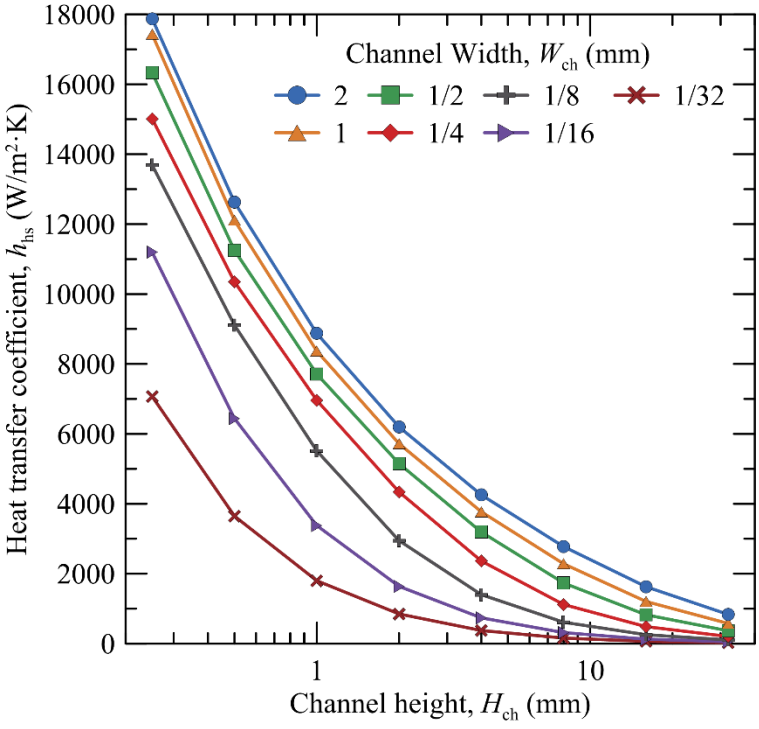

Fig. 4.10 – Heat transfer coefficient of the heatsink for different channel widths and heights, L_{ch} = 2 cm, $T_{\mathrm{in,hs}}$ = 60 °C, q_{total} = 300 W, Q_{in} = 1 L/min, R''_{TIM} = 0.1 K·cm²/W

As the channel height is increased, the exponential-shaped reduction of the heat transfer coefficient in Fig. 4.10 is evident. Moreover, the heat transfer coefficient corresponding to the smallest channel width is actually the lowest at all channel heights. Yet the smallest channel width yielded the lowest wall temperatures in Fig. 4.9a). These two outcomes are reconciled by the fact that the smallest channel width also yielded the highest total heatsink convective heat transfer area which, in turn, resulted in the lowest overall thermal resistances.

It is also interesting to note the important role of the fin width. Reducing the fin width causes a leftward shift in the range of channel heights over which increasing the channel height has a positive effect. At a channel width of 2 mm (*i.e.* also a fin width of 2 mm) for instance, increasing the channel height reduces the maximum wall temperature as long as the initial channel height was between 1 and 10 mm. At a fin width of 1 mm, this channel height range is between 0.5 and 4 mm. At a fin width of 0.25 mm, this range is between 0.25 and 2 mm.

This observation essentially shows that taller fins (*i.e.* taller channels) are only beneficial when the fins and channels are wide. Wider fins facilitate conductive heat transfer while reducing the overall convective heat transfer area. As a result, the fin and channel height must be increased in order to compensate for this reduced area. At the other extreme end of the spectrum with a channel width of 1/32 mm and a channel height of 0.25 mm, the miniscule channel widths (*i.e.* many channels) implicate an initially large convective heat transfer area such that any increase in the channel height only serves to reduce the heatsink thermal resistance by lessening the fluid velocity.

Justifying the predicted pressure losses is much less arduous. Referring to Fig. 4.9b), it is observed that the pressure drop across the channel escalates as the channel width and height are reduced. This relationship is intuitive. As the flow area shrinks and the average fluid velocity increases, the contributions of surrounding wall friction (in the form of shear stress) and fluid viscosity are amplified. For a more mathematically instructive explanation, one must simply invoke the following laminar form of the Darcy-Weisbach equation:

$$\frac{\Delta P}{L_{\mathrm{ch}}} = \frac{64}{\mathrm{Re}}\frac{\rho}{2}\frac{{V_{\mathrm{in}}}^2}{D_{\mathrm{h}}} = 32\mu\frac{V_{\mathrm{in}}}{{D_{\mathrm{h}}}^2} \tag{4.20}$$

where D_h is the hydraulic diameter of the channel and ΔP is the pressure drop across the channel. Reducing the channel height increases the average fluid velocity and decreases the hydraulic diameter. The effects upon the pressure drop are clear from the above equation. Reducing the channel width, on the other hand, solely impacts the pressure drop by decreasing the hydraulic diameter. As was proven earlier in this section, reducing the channel width actually bears little impact upon the average fluid velocity.

Although the channel pressure drop behaves as expected, it is important to note that only a unit cell has been modelled. The significance here is that the additional pressure drop associated with the inlet/outlet regions of a heatsink are not accounted for. The numerical study presented at ASME, in which a full three dimensional heatsink was modelled, has shown that this additional pressure drop is roughly 0.25 kPa for a flowrate of 1 L/min (Kheirabadi & Groulx, 2016a).

4.3.7 Validation against Experimental Results

Prior to discussing the final heatsink design, the effectiveness of the numerical model is examined by comparing numerically predicted wall temperatures with experimentally measured values. This comparison is shown in Fig. 4.11 for operating conditions listed in the figure caption. In order to attain a direct comparison between the two sets of results, the inlet temperature of the heatsink in the numerical simulations was set equal to the heatsink inlet temperature measured experimentally. These heatsink inlet temperatures decreased linearly from 39.8 to 38.3 ºC as the total flowrate through the heatsink increased from 0.3 to 1.5 gal/min (1.1 to 5.7 L/min).

It may be established from Fig. 4.11 that the numerical results correlate well with experimental measurements. At the lowest flowrate of 0.3 gal/min (1.1 L/min), the numerical model underestimates the maximum wall temperature by only 3.0 % based on numerically predicted and experimentally measured maximum wall temperatures of 73.9 and 74.9 ºC, respectively (this percent difference was conservatively calculated relative to the heatsink inlet temperature). At a flowrate of 1.5 gal/min (5.7 L/min), this difference rises to 14.5 % based on numerically predicted and experimentally measured maximum wall temperatures of 61.5 and 64.9 ºC.

The fact that the numerical model always underestimates the maximum wall temperature is likely caused by the thermal resistance of the thermal interface material

R''_{TIM} being underestimated in numerical simulations. This thermal resistance was taken to be 0.1 K·cm^2/W in numerical simulations. This number was based upon the highest thermal resistance values provided within datasheets for TGREASE 880 from Laird Technologies. The actual value of this thermal resistance was likely greater during experimentation which may have been due to smaller contact pressures between the heatsink base and heat source. Additionally, the average roughness of these contacting surfaces was definitely greater than those of polished surfaces often used by manufacturers to evaluate the performance of their thermal pastes.

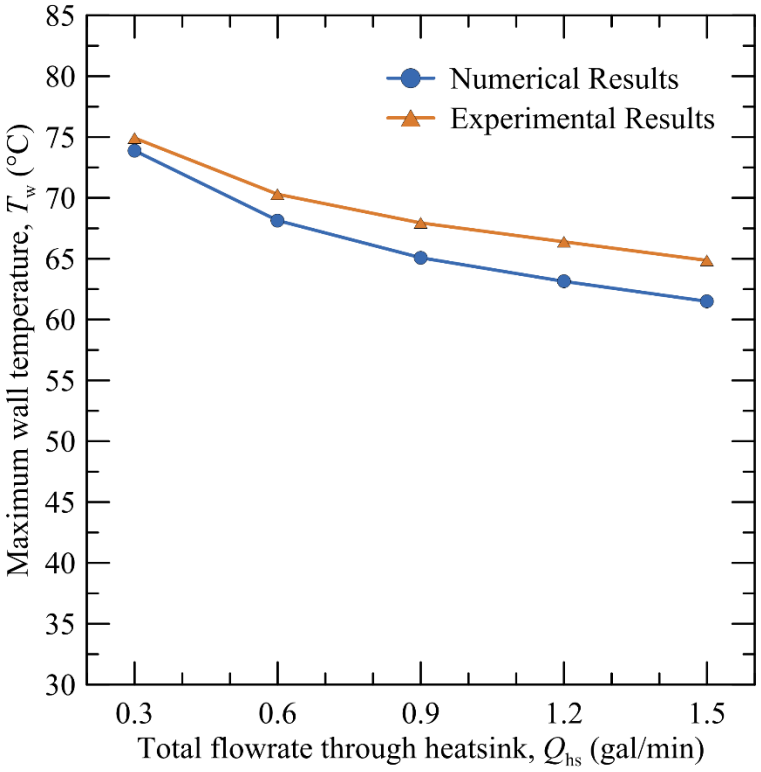

Fig. 4.11 – Comparison of numerically and experimentally derived wall temperatures, q = 330.4 W, $T_{in,ext}$ = 30 °C, W_{ch} = 0.5 mm, H_{ch} = 2.3 mm, L_{ch} = 2 cm, R''_{TIM} = 0.1 K·cm^2/W

4.3.8 Selection of Channel Dimensions

With the parametric numerical simulations completed, the temperature and pressure drop predictions were used to design an appropriate heatsink for experimentation. The aim was to select a combination of channel width and height that would minimize the maximum wall temperature without necessitating an unpractically large pressure drop. Given that the

current system was being design for installation within rackmount servers, which are at least 1.75 in. (4.5 cm) thick, the size and head of the pump were major limiting factors.

An additional concern was of course the manufacturability of the heatsink channels. CNC machining was the preferred method of fabrication given the facilities immediately available to the author. Incidentally, wider channels were preferable as they reduced the requisite machining time. This relationship holds true due not only to the reduced number of channels, but also to the increased cutting speeds and depths available to larger diameter mill bits. Although it is beyond the scope of this study to comment on manufacturing on an industrial scale, it is reasonable to assume that larger channel widths would facilitate production regardless of the methods involved.

In view of these constraints, a channel width of 0.02 in. (0.5 mm) was selected. The maximum possible channel height was consequently 2.3 mm. This dimension was limited by the allowable cutting depth of a 0.02 in. (0.5 mm) diameter mill bit. According to Fig. 4.9, these dimensions yield a maximum wall temperature of 92 °C and a channel pressure drop of 0.6 kPa at a flowrate of 1 L/min, a heat load of 300 W, and a water inlet temperature of 60 °C. The predicted pressure drop raised no concerns; however, the predicted wall temperature of 92 °C exceeded the desired limit. Referring back to the start of the chapter, the aim of numerical modelling was to dimension the channels such that the maximum wall temperature would be maintained below 85 °C at the most extreme operating conditions. Considering the fact that the unit cell method provides a conservative estimate of the wall temperature and that, during experimentation, the flowrate and inlet temperature were varied to compensate for any such shortcomings, a predicted maximum wall temperature of 92 °C was deemed acceptable.

This decision was further reinforced by examining the subsequently smaller and larger channel widths; namely channel widths of 0.25 and 1 mm respectively. A 0.01 in. (0.25 mm) diameter mill bit permits a maximum cutting depth of 1.2 mm; which translates to a maximum possible channel height of 1.2 mm. As per Fig. 4.9, such a channel size would yield a wall temperature of 84 °C and a channel pressure drop of 4.5 kPa at a flowrate of 1 L/min, a heat load of 300 W, and an inlet temperature of 60 ºC. Although the predicted wall temperature was reduced, the projected pressure drop was excessive given the fact that flowrates as high as 6 L/min were tested during experimentation. Furthermore, a

reduction in the wall temperature from 92 to 84 °C (between the 0.5 and 0.25 mm channel widths) was deemed an unfit trade-off for the loss of manufacturability associated with the smaller channel size.

A 0.04 in. (1 mm) diameter mill bit permits a maximum cutting depth of 5 mm; and thus a maximum channel height of 5 mm. As per Fig. 4.9, these dimensions correspond to a wall temperature of 103 °C and a pressure drop of 0.08 kPa. This predicted wall temperature is unacceptably excessive and the loss in manufacturability by reducing the channel width to 0.5 mm was therefore deemed a fit trade-off for a wall temperature reduction from 103 to 92 °C.

4.4 Thermal Contact Heat Exchanger Design

The finned thermal contact heat exchanger was designed using the same numerical methodology outlined above; albeit with a different geometry. As shown in Fig. 4.12, the unit cell geometry for the finned thermal contact heat exchanger simply encompassed two individual channels attached at their bases. One channel represented the internal side of the heat exchanger while the other represented external side. As a result, the previous conclusions concerning the mesh convergence study should remain valid; as should all equations used to calculate geometric parameters and operating conditions.

The volumetric flowrates through both heat exchangers Q_{int} and Q_{ext} were maintained at 1 L/min; however, opposing directions of flow were used as this strategy is well understood to improve heat transfer. Given the operating conditions allotted to the heatsink in the previous section ($T_{in,hs}$ = 60 °C, Q_{hs} = 1 L/min, and q_{total} = 300 W), the heatsink outlet temperature was calculated to be 64.3 °C using a simple energy balance. Since the heatsink outlet feeds into the internal heat exchanger inlet, the inlet temperature of the internal heat exchanger $T_{in,int}$ was accordingly set to 65 °C (64.3 °C rounded up). The inlet temperature of the external heat exchanger $T_{in,ext}$ was optimistically set to 50 °C as a starting point; this ultimately proved more than sufficient. Similar to the heatsink simulations, a thermal contact resistance of 0.1 K·cm^2/W was added at the contact interface between the internal and external heat exchanger plates. The channel length L_{ch} in the current simulations was 6 in. (15.2 cm) and the overall heat exchanger width W_b was 1.75 in (4.4 cm). These dimensions are further discussed in the next chapter.

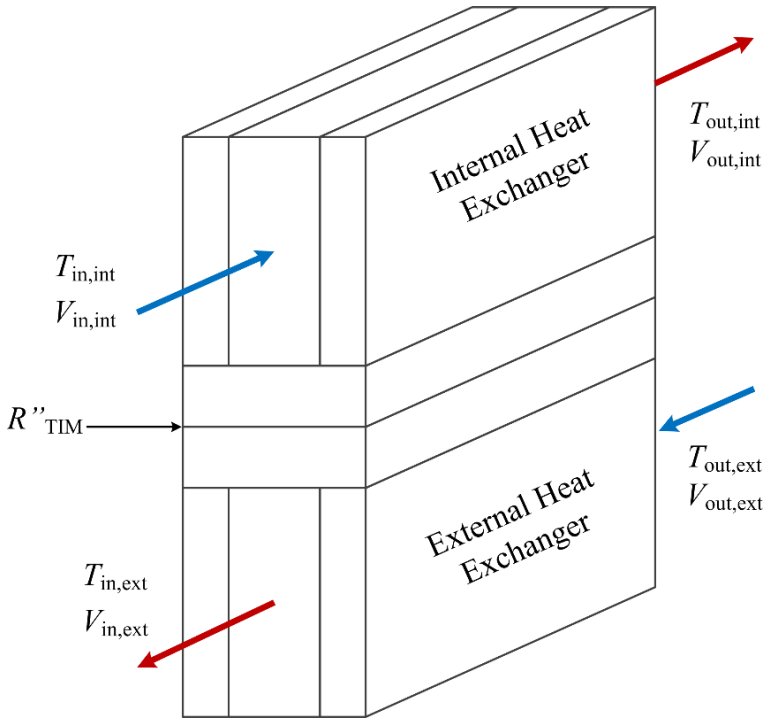

Fig. 4.12 – Schematic of boundary conditions imposed upon the straight channel TCHx unit cell model

Whereas the goal in designing the heatsink was to ensure that the maximum wall temperature did not critically exceed 85 °C, the goal in designing the thermal contact heat exchanger was to ensure that a heat transfer rate of at least 300 W would be attained with the given inlet temperatures of 65 and 50 °C. If no combination of channel width and height produced this desired outcome, then the external inlet temperature would have been reduced from 50 to 40 °C and the simulations repeated. As shown in Fig. 4.13a), such iterations were not necessary.

This figure exhibits the total heat transfer rate across the thermal contact heat exchanger for different combinations of channel width and height. The first interesting observation is that the entirety of this plot is a vertically mirrored image of the wall temperature plots shown in Fig. 4.9a); the reason for which is simple. As the heatsink thermal resistance decreases (regardless of the cause), so does the maximum wall temperature shown in Fig. 4.9a). On the other hand, as the thermal resistance of the thermal contact heat exchanger increase, the overall heat transfer rate shown in Fig. 4.13a) decreases. The wall temperature and the heat transfer rate shift in opposite direction for an identical variation in the thermal resistance.

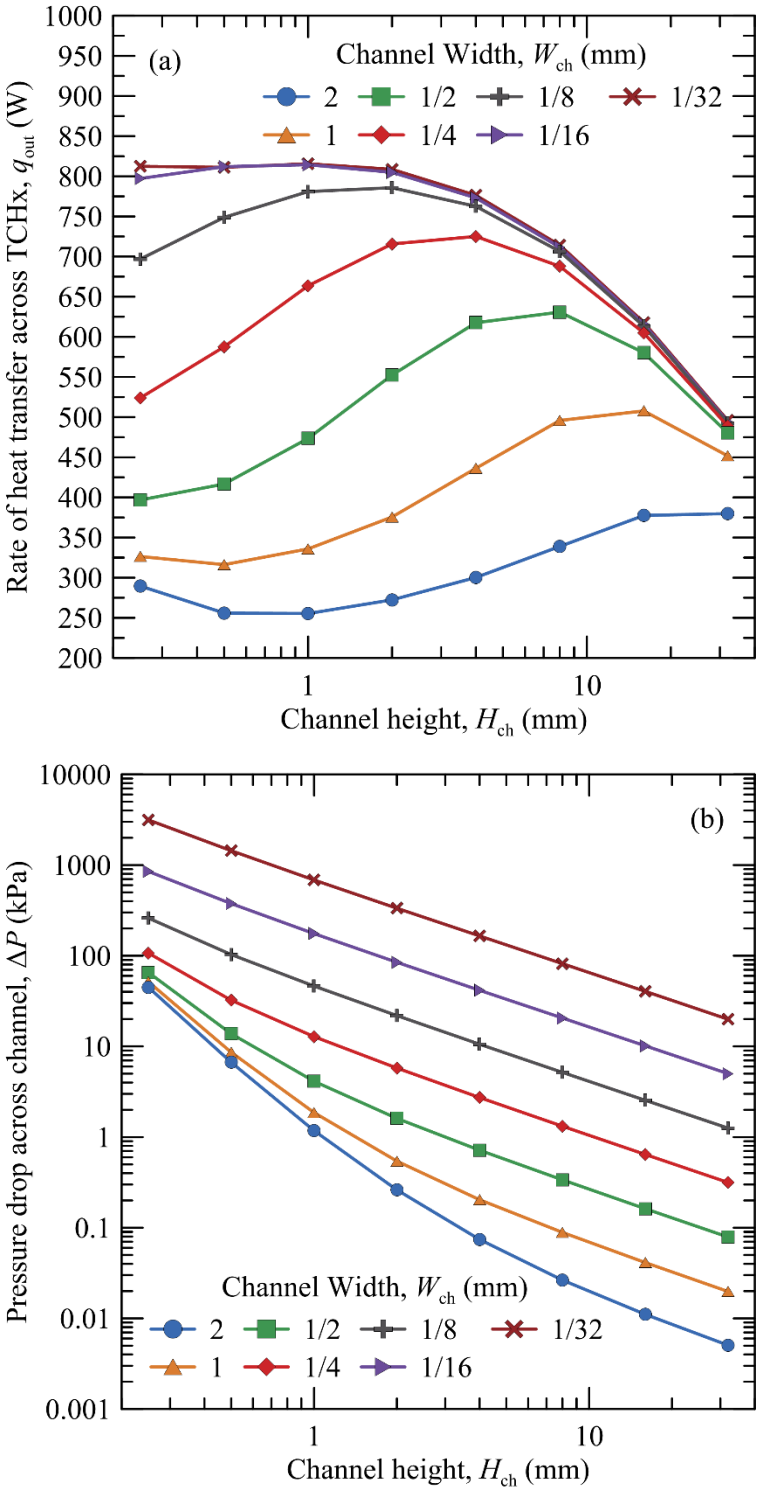

Fig. 4.13 – Parametric study of straight channel TCHx channel width and height, L_{ch} = 6 in., $T_{in,int}$ = 65 °C, $T_{in,ext}$ = 50 °C, Q_{int} = Q_{ext} = 1 L/min, R''_{TIM} = 0.1 K·cm²/W

These opposing relationships would explain why the curves in the two figures generally shift in opposite directions for identical shifts in channel width and height.

However, the fact that even the subtle variations in the curves are mirrored so impeccably indicates that the causes of the change in thermal resistance must also be identical in both cases; leading the discussion pertaining to Fig. 4.9a) to hold for the current figure as well. None of these conclusions come as a surprise of course; the geometries in both simulations were identical and it is reasonable to assume that the same is true for the predicted heat transfer and flow phenomena.

Referring now to the thought process from the previous section which was used to select the optimal heatsink channel dimensions, the optimal heat exchanger channel dimensions were reasoned to be 0.04 in. (1 mm) in width and 4 mm in height. Revisiting Fig. 4.13, these dimensions correspond to a heat transfer rate of 436 W and a pressure drop of 0.2 kPa. Just as in the previous section, the subsequently smaller channel width of 0.5 mm (which would be limited to a channel height of 2.3 mm) would have increased the heat transfer rate to roughly 550 W and the pressure drop to 1.6 kPa. Although 550 W is preferable to 436 W, the harm to manufacturability was deemed an unfair trade-off. The thermal contact heat exchangers were expected to be substantially longer and wider than a chip-level heatsink and, as a result, the largest acceptable channel width was always preferable in order to minimize machining time. The subsequently larger channel width of 2 mm (which would be limited to a channel height of 8 mm to be generous) yielded a heat transfer rate of 339 W and pressure drop of 0.03 kPa. The heat transfer rate was only about 10 % greater than the desired minimum heat transfer rate of 300 W. By taking into consideration the possibility that the numerical model may have been underestimating thermal resistances, a heat transfer rate of 339 W was deemed unacceptable.

4.5 Concluding Remarks

This chapter presented a numerical method of estimating the performance of liquid cooled heatsinks and heat exchanger plates. The method employed a quasi-symmetric unit cell geometry consisting of a single flow channel. This simplified approach permitted a parametric evaluation of the impact of various channel width and height combinations upon thermal performance. The results of these evaluations were necessary in order to design appropriate and effective heatsinks and heat exchangers for the subsequent experimental evaluations.

Based upon these parametric studies, it was established that the ideal heatsink channel width and height should be 0.5 and 2.3 mm, respectively. This decision considered not only the numerical predictions, but also the manufacturability of such small channels and the limitations of fabrication tools available. Based upon similar parametric studies surrounding one particular thermal contact heat exchanger design (the straight channel TCHx), it was established the ideal channel width and height of this heat exchanger plate should be 1.0 and 4.0 mm, respectively.

Chapter 5 - Experimental Setup and Procedure

To reiterate, the ultimate purpose of experimentally evaluating the proposed cooling system was to quantify its thermal performance relative to a conventional water cooling system which uses fluidic connectors. As a result, the experimental setup encompassed not only the thermal contact heat exchanger which is the central topic of this research, but also a heatsink attached to a copper heat source mimicking heat dissipation at the chip-level. This arrangement permitted the sought after comparison between the proposed cooling system and a conventional water cooling system (this point will be further addressed in the following sections). Just as crucial, however, the inclusion of the heatsink provided grounds for a more comprehensive set of recommendations to Raytheon Canada. For instance, the pressure drop measured across the heatsink served as an indicator for the size and type of pump required for industry application. A detailed review and justification of the experimental apparatus is now provided.

5.1 Overview of Experimental Setup

The complete diagram of the experimental setup is presented in Fig. 5.1; this schematic is followed by an image of the complete experimental setup in Fig. 5.2. Appropriately, the setup contained two circulation loops. The top loop in Fig. 5.1 reflected the portion of the cooling system internal to the server while the bottom loop replicated cooling at the facility level. Heat generated by cartridge heaters at Test Section 1 was transferred from the internal heat exchanger plate to the external heat exchanger plate at Test Section 2 and was ultimately expelled to the ambient through a recirculation chiller. Since heat transfer to the ambient occurred in the external loop, no fluid reservoir was incorporated within the internal loop. A reservoir would have increased the thermal mass of the fluid and thus lengthened the duration of transient processes. Moreover, a reservoir would have presented an additional source of heat loss without proper insulation.

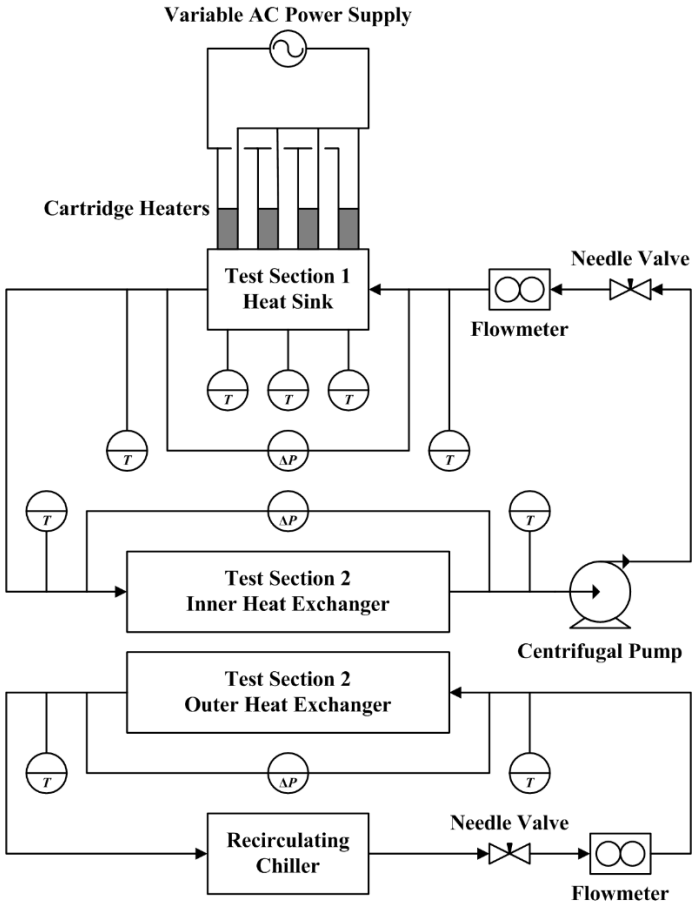

Fig. 5.1 – Process diagram describing the experimental setup

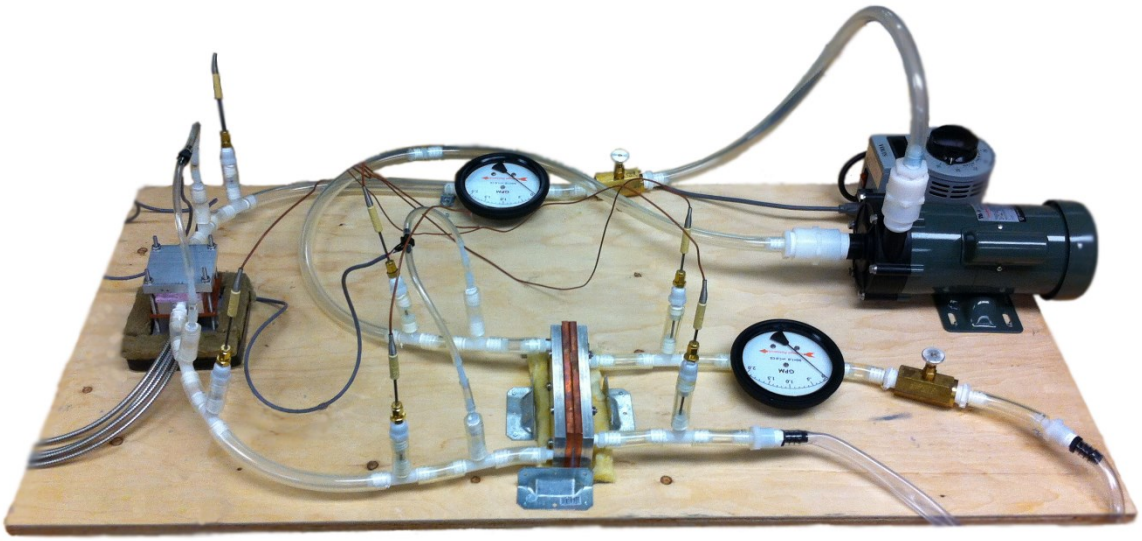

Fig. 5.2 – Image of complete experimental setup

Flow within the internal loop was induced by the 260 W AC centrifugal magnet pump shown in Fig. 5.3 (model no. MD-100RLT from Iwaki, Inc.) with a maximum head of 39

ft. (117 kPa) and a maximum flowrate of 35.6 gal/min (135 L/min). This is clearly an absurdly large pump for installation within a server. This level of power was necessary during experimentation in order to overcome head losses across the needle valve, flowmeter, and the multitude of fittings at each junction. A substantially smaller pump will suffice for maintaining flow within a server containing only the heatsink and thermal contact heat exchanger.

Fig. 5.3 – Image of centrifugal pump used in the internal flow loop

The flowrate was regulated by a standard needle valve and was measured using the mechanical piston-type flowmeter shown in Fig. 5.4 (model no. 2221-S1021 from Orange Research, Inc.). This mechanical flowmeter was preferred over digital alternatives because it possessed the appropriate combination of properties; its aluminum body permitted fluid temperatures up to 70 °C (which was not expected to be exceeded), it measured a flowrate range of 0.2 to 2 gal/min (0.75 to 7.5 L/min, which was precisely the range of interest in this study), it operated with an uncertainty of ± 2 % (which is comparable to digital alternatives), and it was relatively inexpensive (180 USD against more than 600 USD for digital alternatives). Furthermore, lead times on suitable digital alternatives were unacceptable given time constraints.

Flow within the external loop was induced by the built-in pump of the recirculation chiller shown in Fig. 5.5 (model no. Polystat 3C15++ from Cole-Parmer®) and the flowrate was regulated and measured using a needle valve and flowmeter identical to those used in the internal loop. In contrast to the internal loop, the external loop consisted of a 15 L fluid

reservoir integrated within the recirculation chiller. The temperature of this bath was maintained at various set points by the chillers' built-in heating and cooling control systems; thus permitting control of the fluid temperature exiting the chiller. This chiller model uses refrigerant R404a to dissipate heat at a rate up to 800 W within a temperature range of -35 to 200 ºC.

Fig. 5.4 – Image of mechanical flowmeter used in internal and external flow loops

Fig. 5.5 – Image of recirculation chiller used in the external flow loop

Temperature measurements were made at the inlets and outlets of the heatsink and the thermal contact heat exchanger plates. A total of six grounded K-type thermocouples (model no. KTSS-18G-6 from Omega®) where immersed in-line with the flow using simple tee fittings as shown in Fig. 5.6. Three K-type thermocouples (model no. KTSS-116G-6 from Omega®) were also inserted within Test Section 1 in order to measure the heat source temperature. K-type thermocouples were used for no reason other than availability. Finally, pressure losses across both the heatsink and the internal heat exchanger plate were measured using the 5 psi (34.5 kPa) differential pressure transducers shown in Fig. 5.7 (model no. PX26-005DV from Omega®). The pressure drop across the external heat exchanger plates was redundant as it was identical to that of the internal plate.

Fig. 5.6 – Image of K-type thermocouple and tee assembly

Fig. 5.7 – Image of differential pressure transducer

5.2 Test Section 1

The first test section, shown in both collapsed and exploded configurations in Fig. 5.8, was designed to replicate a processor and heatsink assembly found within a conventional liquid cooled server. An image of the first test section is also shown in Fig. 5.9. The entire assembly was compressed between a set of aluminum base and cover plates (1060 aluminum alloy) with four stainless steel studs and nuts applying pressure. A copper block (110 copper alloy) which housed four cartridge heaters and three thermocouples was placed directly on top of the aluminum base in order to simulate the heat source. In order to centrally align the copper block, a 0.5 mm deep pocket was machined from the top surface of the aluminum base.

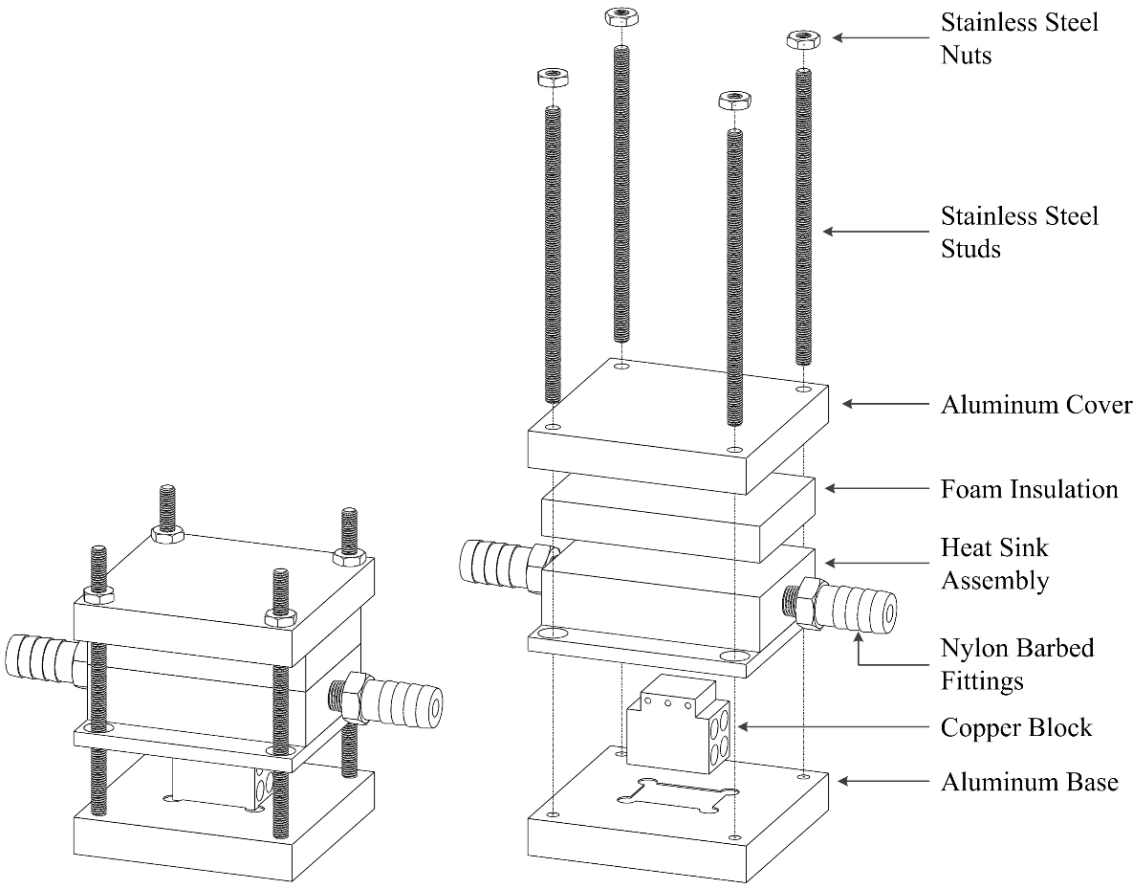

Fig. 5.8 – Schematic of Test Section 1 in collapsed and exploded configurations

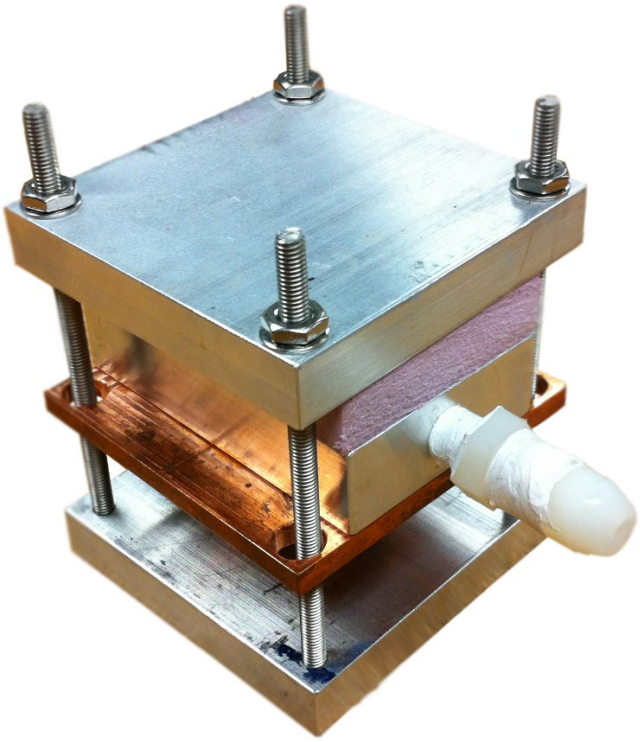

Fig. 5.9 – Image of Test Section 1

The heatsink assembly rested directly atop the copper block with thermal interface material (TGREASE 880 from Laird Technologies®) applied between the contacting surfaces. As mentioned in the previous chapter, the thermal resistance of this thermal paste is 0.09 K·cm^2/W at a contact pressure of 10 psi according to manufacturer datasheets. The surface roughness (R_a value) of the copper block (which had been milled down for flatness) was measured using a digital surface gage (Pocket Surf® from Mahr Federal) to be 1.39 µm while that of the heatsink base (which was stock copper) was measured to be 0.194 µm. Given the scope of the current study, no additional effort was made to measure any contact pressures. Once all components were aligned with the studs, the aluminum cover was forcefully held down while the nuts were hand tightened. As will be shown when discussing repeatability, reassembling the setup in this fashion had little effect on temperature measurements.

A 0.5 in. (1.3 cm) thick layer of foam insulation was placed between the heatsink assembly and the aluminum cover plate. This layer of insulation prevented heat from transferring from the aluminum base through the studs and aluminum cover to the heatsink. Additionally, it may be observed that the clearance holes on the heatsink assembly (through

which the studs passed) were substantially larger in diameter than the studs themselves. This measure was taken to prevent heat transfer from the studs to the heatsink. Once assembled, the entire test section was enclosed on all sides by mineral wool insulation (selected due to its high temperature rating) with appropriate openings for the barbed fittings, thermocouples, and cartridge heaters. Within this enclosure, the copper block was also separately enclosed by mineral wool insulation along its side walls.

Detailed diagrams of the copper block are shown in Fig. 5.10 along with an image shown in Fig. 5.10. First and foremost, the heated surface area was 0.75×0.75 in. (1.9×1.9 cm). The heated surface refers to the portion of the copper block that comes into contact with the heatsink base; or more simply put, it is the top surface of the copper block and the only surface of any significance. It is the temperature of this surface that is indicative of the processor die temperature that this setup is aiming to simulate.

In reality, the internal structure of a chip package differs greatly from a simple copper surface. A simple chip package consists of a heat generating die enclosed by a protective metallic lid which also acts as a heat spreader (ASHRAE, 2012). In high performance computing applications, the die area is expected to remain at 2.74×2.74 cm by the year 2020 (ASHRAE, 2012); therefore, the heated surface area of 1.9×1.9 cm used in this study is mildly conservative. Thermal interface materials or thermally conductive adhesives are also applied between the die and lid in order to enhance heat transfer. The current setup, which is ubiquitously used within electronics cooling literature, does not take these additional geometric layers and their corresponding thermal resistances into account.

The second dimension of importance is the vertical distance between the thermocouple slots and the heated surface. Although a distance of 0.1 in. (2.5 mm) may seem trivial, a heat load of 300 W yields a thermocouple reading that is roughly 5 °C warmer than the heated surface assuming a thermal conductivity of 400 W/m·K for copper 110. However, the fact that the temperature is always overestimated as a result of this vertical offset simply renders the setup more conservative from a design standpoint.

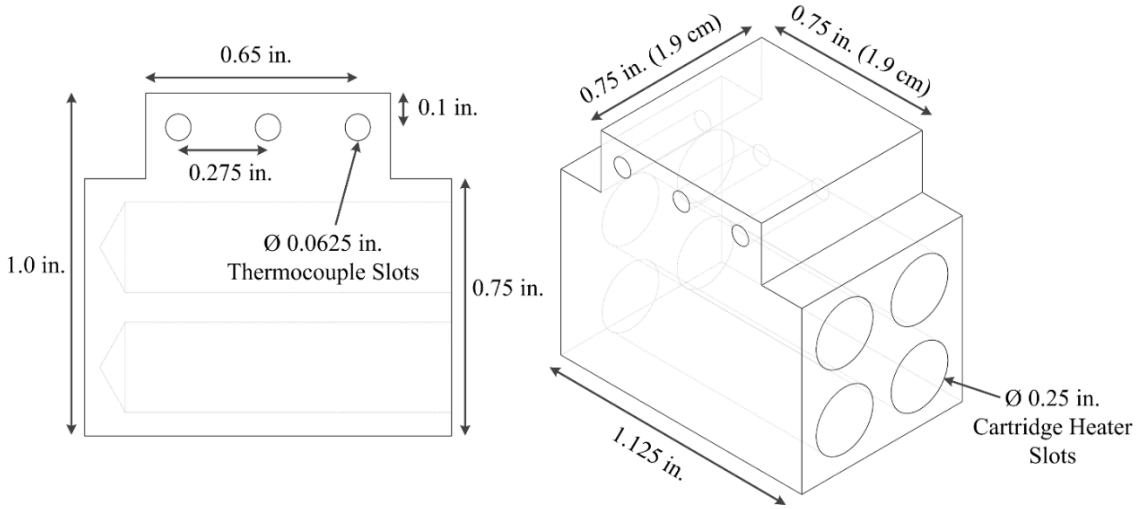

Fig. 5.10 – Schematic of copper block housing

Fig. 5.11 – Image of copper block housing

Four 100 W cartridge heaters shown in Fig. 5.12 (product code B222T11 from McMaster-Carr) with diameters of 0.25 in. (6.4 mm) and lengths of 1 in. (2.5 cm) were inserted into the slots shown in Fig. 5.10. They were powered using a variable AC power supply which allowed for experimentation at various heat loads. When measuring the voltage across and the current through the cartridge heaters, a maximum heat load of 380 W was observed at 120 V instead of the expected 400 W. This discrepancy may have been due to the non-linearity of the heater resistance with increasing temperature. Regardless of the cause, this 20 W setback had no impact on the planned experimental work as the maximum desired heat load for testing was roughly 330 W (10 % higher than the 300 W maximum heat load of HPC processors).

Fig. 5.12 – Image of cartridge heaters inserted within the copper block

Detailed diagrams of the heatsink assembly are shown in Fig. 5.13 along with an image of the heatsink base in Fig. 5.14. The heatsink consists of a copper base fastened to an aluminum cover with four stainless steel machine screws. 1060 aluminum alloy was used for the cover due to its high machinability and corrosive resistance while 110 copper alloy was used for the base due to its high thermal conductivity. Two 0.125 in. (3.2 mm) NPT holes were horizontally tapped on the opposing faces of the aluminum cover to serve as an inlet and outlet. As the hidden lines in Fig. 5.13 demonstrate, two additional holes were vertically tapped on the bottom surface of the cover; these holes intersected the horizontal ones in order to create a flow path to the heatsink manifolds.

Heatsink channels and an O-ring groove were CNC machined onto the copper heatsink base. The overall dimensions of the copper base were 3.0×3.0×0.25 in. (76×76×3.4 mm) while the total finned area was only 1.25×1.26 in. (3.2×3.2 cm). This area was made larger than the heated surface area on the copper heat source (which was 0.75×0.75 in. or 1.9×1.9 cm) in order to exploit heat spreading. The overall area of 3.0×3.0 in. (76×76 mm) was selected to be smaller than the base area of standard air cooled heatsinks used in servers (roughly 3.5×3.5 in. or 90×90 mm) (Geng, 2015). The finned area of 1.25×1.26 in. (32×32 mm) was then the largest attainable area after allocating space to the O-ring groove, the inlet/outlet manifolds, and the clearance holes. Based on the numerical work performed, both fins and channels were 0.02 in. (0.5 mm) wide and 2.3 mm tall; resulting in a total of 32 channels and 31 fins. Since the copper base was initially 0.25 in. (6.4 mm) thick and the channels were 2.3 mm tall, the thickness of the copper base beneath the channels was 4.1 mm.

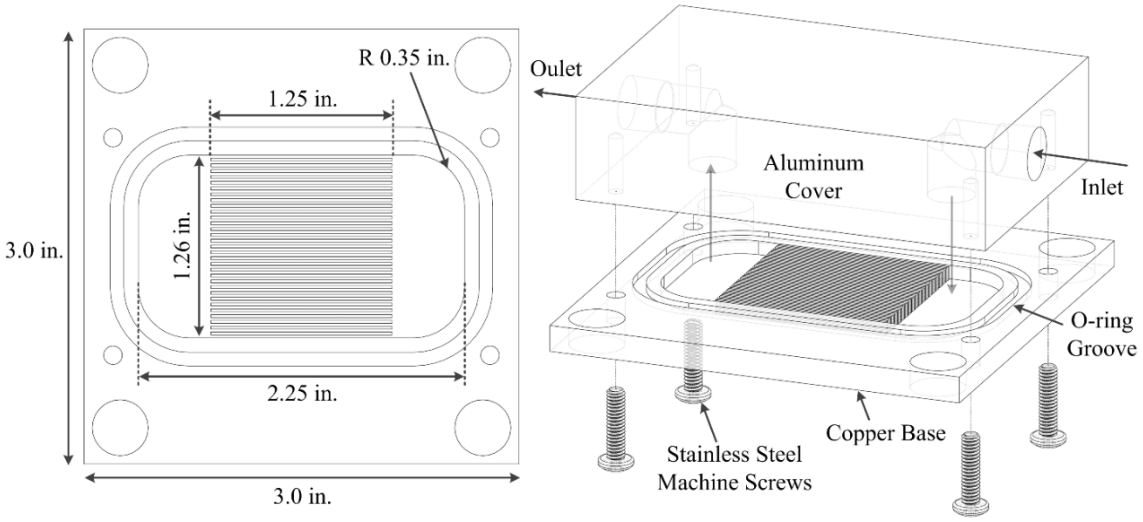

Fig. 5.13 – Schematic of the heatsink base and assembly in its exploded configuration

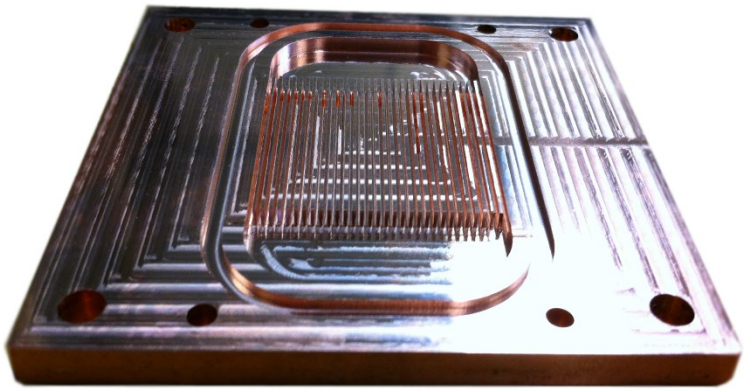

Fig. 5.14 – Image of heatsink base

5.3 Test Section 2

The second test section, shown in both collapsed and exploded configurations in Fig. 5.15, simply comprised the thermal contact heat exchanger. An image of the second test section is also shown in Fig. 5.16. The internal and external heat exchanger plates (it does not matter which is which) were fastened together using four stainless steel machine screws and nuts. This method of attachment sufficed for experimental evaluation; although, industry implementation will require more elaborate methods that permit fast and reliable detachment of the two heat exchanger plates. Thermal interface material (TGREASE 880 from Laird Technologies®) was applied between the contacting surfaces of the two heat exchanger assemblies. As with the first test section, the screws were hand tightened and

no effort was made to measure the contact pressure between the two surfaces. The surface roughness (R_a value) of the stock 110 copper alloy was measured to be 0.194 µm.

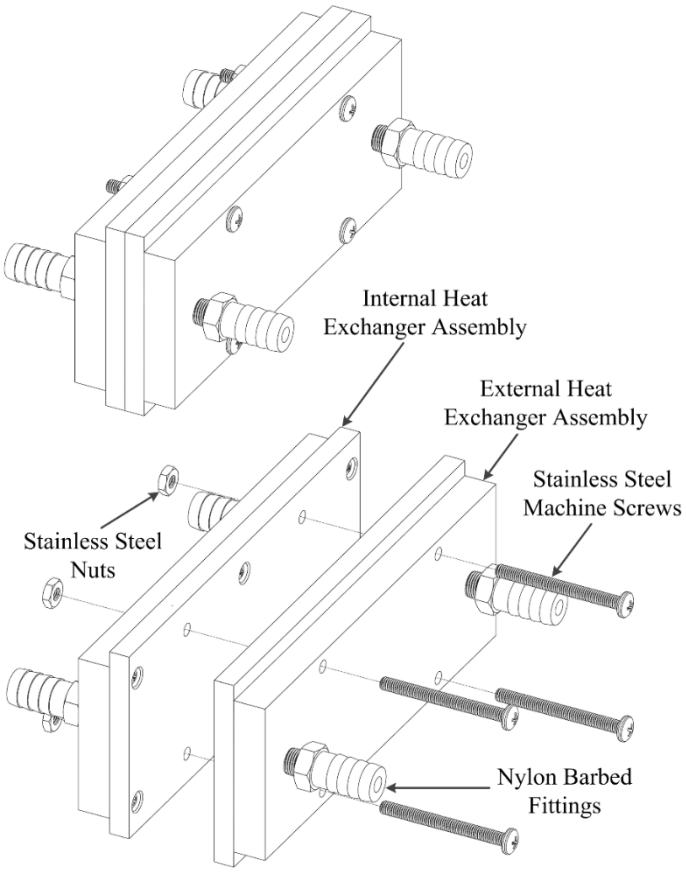

Fig. 5.15 – Schematic of a TCHx in collapsed and exploded configurations

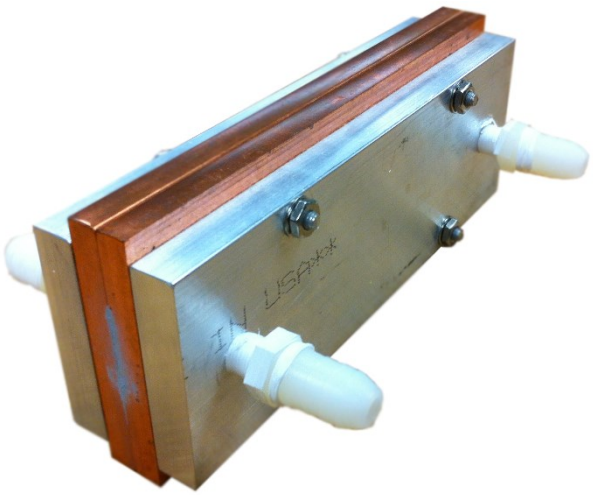

Fig. 5.16 – Image of Test Section 2

An exploded view of a single heat exchanger plate with straight channels is shown in Fig. 5.17. Images of the three heat exchanger plate designs are also shown in Fig. 5.18. It may be observed that these assemblies are identical in structure to the heatsink assembly except for dimensional differences which are accentuated for each heat exchanger design in Fig. 5.19. As briefly discussed in the earlier chapter on numerical modelling, the three heat exchanger designs tested included straight channels, a serpentine channel, and mixed straight-serpentine channels. These designs were selected for no other reason than their prevalence among cold plate manufacturers.

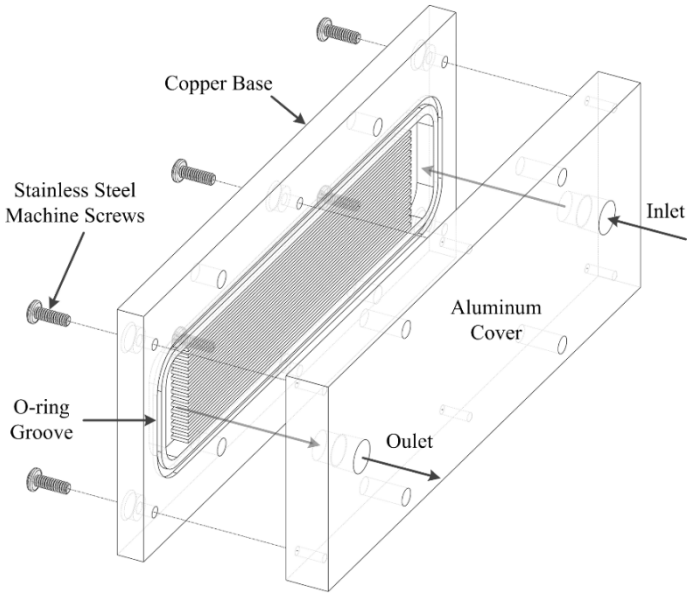

Fig. 5.17 – Schematic of a TCHx heat exchanger plate in its exploded configuration

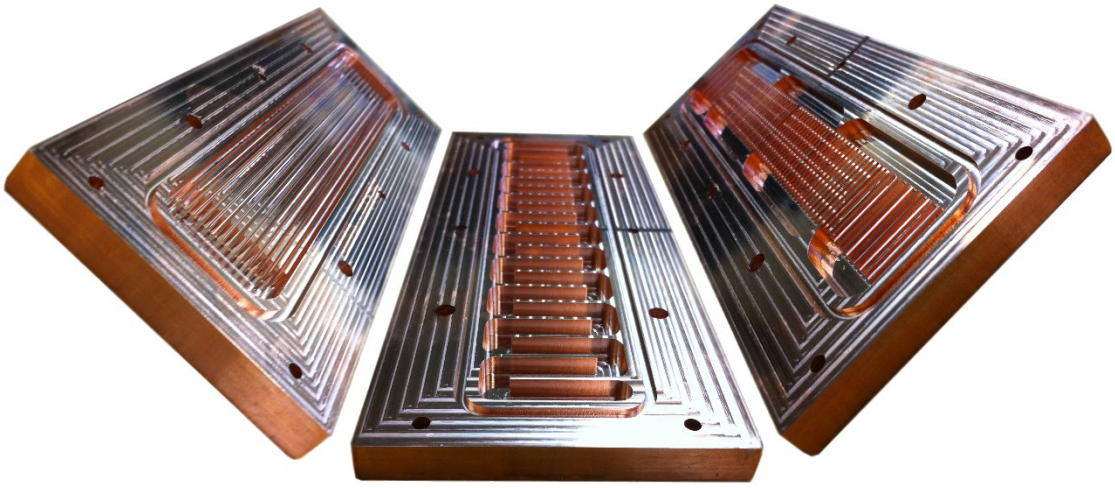

Fig. 5.18 – Images of thermal contact heat exchanger plates: straight channels (left), serpentine channel (center), and mixed channels (right)

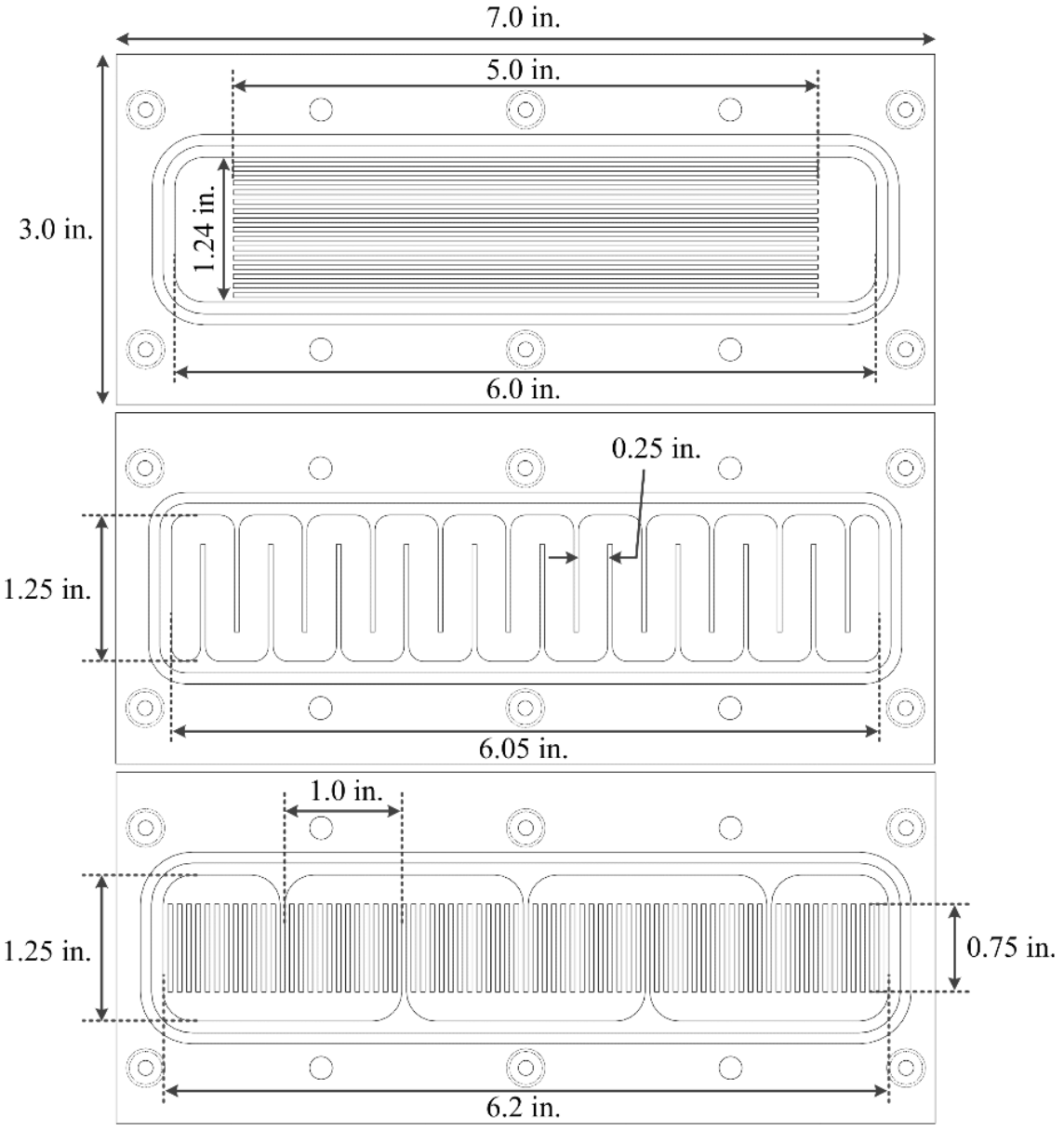

Fig. 5.19 – Schematic of the three TCHx heat exchanger designs

Starting with similarities, the overall copper base dimensions for all heat exchanger designs were 7.0×3.0×0.375 in. (178×76×9.5 mm) while the flow regions were limited to 6.0×1.25 in. (152×32 mm) in size. Some brief discussion is necessary to justify these dimensions. First, the length of 7.0 in. (178 mm) was selected based on the maximum allowable CNC workpiece size. The dimensions of a standard 1U rackmount server are typically 19×22×1.75 in. (48×56×4.5 cm); therefore, heat exchanger plates much longer than 7.0 in. (178 mm) are permissible (ASHRAE, 2012). Second, the flow region width of 1.25 in. (32 mm) was selected such that the thermal contact heat exchanger would fit

vertically within 1U rackmount servers which are 1.75 in. (4.5 cm) thick; thus leaving 0.5 in. (1.3 cm) of additional space for fastening the heat exchanger base to its cover in an industrial product. The experimental copper bases were 3.0 in. (7.62 cm) wide (which is substantially larger than the 1.75 in. limitation) simply due to the necessity of an O-ring and several clearance and tapped holes. These components would not be necessary if the industrial product made use, for instance, of bonding or solder welding for attaching the base to its cover. The flow region length of 6.0 in. (15 cm) was selected to allow space for the O-ring groove on the far sides of the base.

To sum up, the flow regions (including all channels and manifolds) in all designs were required to fit within a 6.0×1.25 in. (152×32 mm) area. It may be observed, however, that certain designs deviate slightly from this requirement. For instance, the flow region length within the mixed straight-serpentine design was actually 6.2 in. (158 mm) and the flow region width within the straight channel design was actually 1.24 in (31.5 mm). The reason for this is that an integer number of channels were required and the width of the channels and fins was predetermined. Thus the designs housed the maximum integer number of channels that fit within an area of approximately 6.0×1.25 in (152×32 mm).

Focusing on the first design, the straight channels and fins were 0.04 in. (1 mm) wide and 4 mm tall (as justified through numerical modelling). The length of the straight channels was 5.0 in. (127 mm) to allow space for the inlet and outlet manifolds. Skipping ahead to the third design, the mixed straight-serpentine pattern consisted of two separate sets of channels. The first was the larger 1 in. (25 mm) wide serpentine channel within which sat the second set of smaller 0.04 in. (1 mm) wide straight channels. The smaller straight channels and fins were of the same dimensions as the straight channels and fins within the first design in order to isolate the effect of the larger 1 in. (25 mm) wide serpentine channel. The height of the channels in the third design was also 4 mm for consistency.

Focusing now on the second design, the serpentine channel was 0.25 in. (6.4 mm) wide and 4 mm tall. The width of this channel was selected somewhat arbitrarily. Since this design consisted only of a single serpentine channel, the fluid velocity was significantly larger than in the case of a design where the flow was divided in parallel among several channels. If the serpentine channel was 1 mm wide and 4 mm tall for

instance (remaining consistent with the other designs), the fluid velocity would have been 4.2 m/s at a flowrate of 1 L/min (compared to 0.28 m/s if the flow were divided among 15 channels as in the case of the straight channel heat exchanger design). This rise in velocity alone would have been sufficient to increase the pressure drop across the heat exchanger substantially. Moreover, the pressure drop dilemma would only have been further exacerbated by the fact that this design contained a single long channel instead of several shorter channels in parallel. This increased length would then raise pressure losses across each serpentine segment.

These characteristics made it inherently difficult to maintain consistency between the serpentine channel design and the other two designs containing parallel straight channels. More simply put, a direct apples-to-apples comparison was not possible. It is for this reason that the channel width was somewhat arbitrarily selected to be 0.25 in (6.4 mm). A quick numerical simulation of two serpentine passes (with a width of 0.25 in.) yielded a predicted pressure drop of 1.2 kPa at a flowrate of 1 L/min; multiplying this value by the total number of double-passes (10.5 in total) yielded an estimated total pressure drop of 12.6 kPa. To put this into perspective, the same flow condition generated a total pressure drop of 0.2 kPa across the straight channel heat exchanger with 1 mm wide channels. Therefore, even when the serpentine channel was 0.25 in. (6.4 mm) wide, the predicted pressure drop was roughly 63 times larger than that predicted for the straight channel design with 1 mm wide channels. Reducing the channel width would only have served to further increase the pressure drop while enlarging the channel width would have adversely affected the heat transfer performance. Unfortunately, no numerical modelling was attempted in order to quantify these characteristics due to the computational expense of such a model (the unit cell approximation would not be possible for a serpentine heat exchanger).

On a final note, three heat exchanger designs have been proposed; however, no mention has yet been made concerning which combination of heat exchanger designs constitute a full thermal contact heat exchanger. Should a thermal contact heat exchanger consist of a pair of identical heat exchanger designs? For instance, should there exist only three thermal contact heat exchangers; straight channels on both sides, serpentine channel on both sides, and mixed channels on both sides? Or is it worth evaluating TCHx

assemblies with differing internal and external heat exchanger designs? The most logical choice would be the former as TCHx assemblies with differing internal and external heat exchangers would be redundant. If, for instance, the serpentine channel design yields the lowest thermal resistance, then the TCHx with the serpentine channel design on both sides would unquestionably yield the best results. Any other combination of heat exchanger designs would be inferior. The only case in which it would be worthwhile to investigate a TCHx with differing heat exchanger designs is one in which different pumping capabilities exist within the server and the facility. The internal heat exchanger plate may be limited by the capability of the miniature server pump while no such limitation may exist for the external heat exchanger in which flow is induced by the facility level pump. This detail is beyond the scope of the current study and thus the TCHx assemblies tested consist of identical pairs of heat exchanger plates.

5.4 Experimental Procedure and Repeatability

The procedure for experimentation was quite simple and requires little discussion. All operating parameters were set to the required values and the system remained active until reaching steady state. Depending on which parameters were being varied, between 15 and 30 minutes of elapsed time were necessary for the system to reach steady state. Once this state was reached, one minute of data from the temperature and pressure sensors at a frequency of one sample per second was recorded using LabVIEW. The room temperature throughout the experimental phase varied between 23 and 26 °C as several heat generating equipment were active within the author's lab.

As listed in Table 5.1, a total of five input parameters were varied during experimentation. These included the voltage across the cartridge heaters V (which determined the heat load q), the flowrates within the internal and external loops Q_{int} and Q_{ext}, the inlet temperature to the external heat exchanger plate $T_{in,ext}$, and the thermal contact heat exchanger type. Of course, not all possible combinations of parameters were tested (this would require more than 2,000 tests). The specific combinations tested will be reviewed when discussing the results.

Table 5.1 – List of operating parameters used during experimentation

Voltage, V (V)	Heat load, q (W)	Flowrates, Q_{int} & Q_{ext}	System inlet Temperature, $T_{in,ext}$ (°C)	TCHx Channel Type
45	54.4	0.3 – 1.5 gal/min	20	Straight
65	111.8	1.14 – 5.68 L/min	30	Serpentine
80	169.2		40	Mixed
92	223.6		50	
102	273.7		60	
112	330.4			

5.4.1 Voltage Across Cartridge Heaters

It was initially desired to test heat loads of 50, 100, 150, 200, 250, and 300 W. However, in order to account for potential heat losses and to evaluate the system more conservatively, these heat loads were increased by roughly 10 % to yield the values listed in Table 5.1. The listed voltages simply represent the variable AC power supply voltages necessary to produce these desired heat loads (the relationship between voltage and heat load will be further detailed when discussing data reduction).

5.4.2 Internal and External Flowrates

The widest range of flowrates tested was 0.3 to 1.5 gal/min (1.14 to 5.68 L/min); however, this range only applied to the straight channel TCHx. The large pressure losses across the other two designs limited their maximum flowrates to 0.4 gal/min (1.5 L/min) for the serpentine design and 0.8 gal/min (3.0 L/min) for the mixed design. The term maximum used in the previous sentence must be clarified. Since the differential pressure sensors used were rated up to 5 psi (34.5 kPa), the maximum allowable pressure drop across any component was limited to 30 kPa during experimentation. Furthermore, miniature 12 or 24 V centrifugal pumps that would fit within a rackmount server deliver a maximum head capacity between 30 to 78 kPa. This range is based on the performance of a miniature solar pump (model TL-B10-B) produced by TOPSFLO. A maximum allowable pressure of 30 kPa was selected while conservatively siding with the lower end of this range. As a result, the maximum allowable flowrate was defined as the flowrate which generated less than roughly 30 kPa of pressure drop across any given component.

5.4.3 System Inlet Temperature

The most important parameter was unequivocally the inlet temperature to the external component of the TCHx $T_{in,ext}$. For all intents and purposes, this parameter may well be called the inlet temperature to the overall system because it is the only temperature that was directly controlled. All other temperatures (within the fluid and the copper heat source) were generated in response to the input parameters listed in Table 5.1; whereas $T_{in,ext}$ was specified and directly controlled by the recirculation chiller. The reason why $T_{in,ext}$ was the most important operating condition was alluded to in the introduction. The main objective of this study was to design a cooling system which maximized the coolant temperature and thereby minimized the cost of cooling. The inlet temperature to the system $T_{in,ext}$ is essentially the coolant temperature that must be maximized. The range of system inlet temperatures tested was 20 to 60 °C and the desired outcome of the study, to reiterate, was to dissipate a 300 W heat load using the higher end of this range while maintaining the heated surface temperature below 85 °C. The inlet temperature did not exceed 60 °C due to the thermal limitations of various components and instruments.

Throughout this study the term system inlet temperature $T_{in,ext}$ refers to the temperature setting on the recirculation chillers. Due to heat losses through the tubing, the actual system inlet temperature may have been slightly lower than this setting. At the highest temperature setting of 60 °C and the lowest flowrate of 0.3 gal/min (1.1 L/min) – a combination which should yield the highest heat losses – the actual system inlet temperature was 58.8 °C. At a flowrate of 1 gal/min (3.8 L/min), the actual system inlet temperature was 59.6 °C. Additionally, the system inlet temperature may have further fluctuated with varying ambient temperatures. This fluctuation is no cause for concern as the actual inlet temperature was used when calculating crucial parameters such as thermal resistances or heat transfer rates.

5.4.4 Type of TCHx Assembly

Finally, the three TCHx assemblies tested included straight channels on both sides, serpentine channel on both sides, and mixed channels on both sides (these combinations were justified in the previous chapter). Referring back to the introduction, one of the purposes of experimentation was to compare the performance of the proposed system to that of a conventional water cooling system which uses fluidic connectors. This objective

does not necessarily require two separate configurations of the experimental setup; one with the TCHx acting as an intermediary heat transfer medium and one in which water flows directly from the recirculating chiller to the heatsink. Since temperature measurements were being made across the heatsink as well as the TCHx, there was an opportunity to (for the lack of more scientific terminology) kill two birds with one stone. This approach is best explained through an example.

Assume the following operating parameters: a 300 W heat load q, internal and external flowrates Q_{int} and Q_{ext} of 1.0 gal/min (3.8 L/min), and a system inlet temperature $T_{in,ext}$ equal to 50 °C. In response to these conditions, the heated surface temperature T_w may be 85 °C and the inlet temperature to the heatsink $T_{in,hs}$ may be 60 °C. In other words, in order to maintain the heated surface temperature at 85 °C with the given heat load and flowrates, the inlet temperature to the external TCHx plate must be 50 °C and the inlet temperature to the heatsink must be 60 °C. The argument may then be made that the inlet temperature to the heatsink is in fact the inlet temperature for a conventional water cooling system; this relation is true simply because the conventional system consists of a heatsink and nothing else. Therefore, for the same set of operating conditions, the conventional water cooling system would be operating with an inlet temperature that is 10 °C higher than the inlet temperature of the proposed cooling system; and would thus require lower cooling costs. One major aim of this study is then to quantify the difference in the cooling costs and to establish whether the higher cost of the proposed system represents a fair trade-off for its added reliability (which derives from the elimination of leakage risks by removing fluidic connectors).

5.5 Repeatability

The parameters that may have affected the repeatability of the experiments include the room temperature, the heat generated by the pump, residue buildup or blockage within the heatsink, and the assembly of Test Section 1 (*i.e.* the contact pressure between the heated surface and the heatsink base). In order to test for repeatability, three experimental runs were performed for which the maximum wall temperatures are plotted in Fig. 5.20. The maximum wall temperature was used for evaluating repeatability as it was the quantity of primary interest; the ultimate purpose of these experiments was to identify whether the maximum wall temperature remained below 85 °C for a given set of operating conditions.

Run 1 was conducted immediately after Test Section 1 was assembled for the first time. Run 2 was conducted at the end of the second day of experimentation when the system had been active for nearly eight hours. Test Section 1 was not reassembled for the second run. Run 3 was conducted after two weeks of experimentation with Test Section 1 completely disassembled, cleansed, and reassembled. The operating conditions were held fixed for these tests and are described in the figure caption.

There is little to gather from this plot other than the fact that the disparity in wall temperatures between the three runs grows as the heat load increases. This outcome should be expected. As the heat load increases, the effect of any parameter that influences the wall temperature should become more pronounced. This scenario is analogous to multiplying two slightly different signals by a gain and observing a growing absolute difference between them. At a heat load q of 50 W, the maximum difference among the three runs was 0.3 °C (between Run 1 and Run 2 to be specific). At a heat load q of 269 W, this maximum difference was 1.6 °C (between Run 2 and Run 3). Judging whether this temperature difference is acceptable in terms repeatability requires further analysis.

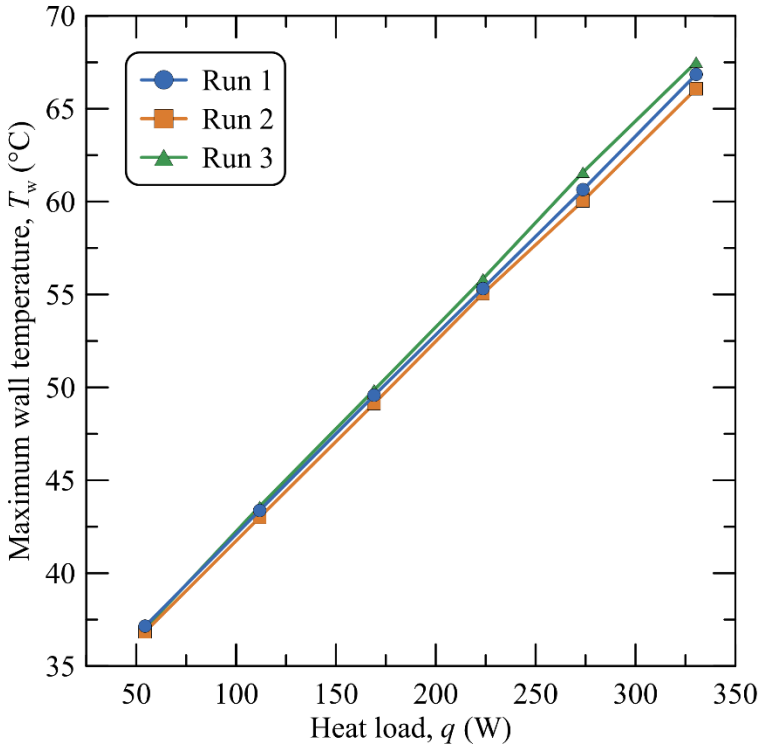

Fig. 5.20 – Wall temperature repeatability, $T_{in,ext}$ = 30 °C, Q_{int} = 1.0 gal/min, Q_{ext} = 1.0 gal/min, straight channel TCHx

For any given heat load q, the relative repeatability error was calculated as follows:

$$\delta_{\text{rep}} = \frac{\max(T_{\text{w}}) - \min(T_{\text{w}})}{\min(T_{\text{w}}) - T_{\text{in,ext}}} \times 100 \tag{5.1}$$

where $\max(T_{\text{w}})$ and $\min(T_{\text{w}})$ represent the highest and lowest wall temperatures from the three runs at any given heat load q. At a heat load q of 325 W for instance, the highest wall temperature belonged to Run 3 while the lowest belonged to Run 2. The numerator within this equation therefore simply calculates the maximum possible difference among the three runs. The term $\min(T_{\text{w}})$ was used in the denominator instead of an average wall temperature in order to most conservatively calculate the relative difference.

The resulting maximum relative difference at the various heat loads is shown in Fig. 5.21. Even though the maximum absolute differences shown in Fig. 5.20 increased as the heat load rose, the maximum relative difference hovered between 3 and 5 % at all heat loads. Therefore, based on the three repeatability tests, it is safe to conclude that experiments were subject to at most a 5 % repeatability error on the maximum wall temperature.

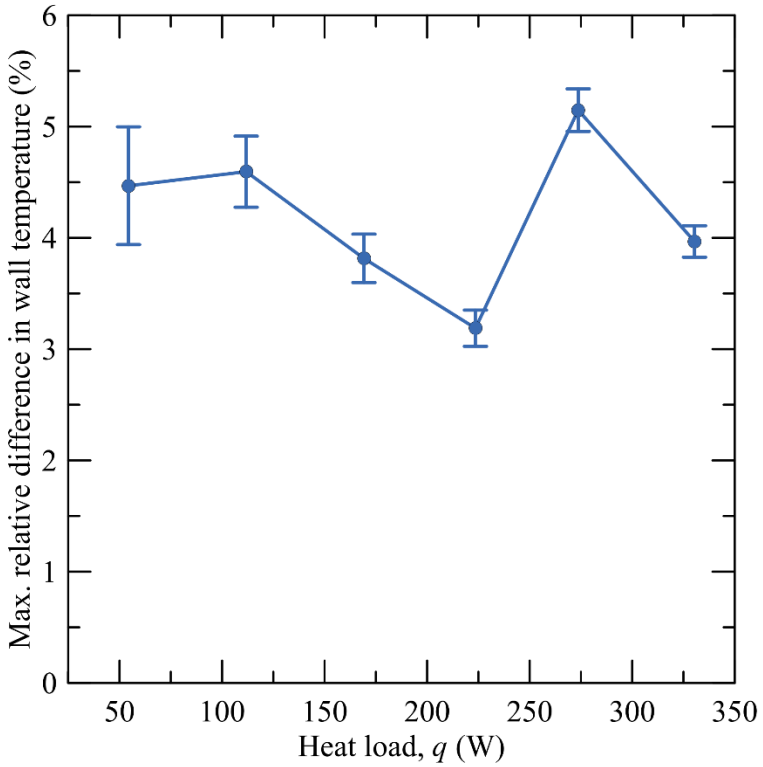

Fig. 5.21 – Relative wall temperature repeatability, $T_{\text{in,ext}}$ = 30 °C, Q_{int} = 1.0 gal/min, Q_{ext} = 1.0 gal/min, straight channel TCHx

Chapter 6 - Data Reduction and Uncertainty Analysis

This chapter defines the equations and methods used to calculate the various properties and operating conditions that characterize the proposed cooling system. Subsequently, the uncertainties associated with these parameters are discussed.

6.1 Data Reduction

6.1.1 Heat Load

In this study, the term heat load refers to the total rate of heat generated by the four cartridge heaters. Due to heat losses to the ambient air, not all heat generated by the heaters was transferred to the fluid. This section outlines the methods used to calculate the heat load, the rate of heat transferred to the fluid, and the resulting heat losses.

After measuring the current through and the voltage across the cartridge heaters I and V, the rate of heat generated by the heaters q is calculated as follows:

$$q = IV \tag{6.1}$$

This calculation represents the rate of heat generated by all four cartridge heaters; however, it does not take into account heat losses q_{loss}. The rate of heat transfer to the fluid q_{in} was first calculated through a first law analysis across the heatsink:

$$q_{\text{in}} = \dot{m}_{\text{int}} c_{\text{p}} \left(T_{\text{out,hs}} - T_{\text{in,hs}}\right) = \rho Q_{\text{int}} c_{\text{p}} \left(T_{\text{out,hs}} - T_{\text{in,hs}}\right) \tag{6.2}$$

where Q_{int} is the flowrate within the internal flow loop which contains the heatsink, c_{p} is the specific heat capacity at constant pressure of water, ρ is the density of water, and the two temperature variables represent the heatsink inlet and outlet fluid temperatures. The specific heat capacity c_{p} was taken to be 4,180 J/kg·K as the property varies by less than 0.27 % between water temperatures of 20 and 70 °C (which was the expected range throughout experimentation). The density ρ was calculated as a function of fluid temperature through the following polynomial regression:

$$\rho = -0.0039T^2 - 0.0585T + 1000.9 \tag{6.3}$$

The coefficients in this equation were determined based on water density values for various temperatures at atmospheric pressure (Sonntag et al., 2003). When calculating the heat transfer rate to the fluid, the water density was calculated based on the fluid temperature at

the heatsink inlet. With the heat load q and the heat transfer rate to the fluid q_{in} calculated, heat losses q_{loss} were calculated as follows:

$$q_{loss} = q - q_{in} \tag{6.4}$$

A comparison between the heat load q and the rate of heat transferred to the fluid q_{in} is shown in Fig. 6.1. As expected, the heat transferred to the fluid is always less than the heat load at all heater voltages. Moreover, the first test section was well enough insulated that the disparity between the two curves is observably insignificant. A quantitative assessment of heat losses is necessary regardless.

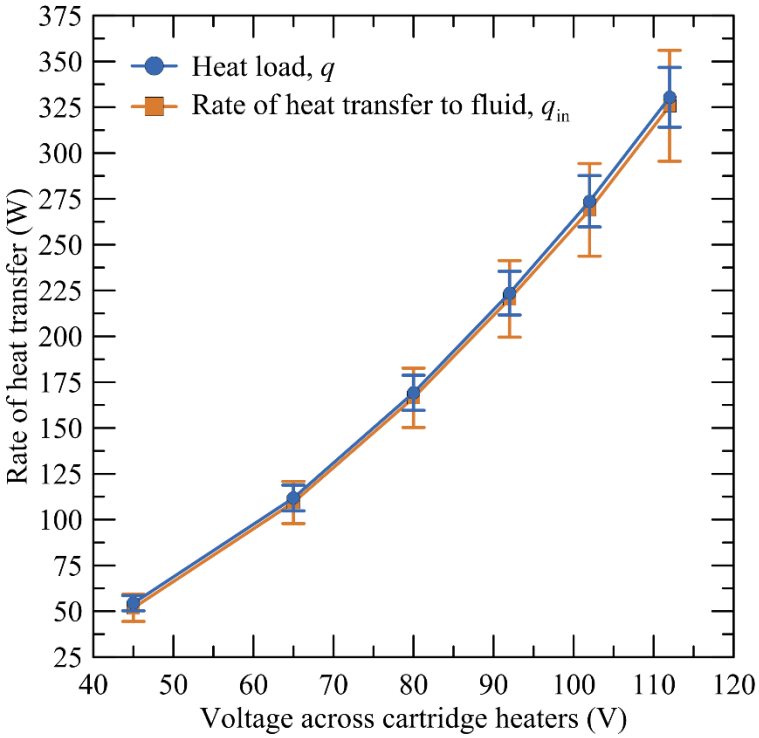

Fig. 6.1 – Comparison of heat load to the rate of heat transfer to the fluid, $T_{in,ext}$ = 30 °C, Q_{int} = 1.0 gal/min, Q_{ext} = 1.0 gal/min, straight channel TCHx

The heat loss as a percentage of the heat load is plotted in Fig. 6.2. Prior to examining its content, it should be noted that uncertainties in this plot are as high as 15 % due to the large uncertainty in calculating the heat transfer rate to the fluid q_{in}. Subsequent discussions on uncertainty will address this point further. The current discussion is focused upon the general trend of the results. It should be noted from the figure, that uncertainties generally decline as the heat load increases. The reason for this decline is that an increase in the heat load raises the temperature difference across the heatsink which in turn reduces the relative error in relative temperature measurements. A useful conclusion is therefore

that the calculation of the heat transfer rate to the fluid q_{in} is more accurate at higher heat loads. In other words, the percent heat loss calculated at a heat load of 330.4 W makes redundant the percent heat losses calculated at any lower heat loads.

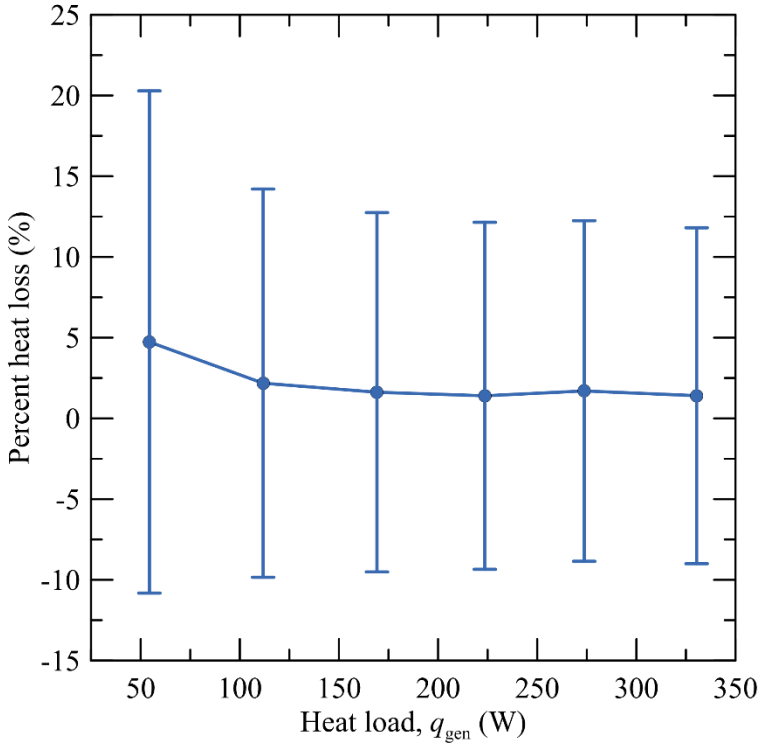

Fig. 6.2 – Heat losses as a percentage of heat load, $T_{in,ext}$ = 30 °C, Q_{int} = 1.0 gal/min, Q_{ext} = 1.0 gal/min, straight channel TCHx

Returning to the figure content, it was established that at the lowest heat load q of 54.4 W, heat losses were calculated to be 4.73 % of the total heat load (and up to 20 % when considering uncertainties). At a heat load of 330.4 W, heat losses were calculated to be 1.4 % of the total heat load (up to 12 % when considering uncertainties). It does not make physical sense that percent heat losses at lower heat loads should exceed those at higher heat loads. At lower heat loads, the temperature of all surfaces should be closer to the ambient air temperature; thus reducing heat losses to the ambient air rather than increasing them. The reason for the observed higher percent heat loss at a lower heat load of 54.4 W is, as already mentioned, measurement errors in the temperature rise across the heatsink.

For now, it may be conservatively assumed that at least 88 % of all heat generated was transferred to the fluid. This number stems from the fact that at a heat load q of 330.4 W, the percent heat loss was calculated to be as high as 12 % with uncertainties considered.

Furthermore, this was the most accurately calculated percent heat loss value and it therefore trumps the 20 % heat loss calculated at a lower heat load of 54.4 W. As a result, the heat load q was used in all subsequent analyses and discussions to identify the heat transfer rate of the system. Whenever the text reads 330.4 W for instance, the reader should consider that at most 12 % of the heat generated may have been lost to the ambient air. The reason that the heat load q was preferable to the actual rate of heat transfer to the fluid q_{in} is that heat load uncertainty was less volatile. The uncertainty in the rate of heat transfer to the fluid would vary significantly depending on the heat load, the flowrate, and the temperature rise across the heatsink. This point will be further addressed when discussing uncertainties.

6.1.2 Maximum Wall Temperature

As previously mentioned, the desired outcome of any cooling system is to maintain the maximum processor die temperature below the typical allowable limit of 85 °C. As a result, one of the main quantities of interest within this study was the maximum temperature of the heated copper surface; also termed the maximum wall temperature T_w. As previously demonstrated in Fig. 5.10, three thermocouples were inserted within the copper heat source block a distance of 0.1 in. (2.5 mm) below the top surface. One of the intentions behind this arrangement was to characterize the temperature distribution along the heated surface in the direction of the flow. More importantly, the intent was to calculate through extrapolation the temperature at the downstream edge of the heated surface. This edge would theoretically represent the hottest location along the heated surface as the coolant temperature within the heatsink would be highest the furthest downstream.

The temperature of this edge was calculated using a linear regression of the three thermocouple measurements. For an exemplary set of operating conditions, the temperature distribution along the heated surface is shown in Fig. 6.3. The highest thermocouple measurement, which was taken at a distance of 0.65 in. (16.5 mm) from the upstream edge of the heated surface, was 66.9 °C. The maximum heated surface temperature, which was located at the downstream edge and was calculated using a linear regression, was 67.5 °C. The relative difference between these quantities (calculated relative to an inlet temperature of 30 °C) was 1.6 %. Given such minute disparity even at the highest heat load of 330.4 W, it was deemed sufficient to quantify the maximum wall temperature T_w through the most downstream thermocouple measurement rather than

through the extrapolated maximum value. This is especially a reasonable approximation when considering the fact that the thermocouple measurements overestimate the wall temperature by 5 °C at a 300 W heat load due to the 0.1 in. (2.5 mm) vertical offset from the heated surface (this point was previously addressed when describing copper block housing).

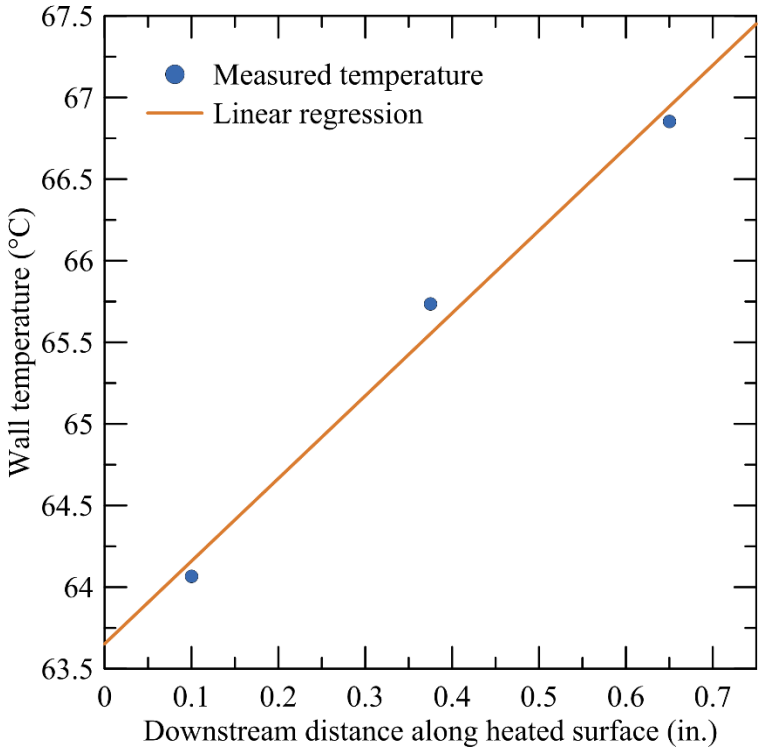

Fig. 6.3 – Temperature distribution along heated surface, q = 330.4 W, $T_{in,ext}$ = 30 °C, Q_{int} = 1.0 gal/min, Q_{ext} = 1.0 gal/min, straight channel TCHx

6.1.3 Thermal Resistance

The thermal resistances of the heatsink and different TCHx assemblies were calculated for various reasons. In all cases, the thermal resistance provided a single parameter with which a subsystem's performance could be estimated for any given set of operating conditions. In the case of the TCHx assemblies, the thermal resistance enabled a direct comparison between the various designs using a single parameter.

The thermal resistance of the heatsink R_{hs} was calculated based on the difference between the maximum wall temperature T_w and the heatsink inlet temperature $T_{in,hs}$ as follows:

$$R_{hs} = \frac{T_w - T_{in,hs}}{q_{in}} \tag{6.5}$$

The heatsink inlet temperature $T_{\text{in,hs}}$ was used instead of an average fluid temperature such that the thermal resistance would serve as a predictive parameter. For a given heat and a desired maximum wall temperature, the thermal resistance as defined above may be used to estimate the requisite inlet water temperature. It should be noted that the heat transfer rate to the fluid q_{in} was used when calculating the thermal resistance of the heatsink.

The thermal resistance of the TCHx assemblies R_{TCHx} was calculated based on the difference between the inlet temperatures of the internal and external heat exchanger plates as follows:

$$R_{\text{TCHx}} = \frac{T_{\text{in,int}} - T_{\text{in,ext}}}{q_{\text{out}}} \tag{6.6}$$

where $T_{\text{in,int}}$ and $T_{\text{in,ext}}$ are the inlet temperatures to the internal and external heat exchanger plates respectively. This equation essentially describes the difference in inlet temperatures necessary to dissipate a certain heat load q_{out} from the system. The newly introduced term q_{out} represents the rate of heat transfer out of the internal flow loop through the internal TCHx plate. It is calculated based upon the difference between the inlet and out temperatures of the internal TCHx plate $T_{\text{in,int}}$ and $T_{\text{out,int}}$ as follows:

$$q_{\text{out}} = \rho Q_{\text{int}} c_{\text{p}} \left(T_{\text{in,int}} - T_{\text{out,int}} \right) \tag{6.7}$$

The thermal resistance of the entire cooling system R_{sys} could have been calculated based on the difference between the maximum wall temperature T_{w} and the system inlet temperature $T_{\text{in,ext}}$ as follows:

$$R_{\text{sys}} = \frac{T_{\text{w}} - T_{\text{in,ext}}}{q} \tag{6.8}$$

However, this method is flawed for a reason that has yet to be discussed: the centrifugal pump within the internal flow loop generated heat at a nontrivial rate. A more detailed discussion of pump heating is provided in subsequent sections. At the current stage, the reader simply needs to appreciate why the system thermal resistance R_{sys} cannot be calculated as shown in Eq. (6.8). Although it may yield a fair approximation, the above equation does not take into account the additional rate of heat input into the system. The solution to this problem is not as trivial as simply adding the pump heat load to the actual heat load because the pump heats the fluid upstream of the heat source rather than at the heat source itself.

Instead, an equivalent thermal resistance was calculated for the entire system based upon the thermal resistances of the heatsink and TCHx. The derivation is interesting and begins with defining the system heat transfer rate as a function of the heatsink thermal resistance as follows:

$$q = \frac{T_{\mathrm{w}} - T_{\mathrm{in,hs}}}{R_{\mathrm{hs}}} \tag{6.9}$$

Since the fluid leaving the heatsink directly enters the internal TCHx plate, the heatsink outlet temperature $T_{\mathrm{out,hs}}$ must be equal to the inlet temperature of the internal heat exchanger plate $T_{\mathrm{in,int}}$. Furthermore, the heatsink outlet temperature may be defined through a first law analysis of the heatsink. Both statements may be expressed as follows:

$$T_{\mathrm{in,int}} = T_{\mathrm{out,hs}} = T_{\mathrm{in,hs}} + \frac{q}{\rho Q_{\mathrm{int}} c_{\mathrm{p}}} \tag{6.10}$$

where ρ is the density of water, Q_{int} is the volumetric flowrate within the internal loop, and c_{p} is the specific heat capacity at constant pressure of water. Solving Eq. (6.10) for $T_{\mathrm{in,hs}}$ and substituting into Eq. (6.9) yields the following:

$$q = \frac{1}{R_{\mathrm{hs}}}\left[T_{\mathrm{w}} - \left(T_{\mathrm{in,int}} - \frac{q}{\rho Q_{\mathrm{int}} c_{\mathrm{p}}}\right)\right] \tag{6.11}$$

The next step is to eliminate $T_{\mathrm{in,int}}$ and replace it with the system inlet temperature $T_{\mathrm{in,ext}}$. This step is accomplished by rearranging Eq. (6.6) into the following form:

$$T_{\mathrm{in,int}} = T_{\mathrm{in,ext}} + qR_{\mathrm{TCHx}} \tag{6.12}$$

Substituting Eq. (6.12) into Eq. (6.11) yields the following:

$$q = \frac{1}{R_{\mathrm{hs}}}\left[T_{\mathrm{w}} - \left(T_{\mathrm{in,ext}} + qR_{\mathrm{TCHx}} - \frac{q}{\rho Q_{\mathrm{int}} c_{\mathrm{p}}}\right)\right] \tag{6.13}$$

Finally, isolating q yields an equation relating the heat load to the difference between the maximum wall temperature T_{w} and the system inlet temperature $T_{\mathrm{in,ext}}$ as follows:

$$q = \frac{T_{\mathrm{w}} - T_{\mathrm{in,ext}}}{R_{\mathrm{hs}} + R_{\mathrm{TCHx}} - \frac{1}{\rho Q_{\mathrm{int}} c_{\mathrm{p}}}} \tag{6.14}$$

where the entire denominator represents the equivalent thermal resistance of the cooling system R_{sys} as follows:

$$R_{\mathrm{sys}} = R_{\mathrm{hs}} + R_{\mathrm{TCHx}} - \frac{1}{\rho Q_{\mathrm{int}} c_{\mathrm{p}}} \tag{6.15}$$

This equation yields the advantage of directly estimating the system inlet temperature $T_{\mathrm{in,ext}}$ required to maintain the heated surface at a desired maximum temperature T_{w} for any given heat load q. The fact that the system thermal resistance is a function of the thermal

resistances of the heatsink and TCHx is unsurprising. If the thermal resistances of either component were to increase, so too would the thermal resistance of the overall system. The third and final term in the equation is certainly more interesting and accounts for the temperature rise across the heatsink. In contrast to the intuition of a thermal engineer, the presence of the third term indicates that larger coolant densities, flowrates, and specific heat capacities actually serve to increase the overall system thermal resistance. This finding is counterintuitive because larger values of these parameters are usually preferred for reducing thermal resistances and enhancing heat transfer. For instance, water is a superior coolant relative to air due to its enhanced density and specific heat capacity. Nonetheless, a simple thought experiment will validate the above equation.

If the wall temperature T_w and the system inlet temperature $T_{in,ext}$ were held fixed, then the system thermal resistance alone would determine the rate at which heat transfers from the heat source to the external flow loop. Assuming that the thermal resistance of the heatsink and TCHx remain unchanged, reducing the specific heat capacity of the fluid would increase the temperature rise across the heat sink. This temperature rise would in turn result in a higher temperature fluid being delivered to the thermal contact heat exchanger. Since the thermal resistance of the TCHx was held fixed in this hypothetical case, heat would transfer across the TCHx at a higher rate due simply to the larger temperature difference between the internal and external heat exchanger plates. Specific heat capacity was used to illustrate this point; coolant density and flowrate would have served the purpose equally well. In reality, reducing the specific heat capacity, density, or flowrate of the coolant would absolutely diminish the thermal resistances of both the heatsink and the TCHx plates. This hypothetical and idealized example simply allowed for the effects of a specific term to be isolated.

6.1.4 Pumping Power

The pumping power required to maintain a given flowrate is useful as it serves as an indication of the total operating cost of the cooling system. More importantly, it provides an additional basis upon which to compare the various TCHx designs. If two designs hypothetically yielded identical thermal performances, then the design requiring the lower pumping power would be the more attractive choice (unless this design also yielded

massive pressure losses). The required pumping power across any given component was calculated as follows:

$$\dot{W}_{\text{pump}} = Q\Delta P \tag{6.16}$$

where Q is the flowrate through any given component and ΔP is the pressure drop across said component. Pumping power is denoted as the first order time derivative of the pump work W_{pump}.

The total pumping power required by the internal flow loop would then be the sum of the individual pumping power requirements of each of its components. For an industrial product, these would include the heatsink, the internal TCHx plate, and all tubing. For the current experimental, these additionally include the needle valve, the flowmeter, and all fittings.

6.1.5 Pump Heat Load

As mentioned while discussing thermal resistance calculations, the centrifugal pump within the internal flow loop generated heat at a nontrivial rate. This pump heat load q_{pump} was calculated based on a first law analysis across the pump as follows:

$$q_{\text{pump}} = \rho Q_{\text{int}} c_{\text{p}} \left(T_{\text{in,hs}} - T_{\text{out,int}}\right) \tag{6.17}$$

where ρ and c_{p} are the density and specific heat capacity of the fluid and Q_{int} is the internal volumetric flowrate. The heat load was calculated based on the temperature difference between the heatsink inlet $T_{\text{in,hs}}$ and the internal TCHx plate outlet $T_{\text{out,int}}$. The reason that these temperature we used is that, upon leaving the internal TCHx plate, the fluid passes through the pump and then enters the heatsink. Therefore, any heat gained from the centrifugal pump would alter the fluid temperature between these points.

The rate of heat transfer from the pump to the fluid is plotted as a function of the system inlet temperature $T_{\text{in,ext}}$ in Fig. 6.4. Interestingly, the pump heat load decreased almost linearly as the system inlet temperature increased. This relationship indicates that the pump cannot be treated as a constant heat generating device; but rather, it must be treated as a constant temperature source of heat. Rather, the rate of heat transfer to the fluid is determined based upon the temperature of the pump housing. At lower fluid temperatures, the temperature difference between the fluid and the pump housing is greater and thus induces a larger rate of heat transfer to the fluid. This conclusion is reinforced by the fact that at the highest system inlet temperature of 60 ºC, heat was actually transferred

from the fluid to the pump. This reverse direction of heat transfer indicates that the fluid temperature may have been exceed the pump housing temperature.

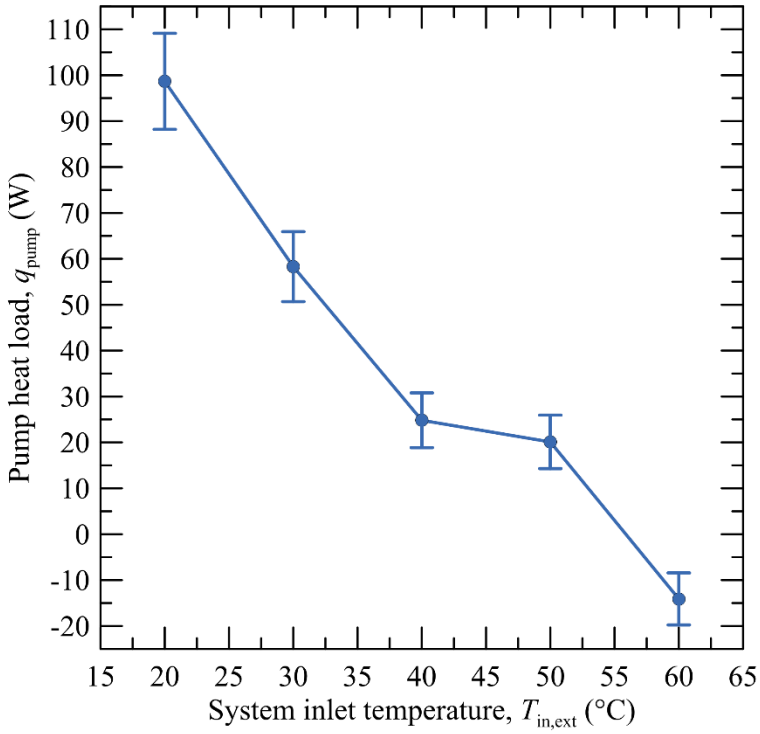

Fig. 6.4 – Heat transferred to or from centrifugal pump, q = 330.4 W, Q_{int} = 1 gal/min, Q_{ext} = 1 gal/min, straight channel TCHx

Overall, the rate of heat transfer from the pump to the fluid ranged from -15 to 100 W depending on the system inlet temperature. A 100 W pump heat load seems quite significant; however, when considering the nature of the heat transfer, such a high heat load is not worrisome. The primary value of interest in this study is the heated surface temperature T_w. If, hypothetically speaking, the additional 100 W pump heat load was being transferred to the fluid at the heat source rather that at the pump, then a 300 W system would actually be generating heat at a rate of 400 W. This configuration would raise the heated surface temperature by at least 10 ºC (this value was calculated by assuming the absolute lowest thermal resistances measure from experimentation).

In reality, the additional 100 W heat load is transferred to the fluid at the pump which lies upstream of the heat source. As a result, the 100 W heat load solely raises the fluid temperature by 1.3 ºC assuming a low flowrate of 0.3 gal/min (1.1 L/min) and 0.38 ºC assuming a nominal flowrate of 1.0 gal/min (3.8 L/min). This rise in the fluid temperature ultimately yields an equal rise in the heated surface temperature. A maximum possible

wall temperature rise of 1.3 ºC is acceptable given that the difference between the heated surface temperature and the system inlet temperature was as high as 30 ºC at heat loads of interest. Ultimately, the heat transferred from the pump to the fluid is dissipated from the system through the thermal contact heat exchanger.

On a side note, the linearity of the pump heat load in Fig. 6.4 is temporary broken between system inlet temperatures of 40 and 50 ºC. The reason for this break is discontinuity in experimentation between these runs. The data points for system inlet temperatures of 20, 30, and 40 ºC were all collected on the same day. The data points for system inlet temperatures of 50 and 60 ºC were collected on the next day. This conclusion indicates that the pump heat load was not repeatable; however, this irreparability is no cause for concern as the maximum wall temperature, which is the primary value of interest, was subject to a repeatability error of 5 %.

Table 6.1 – Measurement and parameter uncertainties

Measurement	Error Expression	Error	At Value
Absolute temperature, T	± 0.3 °C	-	-
Relative temperature, ΔT	± 0.03 °C	-	-
Pressure drop, ΔP	± 1.7 %	± 0.51 kPa	30 kPa
Flowrate, Q	± 4 % + 0.05 gal/min	± 0.09 gal/min	1.0 gal/min
	± 4 % + 0.19 L/min	± 0.34 L/min	3.8 L/min
Pumping power, $\dot{W}_{pump}$	-	± 0.086 W	± 0.95 W
Cartridge heater current, I	± 3 % + 0.05 A	± 0.14 A	2.95 A
Cartridge heater voltage, V	± 0.8 % + 0.8 V	± 1.7 V	112 V
Heat load, $q = IV$	-	± 16.5 W	330.4 W
Water density, ρ at 70 °C	-	± 0.18 kg/m^3	978 kg/m^3
Water specific heat capacity, c_p	-	± 11.4 J/kg·K	4,180 J/kg·K
Heat transfer to fluid, $q_{in} = \rho Q_{int} c_p \Delta T$	-	± 30.8 W	330.4 W
Heatsink thermal resistance, R_{hs}	-	± 0.0077 K/W	± 0.084 K/W
TCHx thermal resistance, R_{TCHx}	-	± 0.0024 K/W	± 0.026 K/W
System thermal resistance, R_{sys}	-	± 0.0081 K/W	± 0.11 K/W

6.2 Uncertainty Analysis

The uncertainties associated with the various measurements and calculated parameters are listed in Table 6.1. This table lists the general uncertainty expression for

each measurement as well as the uncertainty at practical values of each measurement. If the value of a listed quantity depends on another listed quantity with variable uncertainties, then the listed values and uncertainties of the independent quantity are used. For instance, the heat transfer rate to the fluid q_{in} depends upon the internal flowrate Q_{int} for which the uncertainty varies with magnitude. Therefore, the listed value and uncertainty of q_{in} (330.4 ± 30.8 W) are based upon the listed value and uncertainty of Q_{int} (1.0 ± 0.09 gal/min or 3.8 ± 0.34 L/min). The following subsections provide justifications for each of the listed uncertainties.

6.2.1 Absolute Temperature Measurements

All K-type thermocouples were calibrated using a temperature controlled oil bath (model no. 7102 MICRO-BATH from FLUKE Hart Scientific). Calibration was performed at 10 °C intervals between temperatures of 10 and 100 °C with the thermocouples resting in the bath for one hour before one minute of data was acquired and averaged. Once this data was collected, the thermocouple at the heatsink inlet was selected as a reference and all other thermocouples were calibrated to match its output. This calibration was accomplished through polynomial functions describing the offset between the reference thermocouple measurements and all other thermocouple measurements.

Additionally, the reference thermocouple was calibrated to match the controlled bath temperature. The rated accuracy of the temperature controlled bath was ± 0.25 °C with a maximum stability error of ± 0.03 °C and a uniformity error of ± 0.02 °C; thus the total uncertainty of the bath temperature was a summation equal to ± 0.3 °C. Since the reference thermocouple was calibrated to match bath readings, and all other thermocouples were calibrated to match the reference thermocouple readings, then the total uncertainty in all absolute temperature readings was equal to the total bath uncertainty of ± 0.3 °C.

6.2.2 Relative Temperature Measurements

Uncertainties in the measurement of relative temperature presented a much greater dilemma however. As mentioned in previous sections, one method for calculating the heat load was through a first law analysis of the heatsink. This first law analysis was, in turn, a function of the temperature rise across the heatsink. If an absolute temperature error of ± 0.3 °C was maintained without scrutiny, then the error in relative temperature calculated through error propagation would have been ± 0.42 °C. Such an error would have yielded

a heat load uncertainty of ± 114 W at a heat load of 330.4 W. This is clearly an unacceptable uncertainty and fortunately this approach does not survive scrutiny.

Since the thermocouples were calibrated to match the heatsink inlet thermocouple, the ± 0.3 °C error in absolute temperature was no longer relevant. All thermocouples were calibrated to deliver the same output as the reference thermocouple at any given temperature. As a result, the uncertainty in relative temperature was only influenced by the repeatability of the thermocouples themselves. The repeatability of the thermocouples was evaluated by performing a second calibration run after the experiments had been completed and then calculating the difference in measured temperatures relative to the first calibration run. For the most conservative estimate of uncertainty, the maximum difference observed between the two calibration runs (for any thermocouple) was employed as the repeatability error of all thermocouples. This repeatability error was ± 0.021 °C and is unsurprisingly close to the ± 0.02 °C uniformity error of the temperature controlled bath. Through error propagation, the total uncertainty in relative temperature was calculated to be ± 0.03 °C which yielded a heat load uncertainty of 30.8 W at a heat load of 330.4 W.

6.2.3 Pressure Drop Measurements

The differential pressure transducers were subject to a maximum linearity error of ± 1 %, a hysteresis and repeatability error of ± 0.2 %, and a stability error of ± 0.5 %. The resulting total uncertainty in differential pressure measurements was therefore ± 1.7 %. At a pressure drop of 30 kPa, this yielded an uncertainty of ± 0.51 kPa. The sensors were a sufficient distance away from the flow path that the influence of temperature on pressure measurement was of no concern.

6.2.4 Flowrate Measurements

The accuracy of the mechanical flowmeters was ± 2 % plus an observational error of ± 0.05 gal/min (0.19 L/min) due to their analog readouts. Changes in the fluid temperature were also expected to affect the measurement of flowrates. Since piston-type flowmeters were used, the measurements were primarily influenced by form drag which, in turn, is mostly dependent upon the fluid density rather than its viscosity. Based on the water density equation presented earlier, the density of water changes by 2 % between temperatures of 20 and 70 °C. In order to compensate for the effects of fluid temperature changes on flowrate measurement, an additional uncertainty of ± 2 % was conservatively

added to the overall uncertainty of the flowmeters. The total uncertainty in flowrate measurements was thus ± 4 % with an observational error of ± 0.05 gal/min (0.19 L/min). This relative uncertainty resulted in an absolute uncertainty of ± 0.09 gal/min (0.34 L/min) at a flowrate of 1.0 gal/min (3.8 L/min).

6.2.5 Pumping Power Calculations

The uncertainty in pumping power requirement $\dot{W}_{\text{pump}}$ was calculated through error propagation as follows:

$$\delta\dot{W}_{\text{pump}} = \dot{W}_{\text{pump}}\sqrt{\left(\frac{\delta\Delta P}{\Delta P}\right)^2 + \left(\frac{\delta Q}{Q}\right)^2} \tag{6.18}$$

where ΔP and Q represent the pressure drop across and flowrate through any given component and $\delta\Delta P$ and δQ represent their respective uncertainties. At a flowrate of 1.0 gal/min (3.8 L/min), for which the resulting heatsink pressure drop and required pumping power were 14.6 kPa and 0.95 W, the uncertainty in the required pumping power was ± 0.086 W (± 9.0 % of the required pumping power).

6.2.6 Heat Load Calculations, $q = IV$

The multimeters (model no. 52-0052-2 from Mastercraft®) used to measure currents and voltages associated with the cartridge heaters held uncertainties of ± 3 % + 0.05 A and ± 0.8 % + 0.8 V, respectively. That is to say, they were subject to relative errors of ± 3 % and ± 0.8 %, respectively, and absolute errors of 0.05 A and 0.8 V. At the highest tested values of 2.95 A and 112 V, the corresponding measurement uncertainties were ± 0.14 A and ± 1.7 V. When calculating the rate of heat generation of the cartridge heaters q, the uncertainty δq was calculated through error propagation as follows:

$$\delta q = q\sqrt{\left(\frac{\delta I}{I}\right)^2 + \left(\frac{\delta V}{V}\right)^2} \tag{6.19}$$

where δI and δV are the respective measurement errors in current and voltage. This equation yielded a heat load uncertainty of ± 16.5 W at a heat load of 330.4 W which amounts to a 5 % uncertainty.

6.2.7 Heat Transfer to Fluid Calculations, $q_{\text{in}} = \rho Q c_{\text{p}} \Delta T$

When ascertaining the heat load through a first law analysis of the heatsink, the uncertainties in water density and specific heat capacity were also considered. Since the polynomial expression used to describe water density was a function of temperature, the

error in water density resulted from the uncertainty in absolute temperature measurements. Applying the principles of error propagation to the polynomial expression yields the following equation:

$$\delta\rho = \sqrt{\left(\frac{d\rho}{dT}\delta T\right)^2} = \sqrt{[2(-0.0039T) - 0.0585]^2 \cdot \delta T^2} \tag{6.20}$$

With an absolute temperature measurement error δT of ± 0.3 °C, the uncertainty in density $\delta\rho$ was ± 0.18 kg/m^3 at a temperature of 70 °C.

The specific heat capacity of water was represented using a fixed value of 4,180 J/kg·K rather than through a temperature dependent function. As a result, the uncertainty in the specific heat capacity was characterized by the maximum deviation of the specific heat capacity within the temperature range tested. Between 20 and 70 °C, the minimum and maximum values of specific heat capacity are 4,178.2 and 4,189.6 J/kg·K (IAPWS, 2007); thus yielding a deviation of 11.4 J/kg·K. Consequently, the uncertainty in the specific heat capacity of water was prescribed as ± 11.4 J/kg·K which corresponds to a relative uncertainty of ± 0.27 %.

The overall uncertainty in the heat transfer rate to the fluid δq_{in} was then calculated through error propagation as follows:

$$\delta q_{\text{in}} = q_{\text{in}}\sqrt{\left(\frac{\delta\rho}{\rho}\right)^2 + \left(\frac{\delta Q_{\text{int}}}{Q_{\text{int}}}\right)^2 + \left(\frac{\delta c_{\text{p}}}{c_{\text{p}}}\right)^2 + \left(\frac{\delta\Delta T}{T_{\text{out,hs}} - T_{\text{in,hs}}}\right)^2} \tag{6.21}$$

where $\delta\rho$, δQ_{int}, δc_{p}, and $\delta\Delta T$ represent the uncertainties in fluid density, internal flowrate, fluid specific heat capacity, and relative temperature measurements.

Based on the common uncertainties listed in Table 6.1, the overall heat load uncertainty was calculated to be ± 30.8 W at a heat load of 330.4 W. This was not, as shown in Fig. 6.5, the highest possible uncertainty in the rate of heat transfer to the fluid. This figure shows the uncertainty in the heat transfer rate to the fluid as a percentage of the heat transfer rate itself. Reducing the flowrate from 1.5 to 0.3 gal/min (5.7 to 1.1 L/min) increased the heat load uncertainty from ± 27.0 to ± 68.3 W at 330.4 W (from ± 8.2 to ± 20.7 % of the heat load). Maintaining the flowrate at 1.5 gal/min (5.7 L/min) while reducing the heat load from 330.4 to 54.4 W raised the heat load uncertainty from ± 27.0 to ± 12.5 W (from ± 8.2 to ± 23.0 % of the heat load). These trends require explanation.

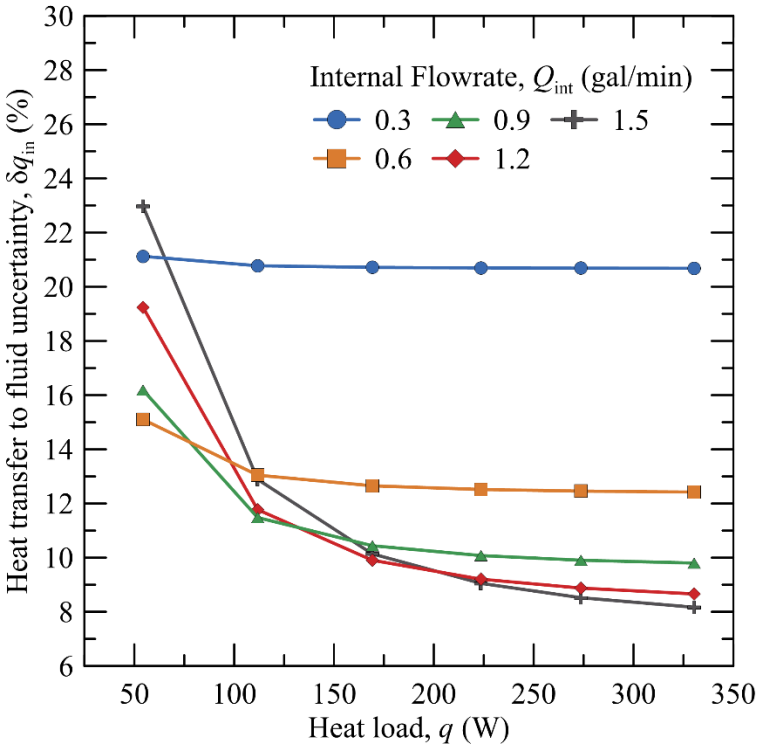

Fig. 6.5 – Uncertainty in the rate of heat transfer to the fluid, $T_{in,ext}$ = 30 ºC, Q_{ext} = 1.0 gal/min, straight channel TCHx

In general, increasing the heat load reduced the relative uncertainty in the rate of heat transfer to the fluid by increasing the temperature rise across the heatsink. Since the error in temperature rise $\delta\Delta T$ was constant at ± 0.03 °C, an increase in the temperature rise itself actually reduced the error contribution of ΔT in Eq. (6.21). Increasing the flowrate further reduced the temperature rise across the heatsink which is why the relative uncertainty in Fig. 6.5 was largest at the highest flowrate of 1.5 gal/min (5.7 L/min) and lowest heat load of 54.4 W; these conditions yielded the lowest temperature rise of 0.14 °C.

At higher heat loads, increasing the flowrate actually reduced the relative uncertainty in the rate of heat transfer to the fluid. The reason for this reduction is that the error contribution of Q_{int} in Eq. (6.21) reduces at higher flowrates. Recall that the uncertainty in flowrate measurements was ± 4 % with an observational error of ± 0.05 gal/min (0.19 L/min). The relative value of this observational error drops from 16.7 to 3.3 % as the flowrate increases from 0.3 to 1.5 gal/min (1.1 to 5.7 L/min). Furthermore, higher heat loads yield a higher temperature rise even while the flowrate is increased and, as already mentioned, a higher temperature rise reduces the error contribution of relative temperature measurement. At a flowrate of 1.5 gal/min (5.7 L/min), a heat load increase from 54.4 to

330.4 W increased the temperature rise from 0.14 to 0.84 °C. Thus the overall effect of increasing the flowrate at high heat loads was a reduction in the relative uncertainty.

These observations were somewhat unpredictable and counterintuitive which is why the uncertainty in the rate of heat transfer to the fluid was previously described as volatile. It was also mentioned previously that the heat load q was used in all subsequent analyses; this decision was justified by the fact that the heat load q was more consistent that the heat transfer rate to the fluid q_{in} and that heat losses accounted for at most 12 % of all heat generated. How accurate is this 12 % heat loss when the uncertainty in the rate of heat transfer to the fluid varies substantially with the flowrate and heat load as shown in Fig. 6.5?

The key to answering this question is understanding that the effectiveness of the insulation enclosing Test Section 1 does not vary when parameters are changed. In other words, if heat losses are calculated to be less than 12 % at higher heat loads and flowrates for which uncertainties are lower, then there is no reason why heat losses should vary significantly once either of these parameters are reduced. Lowering the heat load and flowrate has no impact upon the effectiveness of the insulation – it solely alters the accuracy of heat transfer calculations. Therefore, if the insulation is calculated to maintain at least 88 % of all heat generated under conditions where uncertainties are low, then at least 88 % of all heat generated must be maintained under all other conditions.

6.2.8 Thermal Resistance Calculations

The uncertainty in the heatsink thermal resistance R_{hs} was calculated through error propagation as follows:

$$\delta R_{\text{hs}} = R_{\text{hs}} \sqrt{\left(\frac{\delta \Delta T}{T_{\text{w}} - T_{\text{in,hs}}}\right)^2 + \left(\frac{\delta q_{\text{in}}}{q_{\text{in}}}\right)^2} \tag{6.22}$$

where $\delta \Delta T$ and δq_{in} are the uncertainties in relative temperature measurements and the heat transfer rate to the heatsink. The uncertainty in the TCHx thermal resistance R_{TCHx} was similarly as follows:

$$\delta R_{\text{TCHx}} = R_{\text{TCHx}} \sqrt{\left(\frac{\delta \Delta T}{T_{\text{in,int}} - T_{\text{in,ext}}}\right)^2 + \left(\frac{\delta q_{\text{out}}}{q_{\text{out}}}\right)^2} \tag{6.23}$$

where δq_{out} is the uncertainty in the heat transfer rate out of the internal loop through the internal TCHx plate and was calculated through error propagation as follows:

$$\delta q_{\text{out}} = q_{\text{out}} \sqrt{\left(\frac{\delta\rho}{\rho}\right)^2 + \left(\frac{\delta Q_{\text{int}}}{Q_{\text{int}}}\right)^2 + \left(\frac{\delta c_{\text{p}}}{c_{\text{p}}}\right)^2 + \left(\frac{\delta\Delta T}{T_{\text{in,int}} - T_{\text{out,int}}}\right)^2} \tag{6.24}$$

where $\delta\rho$, δQ_{int}, δc_{p}, and $\delta\Delta T$ represent the uncertainties in fluid density, internal flowrate, fluid specific heat capacity, and relative temperature measurements.

Finally, the uncertainty in the overall system thermal resistance R_{sys} was calculated through error propagation as follows:

$$\delta R_{\text{sys}} = \sqrt{(\delta R_{\text{hs}})^2 + (\delta R_{\text{TCHx}})^2 + (\delta A)^2} \tag{6.25}$$

where δA is the uncertainty in the third and final term in Eq. (6.15) and is defined through error propagation as follows:

$$\delta A = \frac{1}{\rho Q_{\text{int}} c_{\text{p}}} \sqrt{\left(\frac{\delta\rho}{\rho}\right)^2 + \left(\frac{\delta Q_{\text{int}}}{Q_{\text{int}}}\right)^2 + \left(\frac{\delta c_{\text{p}}}{c_{\text{p}}}\right)^2} \tag{6.26}$$

Where $\delta\rho$, δQ_{int}, and δc_{p} represent the uncertainties in fluid density, internal flowrate, and fluid specific heat capacity.

All preceding arguments concerning the effects of flowrate and heat load upon uncertainty remain valid for thermal resistance uncertainties. At higher heat loads and flowrates, thermal resistance calculations are more accurate. At a heat load of 330.4 W and an internal flowrate of 1.0 gal/min (3.8 L/min), the uncertainties in the heatsink and straight finned TCHx thermal resistances were ± 9.2 % of the thermal resistance values. As one would expect, this value seems to echo the percent uncertainty in the heat transfer rate to the fluid. Referring back to Fig. 6.5, the percent uncertainty in q_{in} at a heat load of 330.4 W and an internal flowrate of 1.0 gal/min (3.8 L/min) was roughly ± 9.3 %. At a lower flowrate of 0.3 gal/min (1.1 L/min), these thermal resistance uncertainties increased to roughly ± 20 % of the thermal resistances values.

At a heat load of 330.4 W, the overall thermal resistance uncertainty was ± 7.6 % of the resistance value with an internal flowrate of 1.0 gal/min (3.8 L/min) and ± 16.9 % with a flowrate of 0.3 gal/min (1.1 L/min). These values show that overall system thermal resistances were subject to less uncertainty relative to the individual component thermal resistances.

Chapter 7 - Results and Discussion

This chapter presents the results of the experimental procedure which was designed to evaluate the performance of the proposed thermal contact liquid cooling system. Throughout the chapter, the interpretation of results and subsequent discussions are centered on establishing the ideal configuration and operating parameters for the proposed cooling system. Namely, the goal is to determine which TCHx plate design is most preferable, how influential the internal and external flowrates are upon thermal performance and, most importantly, how high the inlet temperature of the system may be relative to that of a conventional water cooling system.

These question are answered by examining the effects of the four main operating parameters upon the maximum wall temperature, the pressure losses across various components, and the thermal resistance of the overall system. The four parameters are the heat load, the system inlet temperature, and the internal and external flowrates. Additionally, the effect of applying thermal interface materials between the contacting plates of the thermal contact heat exchanger is discussed at the end of the chapter. All other results presented throughout this chapter were based on system measurements with thermal paste applied between the contacting plates.

7.1 Pressure Drop

The pressure losses across the heatsink and different TCHx plates are plotted as a function of the internal flowrate in Fig. 7.1. These tests were conducted with a system inlet temperature of 20 °C and no heat load in order to conservatively characterise pressure losses. At higher temperatures, the pressure drop across any given component would decrease due to higher temperature water being less viscous. The straight channel TCHx yielded the lowest pressure losses with a value of 14.9 kPa at 1.5 gal/min (5.7 L/min). The pressure drop across the heatsink was roughly twice as large as that of the straight channel TCHx at all flowrates with a value of 29.3 kPa at 1.5 gal/min (5.7 L/min). Although it is tempting to link this outcome to the fact that the heatsink channels were half as wide as those constituting the straight channel TCHx, the reality is that this observation is a coincidental outcome influenced by length of and height of the channels as well.

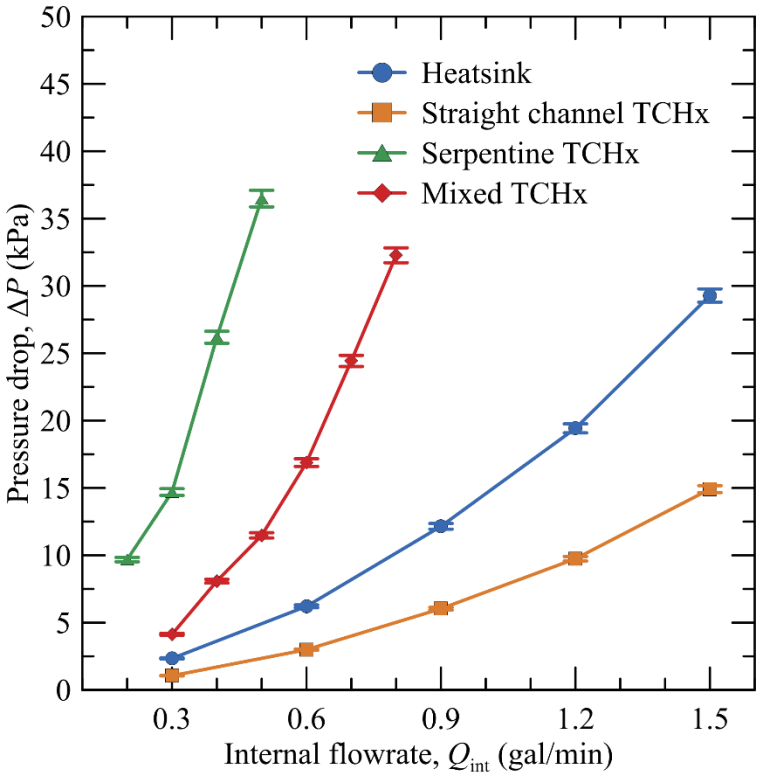

Fig. 7.1 – Pressure drop across heatsink and TCHx plates, q = 0 W, $T_{in,ext}$ = 20 °C, Q_{ext} = Q_{int}

Pressure losses across the serpentine TCHx were unsurprisingly the most significant. In fact, at a flowrate of only 0.5 gal/min (1.9 L/min), the generated pressure drop exceeded the 34.5 kPa measurement limit of the differential pressure transducer; the reading at this flowrate was 36.5 kPa. To put this into perspective, the pressure drop across the straight channel TCHx was 2.4 kPa at the same flowrate which is 15 times smaller. As mentioned in earlier chapters, the relatively substantial pressure drop generated by the serpentine TCHx was due to the fact that it consisted of a single long and winding channel rather than several shorter channels. As a result, fluid velocities were relatively larger, the channel length was greater, and flow turning at the end of each serpentine segment induced additional pressure losses.

Pressure losses across the mixed TCHx were not as problematic relative to the serpentine TCHx. At a flowrate of 0.5 gal/min (1.9 L/min), the pressure drop across the mixed TCHx measured 11.5 kPa versus 36.5 kPa measure across the serpentine TCHx. Relative to the straight channel TCHx, pressure losses was considerable. At a flowrate of 0.8 gal/min (3.0 L/min), the pressure drop across the mixed TCHx was measured to 32.3

kPa which is 4 times larger than the 8.1 kPa pressure drop measured across the straight channel TCHx. Again, it is not surprising that pressure losses across the mixed TCHx were intermediary in this fashion. The numerous smaller straight channels within the mixed TCHx engender a larger flow area relative to the single channel area in the serpentine TCHx. Hence the average fluid velocity through the mixed TCHx is lower which yields a lower pressure drop. However, the mixed TCHx also contained regions that were narrow and where flow turning was prevalent. These regions yielded higher pressure losses relative to the straight channel TCHx which contained no such regions.

7.2 Required Pumping Power

An understanding of pressure losses is instrumental to selecting the appropriate pump for industry implementation; however, a more direct and comprehensive basis for comparison between the different TCHx designs may be attained through pumping power requirements. The pumping power requirements for the heatsink and TCHx plates are plotted as a function of the internal flowrate in Fig. 7.2. With a hypothetical pump operating at 1 W, a flowrate of approximately 1.3 gal/min (4.9 L/min) would be attained through the straight channel TCHx. On the other hand, flowrates of only 0.45 and 0.7 gal/min (1.7 and 2.6 L/min) would be attained through the serpentine and mixed TCHx plates at the same pump load. Furthermore, pressure losses at these flowrates would equate roughly 30 and 10 kPa for the serpentine and mixed TCHx plates respectively; whereas the pressure drop across the straight channel TCHx at a superior flowrate of 1.3 gal/min (4.9 L/min) would be roughly 12 kPa. Therefore, at the same pump load, the straight channel TCHx delivers a higher flowrate with lower pressure losses.

This finding leads to the conclusion that, from the standpoint of pressures and flowrates alone, the serpentine and mixed TCHx designs are inferior to the straight TCHx design. This conclusions is valid firstly because the serpentine and mixed TCHx designs are more likely to exceed the maximum head capacity of a miniature server pump even at inconsiderable flowrates. Secondly, even if pressure losses were not an issue, these two inferior designs would require greater pump loads in order to deliver the same flowrate as that delivered by the straight channel TCHx. Of course, the selection of the ideal TCHx design is contingent upon its thermal performance as well. For instance, if the thermal performance of the serpentine TCHx (at its relatively limited flowrate) substantially

exceeded the thermal performance of the straight channel TCHx (by, for example, lowering the heated surface temperature by 10 °C), then it may very well be the ideal design choice. In order to conduct such an evaluation, the effect of flowrate on thermal performance must be investigated.

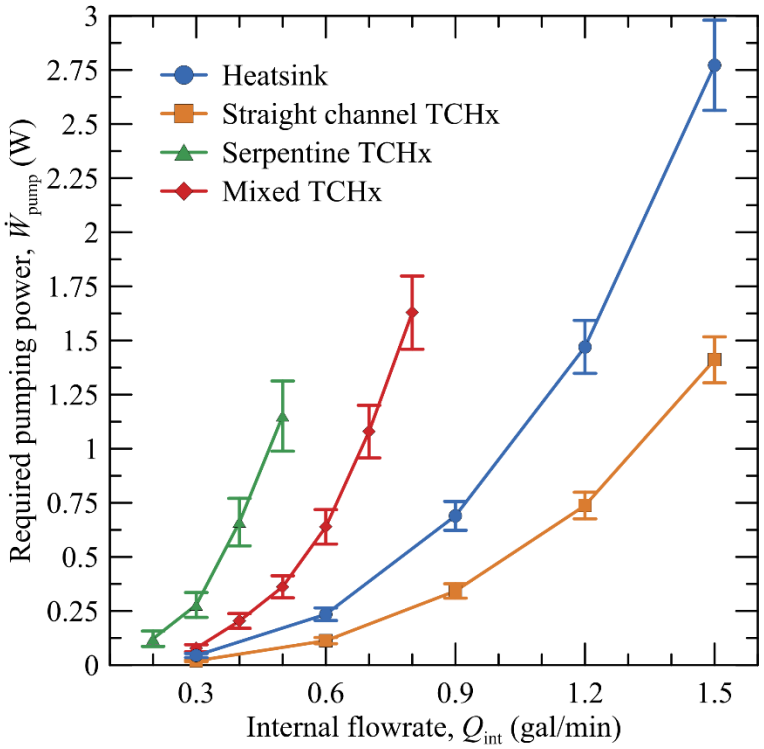

Fig. 7.2 – Pumping power required by the heatsink and TCHx plates, q = 0 W, $T_{in,ext}$ = 20 °C, Q_{ext} = Q_{int}

7.3 Effect of Internal Flowrate

The influence of the internal flowrate Q_{int} on the maximum wall temperature at different heat loads is plotted in Fig. 7.3 for the straight channel TCHx. The system inlet temperatures $T_{in,ext}$ in this test was 30 ºC. The first unsurprising observation is that increasing the heat load shifted the temperatures curves upwards in a linear fashion. Of greater interest is the fact that increasing the flowrate had a more pronounced impact at higher heat loads. At a heat load of 330.4 W, increasing the internal flowrate from 0.3 to 1.5 gal/min (1.1 to 5.7 L/min) reduced the maximum wall temperature by 10 °C from 74.9 to 64.9 °C. Whereas at a heat load of 54.4 W, the same increase in flowrate reduced the maximum wall temperature by only 2.5 °C from 39.2 to 36.7 °C.

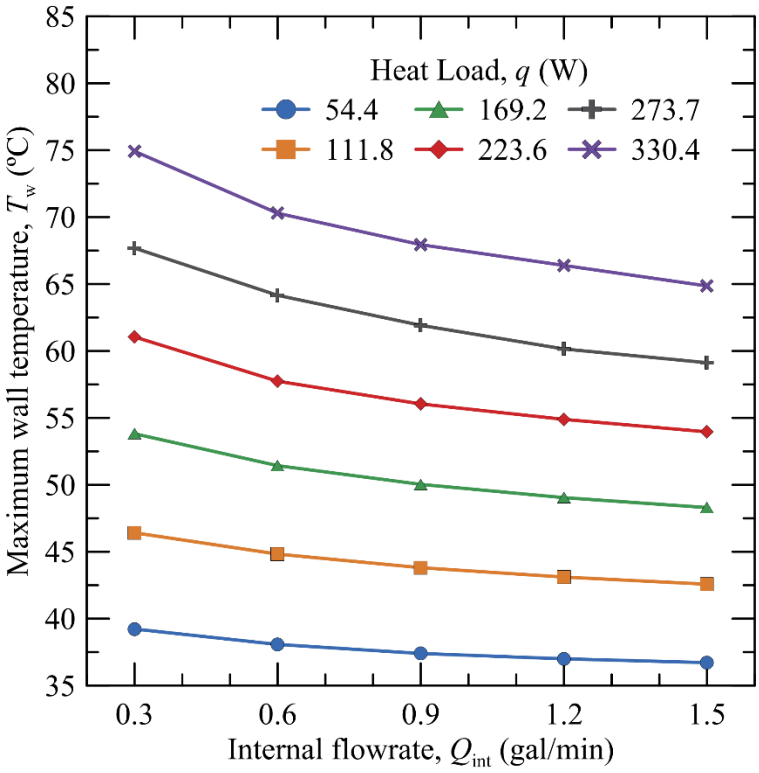

Fig. 7.3 – Effect of internal flowrate Q_{int} on maximum wall temperature for various heat loads q, $T_{in,ext}$ = 30 °C, Q_{ext} = 1.0 gal/min, straight channel TCHx

This finding may be explained from a mathematical standpoint. The wall temperature for a hypothetical low flowrate case may be defined as follows:

$$T_{w,low} = T_\infty + qR_{th,low} \tag{7.1}$$

where $T_{w,low}$ and $R_{th,low}$ are the wall temperature and heatsink thermal resistance when the flowrate is low, T_∞ is the coolant temperature, and q is the heat load. Similarly, the wall temperature for a hypothetical high flowrate case may be defined as follows:

$$T_{w,high} = T_\infty + qR_{th,high} \tag{7.2}$$

where $T_{w,high}$ and $R_{th,high}$ are the wall temperature and heatsink thermal resistance when the flowrate is high. The coolant temperature T_∞ and the heat load q would remain identical in both hypothetical cases. Subtracting Eq. (7.2) from Eq. (7.1) yields the following relationship:

$$\left(T_{w,low} - T_{w,high}\right) = q\left(R_{th,low} - R_{th,high}\right) \tag{7.3}$$

What this equation shows is that the difference in wall temperatures between the high and low flowrate cases is proportional to the difference in heatsink thermal resistances in each case. The factor of proportionality within this relationship is actually the heat load q.

Therefore, at higher heat loads, the same change in thermal resistance between the low and high flowrate cases yields a higher variation in the wall temperature.

Similar plots associated with the serpentine and mixed TCHx designs are shown in Appendix B as they yielded similar conclusions to Fig. 7.3. It is more interesting at this point to compare the thermal performance of all three TCHx designs as a function of the internal flowrate. Such a comparison is shown at the highest heat load of 330.4 W in Fig. 7.4.

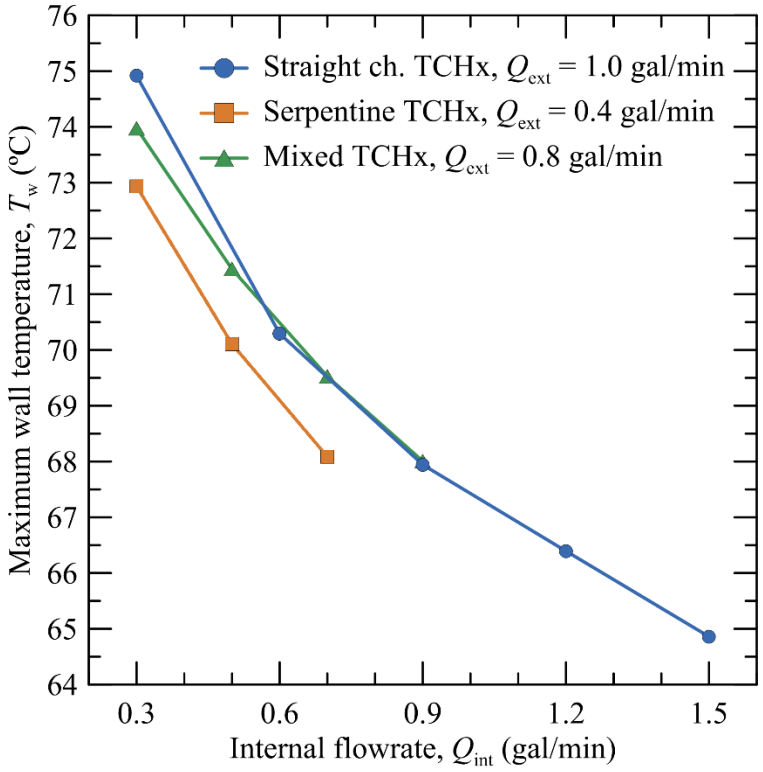

Fig. 7.4 – Effect of internal flowrate Q_{int} on maximum wall temperature for various TCHx designs, q = 330.4 W, $T_{in,ext}$ = 30 °C

At an internal flowrate of 0.3 gal/min (1.1 L/min), the serpentine TCHx design takes the lead by yielding the lowest maximum wall temperature of 72.9 °C while the mixed and straight channel designs yielded maximum wall temperatures of 74 and 74.9 °C. This lead was maintained throughout the range of flowrates tested for the serpentine TCHx design. At its highest tested flowrate of 0.7 gal/min (2.6 L/min), the serpentine TCHx design yielded a maximum wall temperature of 68.1 °C while the mixed and straight channel designs required an internal flowrate of 0.9 gal/min (3.4 L/min) to deliver roughly the same wall temperature. Furthermore, it is worth noting that the external flowrates differ among

the TCHx designs. The serpentine TCHx yielded the lowest wall temperatures even though its external flowrate was the lowest at 0.4 gal/min (1.5 L/min). Clearly, the serpentine TCHx design offers a superior thermal performance even at lower internal and external flowrates. However, are these reduced wall temperatures worth the high pressure and pump loads which accompany the serpentine TCHx design?

The answer is unequivocally no. At a flowrate of 0.5 gal/min (1.9 L/min), the serpentine TCHx design yielded a maximum wall temperature of 70.1 °C which was 1.3 °C lower than that yielded by both the mixed and straight channel TCHx plates. However, the cost of this 1.3 °C temperature drop was a pressure drop of 36.5 kPa which was 15 times greater than the 2.4 kPa pressure drop across the straight channel TCHx at the same flowrate. In terms of pump loads, the 1.3 °C drop cost 1.2 W which was, to reiterate, 15 times greater than the 0.082 W pump load required by the straight channel TCHx at the same flowrate. Clearly, a 1.3 °C temperature drop is not worth pump loads and pressure losses that are 15 times amplified when the absolute temperatures in question range from 60 to 85 °C (this ranges assumes the most problematic scenario with a system inlet temperature of 60 °C).

In terms of a cost comparison, the straight channel TCHx requires an internal flowrate of 0.9 gal/min (3.4 L/min) in order to deliver the same thermal performance as the serpentine TCHx at a flowrate of 0.7 gal/min (2.6 L/min). That is to say, in order to maintain the maximum wall temperature at 68 ºC. These flowrates translate to pumping power requirements of 0.34 W for the straight channel TCHx and roughly 2.7 W for the serpentine TCHx (this latter value was calculated based on a polynomial regression of the serpentine TCHx pumping power requirements shown in Fig. 7.2 since the pressure drop across this heat exchanger plate exceeded the available range of the pressure transducer used). These values indicate that the straight channel TCHx requires pumping loads that are approximately an order of magnitude smaller than those required by the serpentine TCHx in order to deliver the same thermal performance.

The serpentine TCHx is consequently the least ideal choice for a thermal contact heat exchanger. Little discussion is needed to rule out the mixed TCHx as the ideal design choice as well. Referring to Fig. 7.4, the mixed TCHx yields temperatures similar to those of the straight channel TCHx beyond a flowrate of 0.5 gal/min (1.9 L/min). Yet the

pressure losses across the mixed TCHx were four times amplified. Therefore, the mixed TCHx requires additional pumping power while delivering no additional thermal performance beyond 0.5 gal/min (1.9 L/min). These findings leave the straight channel TCHx as the ideal design choice due conclusively to the fact it requires considerably lower pump loads and pump head capacity while delivering a thermal performance that is comparable to the remaining designs.

An additional consideration on the topic of the internal flowrate is the viability of control systems regulating pump activity. What Fig. 7.3 essentially demonstrated was that (in the case of the straight channel TCHx at least) adjusting the flowrate had considerable effects upon the maximum wall temperature. When the internal flowrate was increased from 0.3 to 1.5 gal/min (1.1 to 5.7 L/min), the maximum wall temperature decreased from 74.9 to 64.9 °C. This 10 °C drop is substantial when considering that range of temperatures in question during the associated test was 30 to 85 °C. As a result, there may be benefits in terms of operating costs by implementing a control system which alternates the pump setting between low power and high power modes. At low server heat loads, the pumps would operate in low power mode which delivers low flowrates and conserves energy. Whereas at high server heat loads, high power mode would be activated in order to prevent a processor die from overheating. Such a control system would not require any type of temperature feedback from processor dies; it would operate solely based upon the server heat load.

Finally, a discussion on the ideal internal flowrate will be presented in later chapters. The selection of this parameter is dependent upon the system's thermal performance not just as a function of the internal flowrate, but also as a function of the system inlet temperature $T_{in,ext}$. Before this information is presented, the effect of the external flowrate on the maximum wall temperature is briefly discussed.

7.4 Effect of External Flowrate

Unlike the internal flow, which may vary from one server to another depending upon the heat load, the external flow in an industrial design will be delivered to all server racks using facility level pumps and heat exchangers. Therefore, the system inlet temperature $T_{in,ext}$ and external flowrate Q_{ext} will be uniform for all servers in a given facility. As a

result of this condition, the external flowrate should be specified based upon the worst case scenario, that is, with the highest expected heat load.

The effect of the external flowrate on the maximum wall temperature with a heat load of 330.4 W is plotted in Fig. 7.5 for all TCHx designs. The purpose here is no longer to compare the thermal performances of the various TCHx designs, but rather to discern what the ideal external flowrate should be. It should be noted that internal flowrates were set to the maximum possible values when using serpentine (0.4 gal/min or 1.5 L/min) or mixed (0.8 gal/min or 3.0 L/min) TCHx plates; whereas a nominal flowrate of 1.0 gal/min (3.8 L/min) was used for the straight channel TCHx plate. The magnitudes of the internal flowrate are unimportant since it is the influence of relative changes in the external flowrate that are of interest.

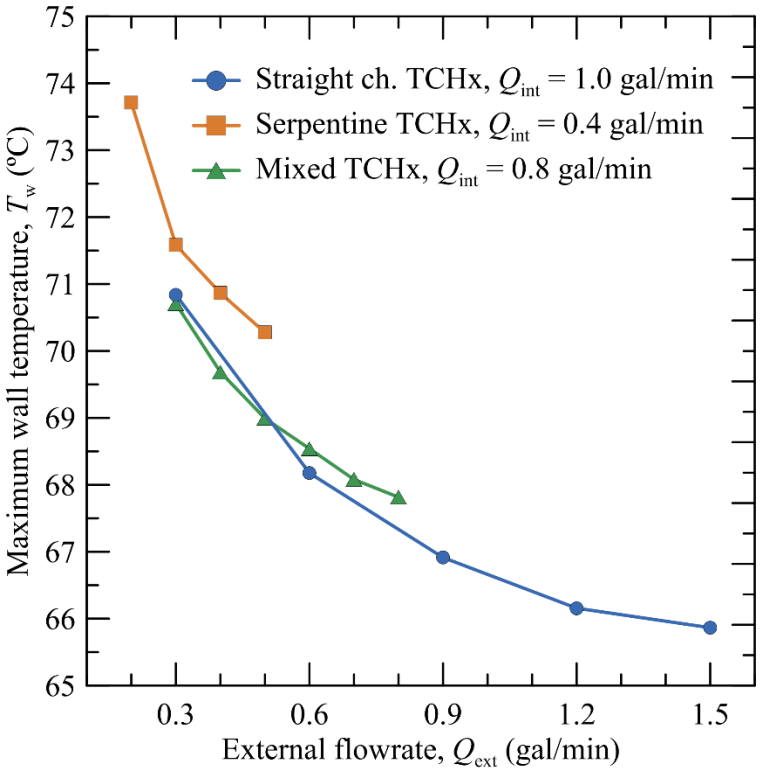

Fig. 7.5 – Effect of external flowrate Q_{ext} on maximum wall temperature for various TCHx designs, q = 330.4 W, $T_{in,ext}$ = 30 °C

It may be observed from Fig. 7.5 that increasing the external flowrate had a lesser effect on the maximum wall temperature than did the internal flowrate. Increasing the external flowrate from 0.3 to 1.5 gal/min (1.1 to 5.7 L/min) while using the straight channel TCHx reduced the maximum wall temperature by 4.9 °C from 70.8 to 65.9 °C. The same

adjustment in the internal flowrate reduced the wall temperature by 10 °C. Similar observations were made while using the remaining TCHx designs.

The reason for this outcome may be that adjusting the internal flowrate alters the thermal resistances of both the heatsink and the TCHx while adjusting the external flowrate only impacts the thermal resistance of the TCHx. In more detail, the overall thermal resistance of the TCHx assembly is the sum of the respective thermal resistances of its internal and external plates. These thermal resistances are in turn influenced by the internal and external flowrates respectively. Therefore, increasing the internal flowrate doubly effects the overall thermal resistance of the entire cooling system relative to an increase in the external flowrate.

As a result of this behaviour, increasing the external flowrate begins to yield diminishing returns earlier than does increasing the internal flowrate. For the straight channel TCHx, maintaining the external flowrate at 1.5 instead of 1.2 gal/min (5.7 instead of 4.5 L/min) results in a pressure drop of 14.9 instead of 9.7 kPa while only reducing the maximum wall temperature by 0.29 °C. Therefore, an external flowrate of 1.0 gal/min (3.8 L/min) or lower may be more appropriate for appreciably reducing the wall temperature without amplifying pressure losses and increasing pumping costs. Similar to the ideal internal flowrate, a more comprehensive selection of the ideal external flowrate will depend on the system performance as a function of the system inlet temperature $T_{in,ext}$. The effects of this parameter will now be discussed.

7.5 Effect of System Inlet Temperature

The effects of the system inlet temperature $T_{in,ext}$ were studied within the context of two different scenarios: a low pump load scenario where both the internal and external flowrates were fixed at 0.3 gal/min (1.1 L/min), and a high pump load scenario where the flowrates were fixed at 1.0 gal/min (3.8 L/min). There was no motivation for this procedure other than to simply characterize the system's thermal performance at two different flowrate extremes. The effect of the system inlet temperature on the maximum wall temperature is plotted for the straight channel TCHx at various heat loads in Fig. 7.6. Similar plots are shown in Appendix B for the serpentine and mixed TCHx designs. These have been omitted from the main body as there is an unnoticeable variation between their resulting temperature curves and those shown in Fig. 7.6.

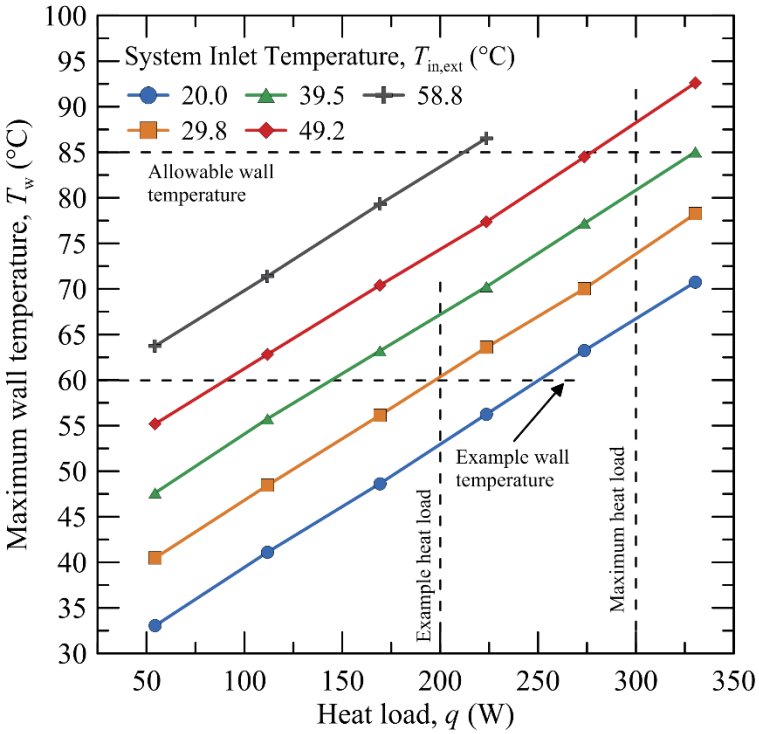

Fig. 7.6 – Effect of the system inlet temperature $T_{in,ext}$ on the maximum wall temperature T_w at low pump loads, Q_{int} = Q_{ext} = 0.3 gal/min, straight channel TCHx

Focusing now on the current plot, it is unsurprising that increasing the system inlet temperature and the heat load both linearly raise the maximum wall temperature. The wall temperature T_w is linearly proportional to these parameters in the following form:

$$T_w = T_{in,ext} + qR_{sys} \tag{7.4}$$

where R_{sys} is the thermal resistance of the entire cooling system and is constant for a given combination of internal and external flowrates. What is more consequential about this figure is the way in which it identifies the thermal limits of the proposed cooling system as a function of the system's inlet temperature and the desired maximum wall temperature.

In this regard, this figure may be used as a design guide by thermal engineers in identify the appropriate system inlet temperature for a given application. For instance, if the processor heat load in a specific application is 200 W and it is required that the maximum wall temperature remain below 60 °C, then the intersection of these coordinates yields the maximum allowable system inlet temperature of 30 °C. This process is illustrated using the dashed lines labelled as *example heat load* and *example wall temperature* in Fig. 7.6.

Even more crucial, this plot provides an answer to the central question of this thesis: what is highest permissible inlet water temperature that maintains the maximum wall temperature below 85 °C at a heat load of 300 W. According to the intersection of the dashed lines labelled as *maximum heat load* and *allowable wall temperature* in Fig. 7.6, the highest permissible system inlet temperature would be approximately 45 °C. This inlet temperature corresponds solely to a system operating with internal and external flowrates of 0.3 gal/min (1.1 L/min) and thus with a cumulative pressure drop of 3.4 kPa (2.34 kPa across the heatsink and 1.06 kPa across the straight channel TCHx) and total pump load of 0.064 W. Given these low pressure losses relative to the performance limits of a typical miniature 12 or 24 V centrifugal pump, there is substantial room for increase of the internal flowrate. Recall that the maximum head capacity of an example miniature centrifugal pump (model TL-B10-B) produced by TOPSFLO ranges from 30 to 78 kPa.

An increase in the flowrate shifts the discussion to Fig. 7.7 which illustrates the effect of the system inlet temperature on the maximum wall temperature for the high pump load case. Relative to Fig. 7.6, both the internal and external flowrates have been raised from 0.3 to 1.0 gal/min (1.1 to 5.7 L/min) in the current figure. This increase in the flowrate raises the system's cumulative pressure drop from 3.4 to approximately 22.5 kPa (15 kPa across the heatsink and 7.5 kPa across the straight channel TCHx) and its total pump load from 0.064 to 1.42 W. Concurrently, increasing the flowrates to 1.0 gal/min (3.8 L/min) also shifts all the temperature curves downwards relative to Fig. 7.6. Now, in order to maintain the maximum wall temperature below 85 °C at a heat load of 300 W, the highest permissible system inlet temperature is closer to 56 °C as opposed to 45 °C when the flowrates were 0.3 gal/min (1.1 L/min). Therefore, increasing the internal and external flowrates from 0.3 to 1.0 gal/min (1.1 to 3.8 L/min) permitted adequate cooling with inlet water that was 11 °C warmer.

This difference of roughly 11 °C in the required system inlet temperature once the flowrates were increased is unsurprising given the previous discussion on the internal and external flowrates. According to Fig. 7.4, increasing the internal flowrate from 0.3 to 1.0 gal/min (1.1 to 3.8 L/min) reduced the maximum wall temperature by roughly 7.5 °C for the straight channel TCHx. According to Fig. 7.5, an identical increase in the external flowrate reduced the maximum wall temperature by roughly 4 °C for the straight channel

TCHx. It is therefore reasonable that increasing both flowrates from 0.3 to 1.0 gal/min (1.1 to 3.8 L/min) shifted the temperature curves in Fig. 7.6 down by roughly 11 °C to deliver the maximum wall temperatures plotted in Fig. 7.7.

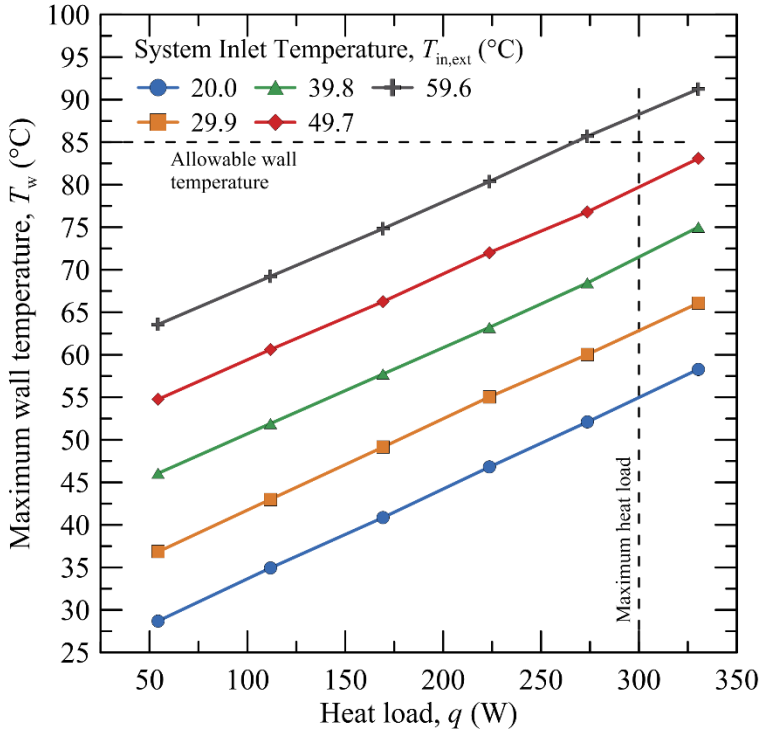

Fig. 7.7 – Effect of the system inlet temperature $T_{in,ext}$ on the maximum wall temperature T_w at high pump loads, Q_{int} = Q_{ext} = 1.0 gal/min, straight channel TCHx

Now that the effects of all system parameters have been ascertained and the thermal limits of the proposed cooling system have been defined, the only outstanding question is how the proposed system compares with a conventional water cooling system. Moreover, it would also be useful to compare its thermal performance to that of air cooling which is currently the most prevalent solution in large data centers. In order to answer these questions, various thermal resistances must first be calculated.

7.6 Thermal Resistance

7.6.1 Heatsink Thermal Resistance

The thermal resistance of the heatsink as a function of the internal flowrate is plotted in Fig. 7.8. The plotted thermal resistance values were calculated at a heat load of 330.4 W and a system inlet temperature of 30 °C. Thermal resistances were also calculated at other heat loads and inlet temperatures and were found to be within 5 % of the values

shown in Fig. 7.8. This consistency in thermal resistance values irrespective of the heat load and inlet temperature was expected after having observed the near-perfect linearity of the wall temperature curves in Fig. 7.7.

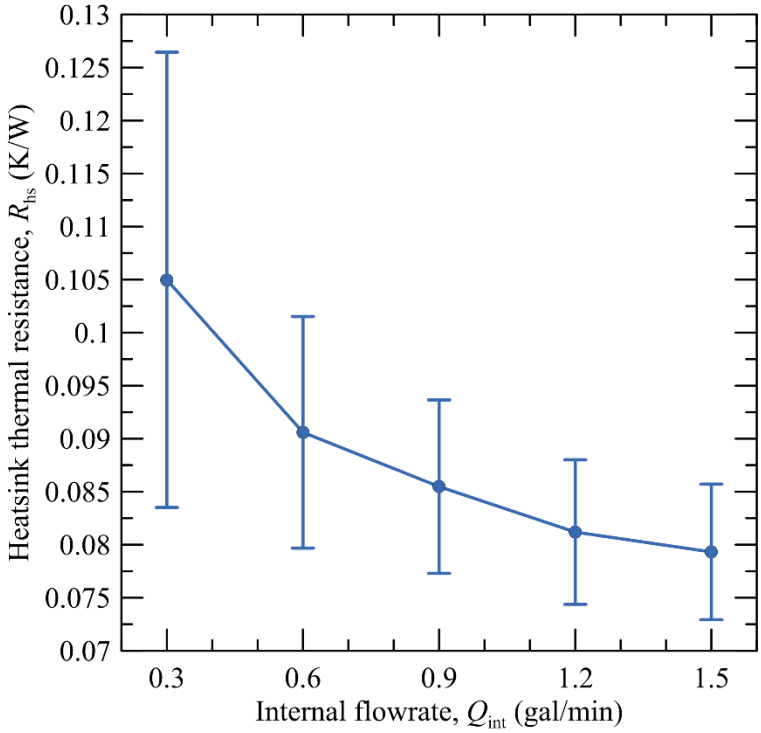

Fig. 7.8 – Heatsink thermal resistance as a function of internal flowrate, q = 330.4 W, $T_{in,ext}$ = 30 °C, Q_{ext} = 1.0 gal/min, straight channel TCHx

Referring now to Fig. 7.8, it is clear that increasing the flowrate enhanced convective heat transfer which in turn reduced the overall thermal resistance of the heatsink. At the lowest tested flowrate of 0.3 gal/min (1.1 L/min), the heatsink thermal resistance was highest at 0.105 K/W. To put this value into perspective, the lowest possible thermal resistance of an air cooled 2U server heatsink, which occurs at an air flowrate of 45 ft^3/min (337 gal/min or 1276 L/min), has been measured to be approximately 0.175 K/W (Geng, 2015). Therefore, the thermal resistance of the proposed liquid cooled heatsink is 40 % lower than that of the air cooled heat sink. What is truly impressive is that an air cooled 2U server heatsink contains fins that are more than 3 in. (7.6 cm) tall while the proposed liquid cooled heatsink channels are only 2.3 mm tall. Even if the heatsink aluminum cover is taken into account, the proposed liquid cooled heatsink is still less than 1 in. (2.5 cm) tall. Increasing the flowrate further reduced thermal resistances with diminishing returns. At a flowrate of 1.0 gal/min (3.8 L/min), the heatsink thermal resistance was reduced to

roughly 0.085 K/W. Further increasing the flowrate to 1.5 gal/min (5.7 L/min) yielded a thermal resistance of 0.08 K/W.

7.6.2 TCHx Thermal Resistance

The thermal resistances of the three TCHx designs are compared in Fig. 7.9. The thermal resistances of all TCHx assemblies were calculated for the low pump load case with internal and external flowrates of 0.3 gal/min (1.1 L/min). The thermal resistance of the straight channel TCHx was additionally calculated for the high pump load case with internal and external flowrates of 1.0 gal/min (3.8 L/min).

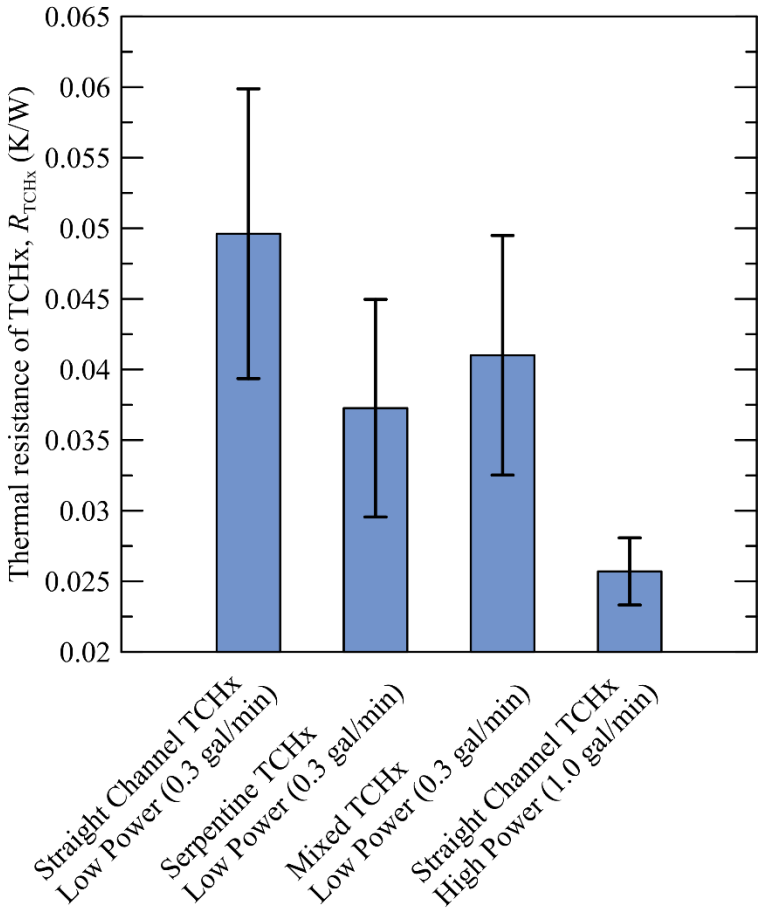

Fig. 7.9 – Thermal resistance of TCHx assemblies for various pump load cases, q = 330.4 W, $T_{in,ext}$ = 30 °C

Prior to discussing the results, further explanation is necessary concerning the physical significance of these thermal resistances. As discussed in earlier chapters, these thermal resistances were calculated based upon the difference in inlet temperatures of the internal and external TCHx plates. Therefore, if the heat load is given, these thermal

resistances may be used to estimate how much cooler the external inlet temperature must be relative to the internal inlet temperature of the TCHx assembly. The lower the thermal resistance, the warmer the external inlet temperature that is permissible.

Under a low pump load (0.3 gal/min or 1.1 L/min), the straight channel TCHx yielded the highest thermal resistance value of 0.050 K/W. Therefore, at a heat load of 300 W, the required external inlet temperature for the straight channel TCHx must be 15.0 °C cooler than the desired internal inlet temperature. The lowest thermal resistance (under a low pump load) of 0.037 K/W was delivered by the serpentine TCHx. At the same heat load of 300 W, the required external inlet temperature for the serpentine TCHx must be 11.1 °C cooler than the desired internal inlet temperature. Therefore, the serpentine TCHx permits an external inlet temperature that is 3.9 °C warmer than that permitted by the straight channel TCHx. The serpentine TCHx may seem more desirable in this regard; however, the serpentine TCHx also generates 14.7 kPa of pressure drop at 0.3 gal/min (1.1 L/min) whereas the straight channel TCHx generates only 1.1 kPa. Clearly, the serpentine TCHx is no longer preferable when pressure losses are taken into consideration.

Moreover, even when the straight channel TCHx is used under a high pump load (1.0 gal/min or 3.8 L/min), the generated pressure drop still remains roughly 50 % lower than that of the serpentine TCHx used under a low pump load. The pressure drop across the straight channel TCHx at a high pump load is roughly 7.5 kPa while its thermal resistance is now 0.026 K/W. As a result, at a heat load of 300 W, the required external inlet temperature for the straight channel TCHx must be only 7.8 °C cooler than the desired internal inlet temperature. In conclusion, running the cooling system at a high pump load (1.0 gal/min or 3.8 L/min internal and external flowrates) while using the straight channel TCHx yielded the most desirable results from the standpoints of both thermal performance and pressure losses.

7.6.3 System Thermal Resistance

Finally and most importantly, the overall thermal resistances of the proposed cooling system using each TCHx design are plotted in Fig. 7.10. The observed pattern unsurprisingly resembles that observed in Fig. 7.9. The system with the serpentine TCHx again yielded the lowest thermal resistance under a low pump load while the lowest thermal resistance resulted from a system with the straight channel TCHx operating under a high

pump load. The reason for this similarity in the pattern is simply that the heatsink thermal resistance remains constant regardless the TCHx assembly used; therefore, only the variations in the thermal resistances of the TCHx assemblies will influence the variations in thermal resistances of the overall system.

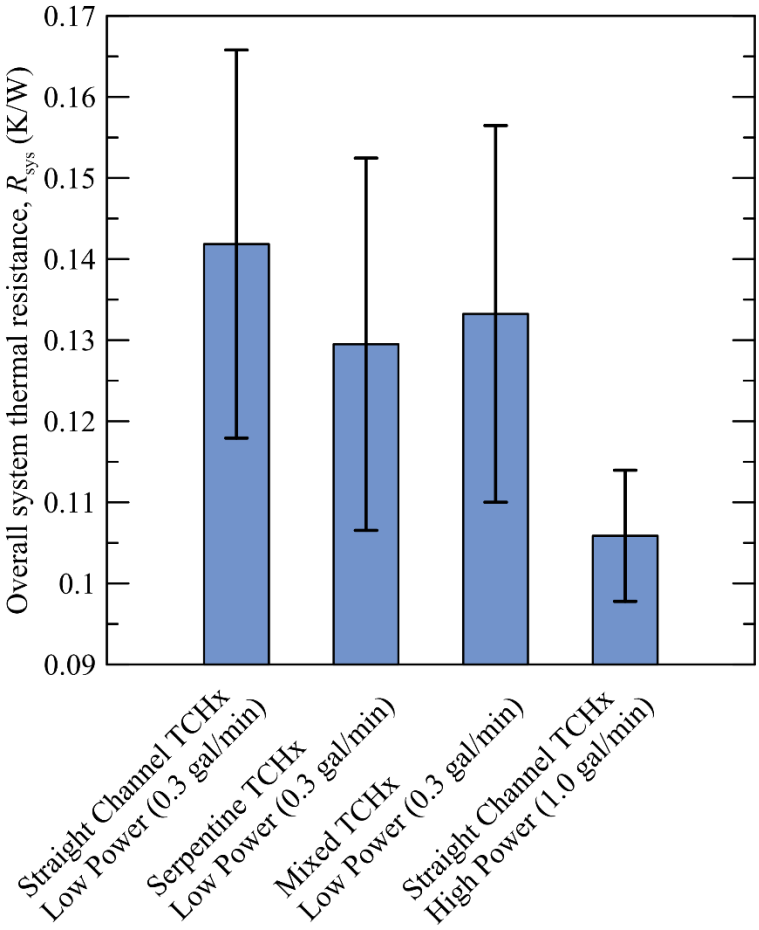

Fig. 7.10 – Overall system thermal resistance for various pump load cases, q = 330.4 W, $T_{in,ext}$ = 30 °C

As a result, the discussions and conclusions from the previous section remain valid for the current plot. It is worthwhile to note that even the worst thermal performance observed in Fig. 7.10 is still an improvement relative to air cooling. The highest thermal resistance of 0.14 K/W corresponded to a system operating at a low pump load and using the straight channel TCHx. However, even this thermal resistance is 20 % lower than the minimum 0.175 K/W thermal resistance of an air cooled 2U server heatsink. Running the same system at a high pump load reduced the system thermal resistance to 0.106 K/W which is 39.4 % lower than that of an air cooled heatsink. Therefore, with a heat load of

300 W and a desired maximum wall temperature of 85 °C, the proposed cooling system requires inlet water at 53.2 °C when operating at a high pump load (1.0 gal/min or 3.8 L/min) while an air cooling system requires inlet air at 32.5 °C with an air flowrate of 337 gal/min (1276 L/min).

On a side note, recall that the system thermal resistance was not calculated based upon the temperature difference between the heated surface and the system inlet. Rather, it was calculated based upon a derived expression which was a function of the individual thermal resistances of the heatsink and TCHx as well as thermal mass of the fluid. Given that the system thermal resistance permits direct calculation of the required system inlet temperature, it would be interesting to compare the result of such a calculation with the required system temperatures obtained visually from Fig. 7.6 for the low pump load case and Fig. 7.7 for the high pump load case.

For the low pump load case, the calculated system thermal resistance with a straight channel TCHx is 0.14 K/W which, for a 300 W heat load and 85 ºC allowable wall temperature, predicts a required system inlet temperature of 43 ºC. The required system inlet temperature under the same operating conditions obtained visually from Fig. 7.6 was roughly 45 ºC. This 2.0 ºC disparity is reasonable given the ± 16.9 % uncertainty in system thermal resistance calculations at low pump loads. Repeating this comparison for the high pump load case yields a similar outcome with a predicted inlet temperature of 53.2 ºC and a visually obtained inlet temperature of roughly 56 ºC from Fig. 7.7. Again, this 2.8 ºC disparity is reasonable given the ± 7.6 % uncertainty in system thermal resistance calculations at high pump loads. It is the opinion of the author that the required system inlet temperatures calculated via the thermal resistance serve as a better indicator of thermal performance. Not only are these inlet temperatures lower than those obtained visually (which renders them more conservative); the calculation comprising the overall system thermal resistance factors out heat losses and pump heat loads because it is solely based upon the individual thermal resistances of the heatsink and thermal contact heat exchanger.

On a more significant note, the thermal resistances plotted in Fig. 7.10 deliver the final piece of information necessary to begin comparing the proposed cooling system to a conventional water cooling system. As first mentioned in previous chapters, a conventional water cooling system contains no additional heat exchangers within the

server; therefore, the heatsink inlet and outlet temperatures are equivalent to the system inlet and outlet temperatures for a conventional water cooling system. According to this definition, the thermal resistance of the heatsink plotted in Fig. 7.8 must also therefore be equivalent to the thermal resistances of a conventional water cooling system. As result, the proposed cooling system may be directly compared to a conventional water cooling system by simply comparing the system thermal resistances plotted in Fig. 7.10 to the heatsink thermal resistances plotted in Fig. 7.8.

Assuming the following operating conditions: a heat load of 300 W, a low pump load (0.3 gal/min or 1.1 L/min internal and external flowrates), and a desired maximum wall temperature of 85 °C, then a conventional water cooling system with a heatsink thermal resistance of 0.105 K/W at 0.3 gal/min (3.8 L/min) will necessitate a system inlet temperature of 53.5 °C. For the same operating conditions, the proposed cooling system with a straight channel TCHx and a resulting thermal resistance of 0.14 K/W will necessitate a system inlet temperature of 43.0 °C. Therefore, for the same set of operating conditions at a low pump load, the proposed cooling system (using a straight channel TCHx) requires inlet water that is 10.5 °C cooler than that required by a conventional water cooling system.

Repeating the same calculation at a high pump load yields required inlet temperatures of 59.5 °C for a conventional water cooling system (heatsink thermal resistance of 0.085 K/W) and 53.2 °C for the proposed cooling system with a straight channel TCHx (thermal resistance of 0.106 K/W). Interestingly, the proposed system now requires inlet water that is only 6.3 °C cooler than that of the conventional system.

This reduction in the temperature differences between the two systems is a perfectly reasonable outcome which requires a simple mathematical explanation. The required inlet temperatures of the conventional and proposed cooling systems may be defined as follows:

$$\left(T_{\text{in,ext}}\right)_{\text{conv}} = T_{\text{w}} - q\left(R_{\text{sys}}\right)_{\text{conv}} \tag{7.5}$$

$$\left(T_{\text{in,ext}}\right)_{\text{prop}} = T_{\text{w}} - q\left(R_{\text{sys}}\right)_{\text{prop}} \tag{7.6}$$

where $(T_{\text{in,ext}})_{\text{conv}}$ and $(T_{\text{in,ext}})_{\text{prop}}$ represent the required inlet temperatures of the two systems, $(R_{\text{sys}})_{\text{conv}}$ and $(R_{\text{sys}})_{\text{prop}}$ represent the thermal resistances of the two systems, and q represents the heat load. The difference between the inlet temperatures may then be defined as follows:

$$\left[\left(T_{\text{in,ext}}\right)_{\text{conv}} - \left(T_{\text{in,ext}}\right)_{\text{prop}}\right] = q\left[\left(R_{\text{sys}}\right)_{\text{prop}} - \left(R_{\text{sys}}\right)_{\text{conv}}\right] \quad (7.7)$$

What this equation shows is that the difference between the inlet temperatures of the two systems is proportional to the absolute difference between their respective thermal resistances. Now if the flowrate is increased sufficiently such that both thermal resistances are reduced by an arbitrary 25 %, the resulting difference in inlet temperatures would equate:

$$\left[\left(T_{\text{in,ext}}\right)_{\text{conv}} - \left(T_{\text{in,ext}}\right)_{\text{prop}}\right]_{\text{high flow}} = \frac{3}{4}q\left[\left(R_{\text{sys}}\right)_{\text{prop}} - \left(R_{\text{sys}}\right)_{\text{conv}}\right] \quad (7.8)$$

Therefore, by reducing the thermal resistance of each system by 25 %, the actual difference between the inlet temperatures also decreases by 25 %. This example is not far from reality since the thermal resistance of the heatsink decreased by 19.0 % as the flowrate was increased from 0.3 to 1.0 gal/min (1.1 to 3.8 L/min) while the thermal resistance of the proposed system decreased by 24.3 %.

7.7 Effect of Thermal Interface Material

One final consideration when designing a TCHx is whether thermal interface material should be applied between the contacting surfaces of the heat exchanger plates. It would be preferable from the standpoint of installation and maintenance if no TIM was required. If no thermal paste or grease had to be cleaned off and reapplied each time a server was hot swapped, the down time for swapping components would be reduced and no supply of TIM to remote areas would be necessary. Regardless of these potential benefits, removing thermal interface materials from the design would only be practical if such a change did not significantly raise the maximum wall temperature; which would, in turn, necessitate lower inlet water temperatures and further increase cooling costs.

All results presented thus far were measured while thermal paste (TGREASE 880 from Laird Technologies®) was applied between the contacting surfaces of the TCHx assemblies. The effect of eliminating thermal paste from the straight channel TCHx assembly on the maximum wall temperature is shown in Fig. 7.11. At a low heat load of 54.4 W, removing thermal paste from the straight channel TCHx increased the maximum wall temperature by 5.7 °C from 37.1 to 42.8 °C. This disparity between the two cases increased with the heat load. At a heat load of 330.4 W, removing thermal paste increased the maximum wall temperature by 13.4 °C from 66.9 to 80.3 °C. The reason behind this

increase in disparity has already been discussed. The difference between the maximum wall temperatures from the two cases is proportional to the difference between their respective thermal resistances and the proportionality factor in this relationship is the heat load. Therefore, as the heat load increases, the same difference between the respective thermal resistances yields a larger temperature difference.

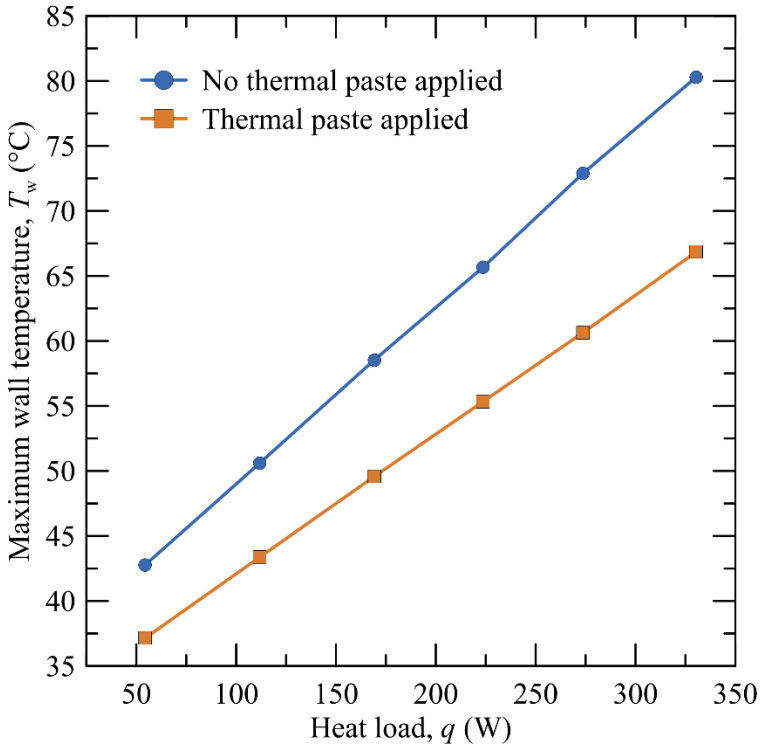

Fig. 7.11 – Effect of thermal interface materials between TCHx plates on the maximum wall temperature, $T_{in,ext}$ = 30 °C, Q_{int} = 1.0 gal/min, Q_{ext} = 1.0 gal/min, straight channel TCHx

For a more general comparison between these cases, the system thermal resistance without thermal paste applied was calculated at the highest heat load to be 0.15 K/W. Since both the internal and external flowrates during this specific experiment were fixed at 1.0 gal/min (3.8 L/min), the operating conditions were identical to the high pump load scenario from the previous section. The system thermal resistance with thermal paste applied has already been calculated for the high pump load scenario to be 0.106 K/W. Therefore, removing thermal paste from the straight channel TCHx increased the overall system thermal resistance by 42 % from 0.106 to 0.15 K/W. At a heat load of 300 W and a high pump load, the system with thermal paste requires an inlet temperature of 53.2 °C to maintain the maximum wall temperature below 85 °C while the system without thermal

paste requires an inlet temperature of 40 °C to meet the same goal. The better design choice would thus be to maintain thermal paste within the TCHx assemblies as withdrawing it would reduce the required system inlet temperature by 13.2 °C.

7.8 Concluding Remarks

An assessment of the effect of the internal flowrate upon the maximum wall temperature showed that the serpentine TCHx plate design offered the best thermal performance. However, this plate design also yielded the highest pressure losses. It was consequently determined that in order to deliver the same thermal performance, the serpentine plate design required a pump load which was approximately an order of magnitude greater than that required by the straight channel plate design. The pump loads were roughly 2.7 versus 0.34 W, respectively. Conclusively, the straight channel TCHx plate was established as the most preferable heat exchanger design.

In regards to the influence of flowrate upon the system's thermal performance, it was established that increasing the internal flowrate was twice as influential in reducing the maximum wall temperature as was increasing the external flowrate. A rise in the internal flowrate from 0.3 to 1.5 gal/min (1.1 to 5.7 L/min) reduced the maximum wall temperature by 10 ºC while the same rise in the external flowrate yielded a temperature reduction of 4.9 ºC. The conclusion drawn here was that varying the internal flowrate is an effective means of regulating the maximum wall temperature. That is to say, the internal flowrate may be reduced when heat loads are moderate and raised only when heat loads are excessive as a means of preserving energy. The external flowrate, on the other hand, should be maintained at 1.0 gal/min (3.8 L/min) or less as diminished returns were evident beyond this point.

The most important topic of discussion within this chapter was undoubtedly the system inlet temperature necessary for maintaining maximum wall temperatures below the recommended 85 ºC limit at a heat load of 300 W. Based on a direct analysis of experimental results, water entering the system must be at most 45 ºC when internal and external flowrates are held fixed at 0.3 gal/min (1.1 L/min) and at most 56 ºC when they are held fixed at 1.0 gal/min (3.8 L/min). Based upon computed system thermal resistance values, these temperature limits were calculated to be 43 and 53.2 ºC. This latter approach

is preferable as the computed system thermal resistances neglect the effects of heat losses and pump heat loads present during experimentation.

With thermal resistance values established for the overall system as well as individual components, the thermal performance of the proposed cooling system was compared to that of a conventional water cooling system. At a heat load of 300 W and a maximum allowable wall temperature of 85 ºC, a conventional water cooling system required inlet water that was 10.0 ºC warmer than that required by the proposed system at low pumps loads (internal and external flowrates of 0.3 gal/min or 1.1 L/min). At high pumps loads (internal and external flowrates of 1.0 gal/min or 3.8 L/min), the inlet water required by the conventional system was only 6.3 ºC warmer. The significance of these difference in the inlet system inlet temperatures are discussed in the next chapter.

Finally, the influence of thermal interface materials upon thermal performance was assessed. It was established that thermal interface materials are necessary between the contacting plates of the thermal contact heat exchanger as their withdrawal would reduce the required system inlet temperature by 13.2 ºC at a heat load of 300 W. This reduction in the inlet temperature would further increase the cost of vapor-compression refrigeration cooling and render the proposed thermal contact liquid cooling system impractical.

Chapter 8 - Design Considerations

The aim of this chapter is to present a discussion on additional design considerations that may be of use to thermal engineers seeking to implement the proposed thermal contact liquid cooling system in industrial applications. Topics that are investigated include cooling costs, miniature centrifugal pump capabilities, cooling system configurations within servers containing multiple processors, and methods of integrating the proposed cooling system within existing server racks.

8.1 Cooling Costs

The primary purpose of increasing the inlet temperature of any cooling system is to reduce the operating costs of cooling. This reduction in cooling costs is achieved either because a warm coolant necessitates less compressor work in order for its thermal energy to be dissipated to warmer ambient air, or preferably because the coolant temperature is sufficiently warmer than the ambient air such that vapor-compression cooling can be relinquished altogether. The latter scenario is referred to as free cooling which is simply the process of dissipating heat from a facility without the use of vapor-compression refrigeration systems and is only possible when the external ambient air temperature is adequately lower than the cooling system inlet temperature (Zhang et al., 2014).

On that note, three possible scenarios exist: the first involves ambient temperatures that are low enough such that both the conventional and proposed cooling systems can exploit free cooling, the second involves ambient temperatures that fall within a narrow range such that only the conventional system exploits free cooling, the third (and most likely) scenario involves ambient temperatures that are high enough such that neither system exploits free cooling. The first scenario requires neither analysis nor discussion. If both system were free cooled, then their respective operating costs for refrigeration would be zero. The subsequent sections describe the implications of the remaining two scenarios as relevant to a thermal engineer designing either type of water cooling system.

8.1.1 Free Cooled Conventional Water Cooling System

The required inlet temperature of the proposed cooling system has been, as expected, consistently lower than that of a conventional cooling system. At a heat load of 300 W and a low pump load, the proposed cooling system with a straight channel TCHx required an

inlet temperature of 43.0 ºC in order to maintain the wall temperature below 85 ºC while its conventional counterpart required a warmer inlet temperature of 53.5 ºC. Therefore, for this specific case, a conventional water cooling system can exploit free cooling in regions that are 10.5 ºC warmer.

The implication here is that there exists a 10.5 ºC ambient temperature range within which the conventional system could exploit free cooling while the proposed system could not. If ambient temperatures fell below this range, then both systems would exploit free cooling. If ambient temperatures rose above this range, then neither system would exploit free cooling. At a high pump load, this temperature difference reduced to 6.3 ºC; thus further narrowing the range of ambient temperatures which are advantageous solely to a conventional water cooling system.

If ambient temperatures fell within this range, then the cost savings associated with using a conventional water cooling system instead of the proposed system would be 100 %. The reason being that the conventional system is free cooled (zero refrigeration costs) while the proposed system is not (nonzero refrigeration costs). However, such cost savings only render a conventional cooling system advantageous if ambient temperatures remained within this narrow range of, for instance, 10.5 or 6.3 ºC for an extended period of time. If, for instance, a server room was being designed for a region in which ambient air temperatures remained within such ranges for six months in a given year, then the costs savings associated with employing a conventional water cooling system instead of the proposed system would be roughly 50 %. It is the task of a thermal engineer to determine how realistic such a scenario would be for a given application and then to weigh such cost savings against the strictness of reliability constraints for said application.

8.1.2 Analysis of a Vapor-Compression Refrigeration Cycle

If ambient temperatures were so high that neither system could exploit free cooling, then the conventional water cooling system would still incur vapor-compression refrigeration costs that are lower than those incurred by the proposed system. Chiller performance data that would permit quantification of this claim is unfortunately scarce for water temperatures higher than 30 ºC. Therefore, the relative cost of operating a conventional water cooling system was approximated by analyzing the rudimentary vapor-compression refrigeration cycle shown in Fig. 8.1.

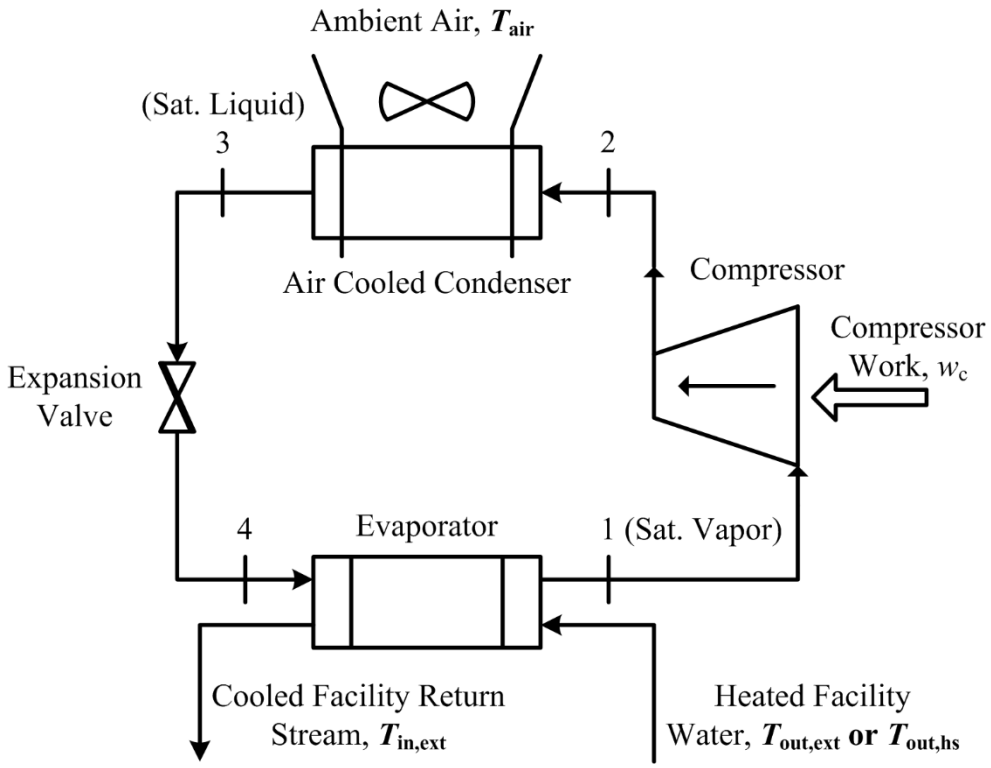

Fig. 8.1 – Schematic of a basic vapor-compression refrigeration cycle using R134a

This cycle consists of an evaporator which extracts heat from the heated facility water. For the proposed cooling system, the heated facility water is analogous to water leaving the external TCHx plate. For a conventional cooling system, the heated facility water is analogous to water directly leaving the heatsink. Either way, the cooled return stream to the facility is analogous to the cooling system inlet water and its temperature is therefore the system inlet temperature $T_{in,ext}$.

In order to attain sufficient heat extraction from the facility water stream, it was assumed that the outlet temperature of the evaporator T_1 was 10 ºC lower than the system inlet temperature $T_{in,ext}$. Additionally, it was assumed for simplicity that the refrigerant R134a leaving the evaporator was in a saturated vapor state at location 1. Likewise, in order attain sufficient heat expulsion to the ambient air, it was assumed that the outlet temperature of the condenser T_3 was 10 ºC higher than the ambient air temperature T_{air}. Again, it was assumed for simplicity that the refrigerant R134a leaving the air cooled condenser was in a saturated liquid state at location 3.

The isentropic efficiency of the compressor was irrelevant as the aim of this exercise was to determine the compressor work required by a conventional water cooling system as

a percentage of the compressor work required by the proposed system. This calculation was performed at heat loads q ranging from 0 to 300 W, ambient air temperatures T_{air} ranging from 30 to 60 ºC, and allowable die temperatures T_w of 60 and 85 ºC. Based upon these parameters, the required system inlet temperatures for a conventional water cooling system $(T_{in,ext})_{conv}$ and the proposed cooling system $(T_{in,ext})_{prop}$ were calculated as follows:

$$\left(T_{\text{in,ext}}\right)_{\text{conv}} = T_{\text{w}} - q\left(R_{\text{sys}}\right)_{\text{conv}} \tag{8.1}$$

$$\left(T_{\text{in,ext}}\right)_{\text{prop}} = T_{\text{w}} - q\left(R_{\text{sys}}\right)_{\text{prop}} \tag{8.2}$$

where $(R_{sys})_{conv}$ and $(R_{sys})_{prop}$ as the thermal resistances of the two systems and q is the heat load. The refrigerant temperatures at states 1 and 3 were calculated based on the 10 ºC temperature difference assumption as follows:

$$(T_1)_{\text{conv}} = \left(T_{\text{in,ext}}\right)_{\text{conv}} - 10\ ℃ \tag{8.3}$$

$$(T_1)_{\text{prop}} = \left(T_{\text{in,ext}}\right)_{\text{prop}} - 10\ ℃ \tag{8.4}$$

$$T_3 = T_{\text{air}} + 10\ ℃ \tag{8.5}$$

where $(T_1)_{conv}$ and $(T_1)_{prop}$ represent the refrigerant temperatures at state 1 for both cooling systems. The temperature at state 3 was common to both cases as the ambient air temperature was independent of the cooling system in use.

With these temperatures calculated, the properties of R134a were estimated at states 1, 2, and 3 using digitized thermodynamic property tables (Sonntag et al., 2003) for which MATLAB code is provided in Appendix C. The only assumptions necessary for approximating thermodynamic properties at state 2 were negligible pressure losses across the air cooled condenser, which set the pressure at state 2 equal to that calculated for state 3, and zero entropy change across the compressor, which set the isentropic entropy at state 2 equal to that calculated for state 1. As already mentioned, this isentropic assumption was perfectly acceptable since it was the ratio of compressor work associated with the two cooling systems that was of interest rather than the magnitudes of compressor work. This ratio was calculated as follows:

$$w_r = \frac{(w_c)_{\text{conv}}}{(w_c)_{\text{prop}}} \times 100 = \frac{(h_{2s})_{\text{conv}} - (h_1)_{\text{conv}}}{(h_{2s})_{\text{prop}} - (h_1)_{\text{prop}}} \times 100 \tag{8.6}$$

where $(w_c)_{conv}$ and $(w_c)_{prop}$ represent the compressor work required in conjunction with each of the two cooling systems, $(h_1)_{conv}$ and $(h_1)_{prop}$ represent the refrigerant enthalpies at state

1 for each of the two cooling systems, and $(h_{2s})_{conv}$ and $(h_{2s})_{prop}$ represent the isentropic refrigerant enthalpies at state 2 for each of the two cooling systems.

8.1.3 High Ambient Temperature Scenario

The compressor work ratios w_r associated with an allowable die temperature of 60 ºC are plotted in Fig. 8.2. What this figure essentially indicates is how much energy or operating expenses would be saved if a conventional water cooling system is used instead of a thermal contact liquid cooling system. For clarity, a compressor work ratio of zero indicates that the conventional cooling system was able to exploit free cooling at the given combination of heat load and ambient air temperature. At an ambient air temperature of 40 ºC in Fig. 8.2, the conventional system exploits free cooling at heat loads lower than 70 W. At a lower ambient air temperature of 30 ºC, free cooling is permissible for heat loads as high as nearly 160 W. This ability to visualize the heat loads and ambient temperatures at which free cooling is permissible is a useful feature of Fig. 8.2. The implications of free cooling have already been addressed however. This section will focus instead upon cost savings at higher heat loads and ambient temperatures where free cooling is unavailable.

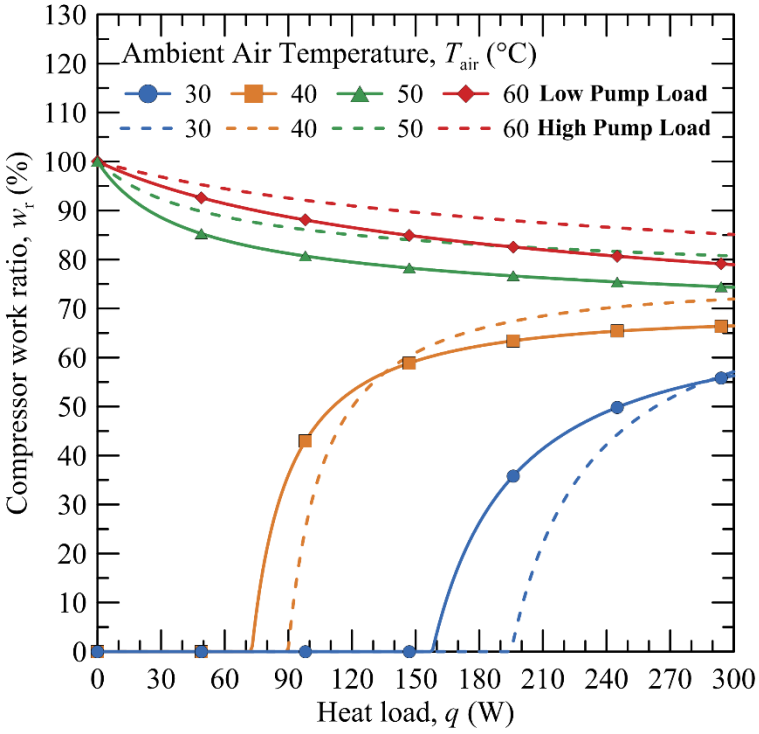

Fig. 8.2 – The compressor load required for dissipating heat from a conventional water cooling system relative to the proposed system, T_w = 60 ºC

Ignoring the dashed lines in Fig. 8.2 and focusing upon the low pump load scenario for now, it is easily observed that at higher ambient air temperatures, the cost savings associated with a conventional water cooling system are less significant. At a heat load of 300 W, a rise in the ambient air temperature from 30 to 60 ºC raises the compressor work ratio from roughly 55 to 80 %; thus reducing cost savings from roughly 45 to 20 %. The system inlet temperatures at this heat load are 18 ºC for the proposed system and 28.5 ºC for a conventional system. The significance here for a thermal engineer is that the additional cost of operating a thermal contact liquid cooling system is not problematic if the ambient air temperature greatly exceeds the system inlet temperature. At higher ambient temperatures of 50 and 60 ºC, the compressor work ratio ranges from 70 to 100 % for all the heat loads shown. This range translates to maximum cost savings of only 30 % while using a conventional water cooling system. Therefore, depending upon the strictness of reliability constraints and the intolerance for leakage risks, a thermal contact cooling system would be a practical and cost effective thermal management solution even in warmer regions.

Under the high pump load scenario, which is represented by the dashed curves in Fig. 8.2, the only observable difference is that the compressor work ratio at higher heat loads increased. At an ambient air temperature of 50 ºC and a heat load of 300 W, switching from a low pump load to a high pump load scenario increases the compressor work ratio from 75 to 80 %. The reason behind this outcome is that an increase in the pump load reduces the difference in the required inlet temperatures of the two systems. At a heat load of 300 W and an allowable wall temperature of 85 ºC, transitioning from a low pump load to a high one reduced this difference from 10.5 to 6.3 ºC. Since the required inlet temperatures of the two systems converge as the pump load increases, so too do their compressor work requirements. The significance here for thermal engineers is that operating a thermal contact liquid cooling system at higher pump loads reduces its relative operating costs for refrigeration.

8.2 Miniature Server Pump

An exemplary miniature centrifugal pump that could be used in conjunction with the proposed thermal contact liquid cooling system is the miniature solar pump (model TL-B10-B) developed by TOPSFLO. The overall dimensions of this pump are 3.90×3.25×1.84

in. (9.9×8.3×4.7 cm). Its height of 1.84 in. (4.7 cm) only slightly exceeds the 1.75 in. (4.4 cm) thickness of a 1U rackmount server; however, the intention here is not to recommend this specific pump for future use. Rather, the aim is to demonstrate that the pressure and flowrate requirements encountered during experimentation can be realistically met with centrifugal pumps of such a small scale.

The pump curve for the highest power configuration of this specific pump model is plotted in Fig. 8.3. At a flowrate of 1.0 gal/min (3.8 L/min), the deliverable head of this pump is 62.4 kPa. Referring back to the experimental results, the overall pressure drop across the heatsink and straight channel TCHx plate was roughly 22.5 kPa (15 kPa across the heatsink and 7.5 kPa across the straight channel TCHx plate). The miniature pump in question is clearly powerful enough to deliver the head and flowrates necessary for the high pump load scenario examined in this study.

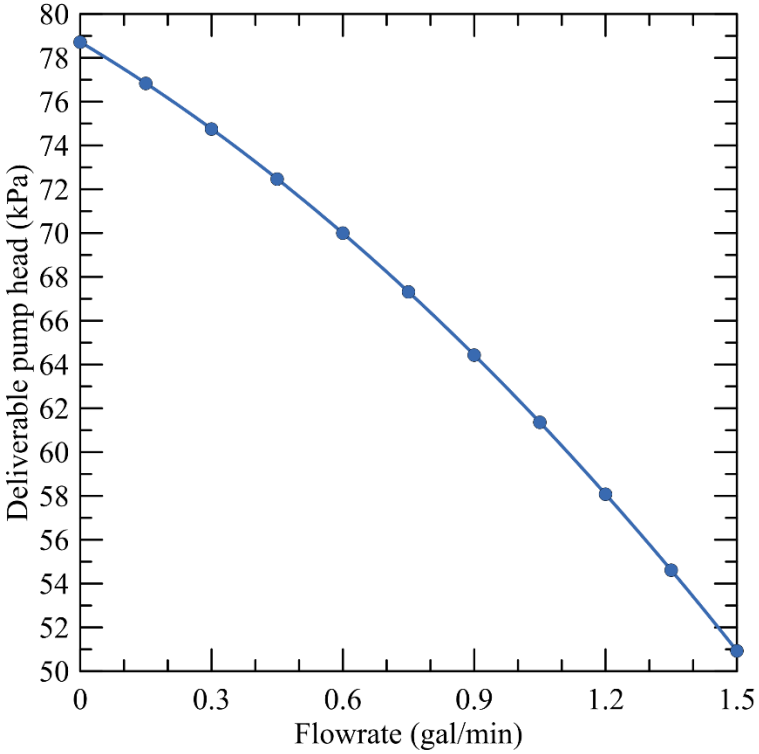

Fig. 8.3 – TOPSFLO TL-B10-B24-1208 miniature centrifugal pump head capacity based on manufacturer datasheets

8.3 Multiple Processors

Similar to most experimental evaluations of liquid cooling systems, this study only examined the characteristics of a cooling system consisting of a single heat source.

However, rackmount servers typically contain up to four general purpose processors (ASHRAE, 2012). this increase in the quantity of processors raises questions about the ideal cooling approach in such scenarios; namely, should the multiple processors be cooled using series or parallel configurations? The differences between these arrangements are illustrated in Fig. 8.4. These diagrams assume that there four processors within a single server and that each processor generates heat at a rate of 150 W. The resulting rate of heat dissipation through the TCHx plate q_{server} must therefore be four times larger at 600 W. Moreover, server pumps have not been included in the figure; they would exist in both systems nonetheless.

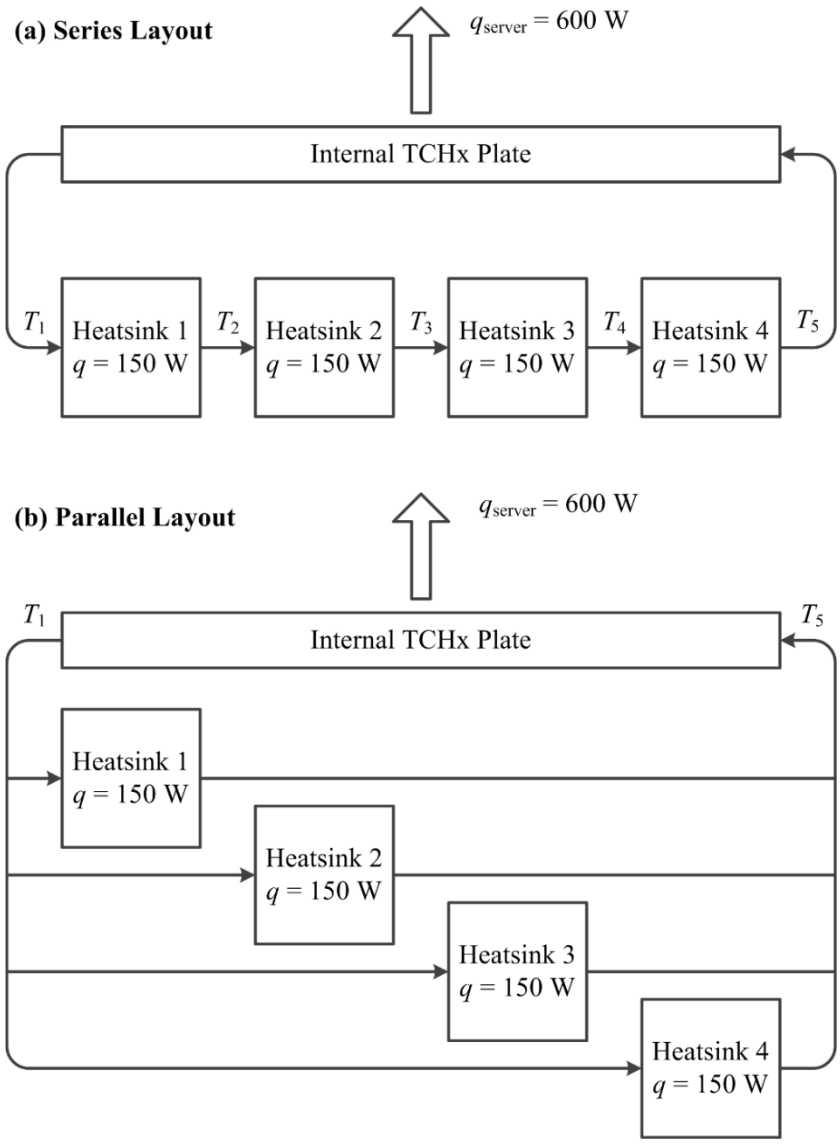

Fig. 8.4 – Four processor liquid cooled in (a) series and (b) parallel

In the series configuration, a single stream of water flows through all four heatsinks. In the parallel configuration, the main stream of water is broken up into four separate streams. Each stream extracts heat from a single processor and heatsink assembly prior to congregating with the remaining streams. The primary advantages of the series configuration over the parallel are that the series configuration requires less material (tubing and fittings) and is more easily tailored to a specific server layout. However, a more thorough comparison requires investigating the effects of the cooling system configuration upon flow and heat transfer characteristics.

8.3.1 Effects of System Configuration on Flow Characteristics

In the case of a series configuration, the flowrate through the system remains unchanged while the pressure drop across the system increases. This increase in pressure losses is simply due to the cumulative drop in pressure across each subsequent heatsink as well as across the TCHx plate. In the case of the parallel configuration, both the pressure drop across the system and the flowrate through the system increase. An example is required to explain this outcome.

Assuming that a flowrate of 0.3 gal/min (1.1 L/min) is necessary through each heatsink for adequate cooling, the flowrate through each parallel stream in the parallel configuration must be equal to 0.3 gal/min (1.1 L/min). Consequently, the flowrate through the TCHx plate in the parallel configuration quadruples to 1.2 gal/min (4.5 L/min). The pressure drop across the entire system is therefore the sum of the pressure drop across a single heatsink at a flowrate of 0.3 gal/min (1.1 L/min) and the pressure drop across the TCHx plate at a flowrate of 1.2 gal/min (4.5 L/min). The experimentally measured pressures losses at these conditions are 2.5 kPa across the heatsink at 0.3 gal/min (1.1 L/min) and 10 kPa across the straight channel TCHx plate at 1.2 gal/min (4.5 L/min). The resulting total pressure drop across the example system with a parallel configuration is 12.5 kPa. The pressure losses across the four heatsinks do not cumulate as their streams are in parallel with one another. Furthermore, this calculation does not consider pressure losses across the manifold through which the main stream is split.

A similar calculation may be repeated for the series configuration. However, since the flowrate through the TCHx plate remains unchanged in the series layout, the pressure drop across the straight channel TCHx plate is only 1.2 kPa at 0.3 gal/min (1.1 L/min). In

the current case, the pressure drop across the entire system is equal to the pressure drop across the TCHx plate added to the cumulative sum of the pressure losses across each of the four heatsinks. The resulting total pressure drop across the example system with a series configuration is 11.25 kPa. Therefore, the total pressure drop of the series configuration is actually 10 % smaller than that across the parallel configuration.

In this regard alone, the series configuration is preferable and this may explain why companies developing water cooling systems for data centers (companies such as Asetek and CoolIT Systems) employ series configurations. Namely, it is easier to manage larger pressure losses across individual components than to amplify flowrates throughout the entire system. In order to overcome the increased pressure losses across individual components, these companies integrate miniature centrifugal pumps into each heatsink. As a result, the pumping capacity of their cooling systems increase in tandem with rising pumping requirements.

8.3.2 Effects of System Configuration on Thermal Performance

One of the advantages of having established thermal resistance values for each individual component is that more complex systems involving multiple processors and heatsinks may now be easily analyzed. Preserving the example from the previous section (in which a flowrate of 0.3 gal/min or 1.1 L/min was assumed across each heatsink), the aim of the current section is to calculate and compare the system inlet temperatures required by the series and parallel cooling system configurations. Additional assumptions include a maximum allowable processor die temperature of 85 ºC and an individual general purpose processor heat load of 150 W.

One disadvantage of the series configuration is that the fluid temperature rises across each subsequent heatsink. Therefore, the inlet temperature of the fourth heatsink (denoted as T_4 in Fig. 8.4) is noticeably larger than the inlet temperatures T_1, T_2, and T_3 of each preceding heatsink. Accordingly, it is the fourth heatsink that limits how warm the circulating fluid may be. At an internal flowrate Q_{int} of 0.3 gal/min (1.1 L/min), the heatsink thermal resistance R_{hs} is 0.105 K/W. The resulting value of T_4 necessary to maintain the fourth processor die temperatures T_{w} at 85 ºC with a heat load q of 150 W is calculated as follows:

$$T_4 = T_{\text{w}} - qR_{\text{hs}} \tag{8.7}$$

This expression yields a value for T_4 of 69.3 ºC. By means of energy balances, the inlet temperatures of the preceding heatsinks are calculated as follows:

$$T_3 = T_4 - \frac{q}{\rho Q_{\text{int}} c_{\text{p}}} \tag{8.8}$$

$$T_2 = T_3 - \frac{q}{\rho Q_{\text{int}} c_{\text{p}}} \tag{8.9}$$

$$T_1 = T_2 - \frac{q}{\rho Q_{\text{int}} c_{\text{p}}} \tag{8.10}$$

The resulting inlet temperatures are 67.4 ºC for the third heatsink, 65.5 ºC for the second, and 63.6 ºC for the first. Therefore, the inlet temperature of the first heatsink must be 5.7 ºC lower than that of the fourth and final heatsink.

Although these successive temperature drops are an interesting quality of the series configuration, they are not pertinent to calculating the required system inlet temperature. The temperature necessary for doing so is the inlet temperature of the internal TCHx plate T_5. Through an energy balance across the fourth heatsink, T_5 is calculated as follows:

$$T_5 = T_4 + \frac{q}{\rho Q_{\text{int}} c_{\text{p}}} \tag{8.11}$$

This equation results in a value of T_5 of 71.1 ºC. At an internal flowrate of 0.3 gal/min (1.1 L/min) and an external flowrate of 1.0 gal/min (3.8 L/min), the thermal resistance of the straight channel TCHx R_{TCHx} is 0.038 K/W. In order to dissipate a total of 600 W from the server, the required inlet temperature of the external TCHx plate (which is analogous to the system inlet temperature) is calculated as follows:

$$T_{\text{in,ext}} = T_{\text{in,int}} - qR_{\text{TCHx}} \tag{8.12}$$

Consequently, the necessary system inlet temperature while employing a series configuration is 48.3 ºC.

Repeating these calculations for the parallel configuration yields an inlet temperature for all heatsinks T_1 equal to 69.3 ºC and an inlet temperature of the internal TCHx plate T_5 again equal to 71.1 ºC. The temperatures T_2, T_3, and T_4 are irrelevant in the parallel configuration as they all match T_1. The difference in thermal performance between the series and parallel configurations stems from the fact that the flowrate through the TCHx plate is four times larger in the parallel configuration. At an internal flowrate of 1.2 gal/min (4.5 L/min) and an external flowrate of 1.0 gal/min (3.8 L/min), the thermal resistance of the straight channel TCHx is 0.024 K/W. In order to dissipate a total of 600 W from the

server, the system inlet temperature must now be 56.8 ºC. All calculated fluid temperatures for the two configurations are listed in Table 8.1.

Table 8.1 – Fluid temperatures at various locations for series and parallel cooling system configurations, q = 150 W per processor, 4 processors, T_w = 85 ºC, Q_{int} = 0.3 gal/min through heatsinks, Q_{ext} = 1.0 gal/min

Temperature	Series config. (ºC)	Parallel config. (ºC)
T_1	63.6	69.3
T_2	65.5	-
T_3	67.4	-
T_4	69.3	-
T_5	71.1	71.1
$T_{in,ext}$	48.3	56.8

The parallel configuration requires a system inlet temperature that is 8.5 ºC higher than that of the series configuration due to the fact that the flowrate through the straight channel TCHx is greater when employing a parallel configuration. A greater flowrate, in turn, lowers thermal resistances. This temperature difference resembles those observed between a conventional water cooling system and a thermal contact water cooling system at a heat load of 300 W (6.3 ºC at high pump loads and 10.5 ºC at low pump loads). Consequently, the conclusions inferred from the cost savings analysis shown in Fig. 8.2 may be extended to the current discussion.

Using a parallel instead of a series configuration could yield cost savings as high as 30 % when ambient temperatures are sufficiently high and free cooling is unavailable. In this regard, the only recommendation to be made is that a parallel configuration is the preferred design choice for cooling multiple processors provided that design and installation of such a system is not problematic or costly.

8.4 Integration within Server Racks

The objective of this final section is to briefly recommend methods of integrating a thermal contact liquid cooling system within existing server racks. Coupling mechanisms for forcing the internal and external TCHx plates into contact are not discussed. Examples of such mechanisms are prevalent among the patents reviewed for this thesis and there little novel information that could be presented in that regard. Moreover, the ideal coupling

mechanism design depends upon the specific geometric properties of electronic enclosures. Rather, this section focuses upon a more general strategy of integration that may potentially deliver further cost savings.

One method of improving the efficiency of traditional air cooling systems is to equip server racks with air-water heat exchangers. One approach involves attaching such heat exchangers to the rear door of a server; these are termed rear door heat exchangers (RDHx) (Grimshaw et al., 2011). In this case, cold facility air is driven through individual servers by cooling fans. As usual, this air stream extracts heat generated by electronic components; however, prior to re-entering the facility, the heated air is driven through an air-water heat exchanger located along the rear server door. At this stage, heated air is water cooled immediately upon leaving the server. No additional power is consumed by first transporting the air to the computer room air conditioning (CRAC) unit. This approach to air cooling has been shown to yield cost savings between 30 and 40 % (Grimshaw et al., 2011).

Another approach involves enclosing the entire server rack within a sealed chamber inside which air recirculates. Heated air leaving servers passes through an air-water heat exchanger located along the side of the rack; this components is referred to as a side car heat exchanger (SCHx) (Gao et al., 2015). This design adds the benefit of shielding the recirculating air from the external environment; which can be advantageous in corrosive or contaminated military environments. Given the similarities between their heat transfer mechanisms, air cooling systems employing RDHx or SCHx subsystems can safely be assumed to offer comparable thermal performances.

Regardless of which design is preferable, it is recommended that thermal contact liquid cooling systems be commissioned in conjunction with such air-water heat exchangers. One major benefit that would result from the union of these technologies is cost savings due to the use of warmer recirculating air. Since the thermal contact liquid system manages heat dissipation from the most problematic and concentrated sources of heat (central processing units), only the remaining low heat flux components would require air cooling. As a result, the cooling load incurred by the air cooling system would diminish. This reduction in air cooling loads permits the use of warmer recirculating air which would, in turn, be cooled by warmer water circulating through the air-water heat exchangers.

An example configuration for integrating a thermal contact liquid cooling system with a side car heat exchanger is shown in Fig. 8.5. In this case, the side car heat exchanger and the external TCHx plate have been combined into a single assembly. Cold facility water first enters the side car heat exchanger rather than the external TCHx plate as air temperatures are likely to be lower than water temperatures within the server loop. This assertion is speculated based on the poor thermophysical properties of air relative to those of water. Upon cooling the recirculating air, slightly warmer facility water is delivered to the external TCHx plate through which heat is extracted from the server's internal flow loop. Upon exiting the external TCHx plate, the heated facility water is returned to the facility level heat exchanger which dissipates all generated heat to the external ambient environment.

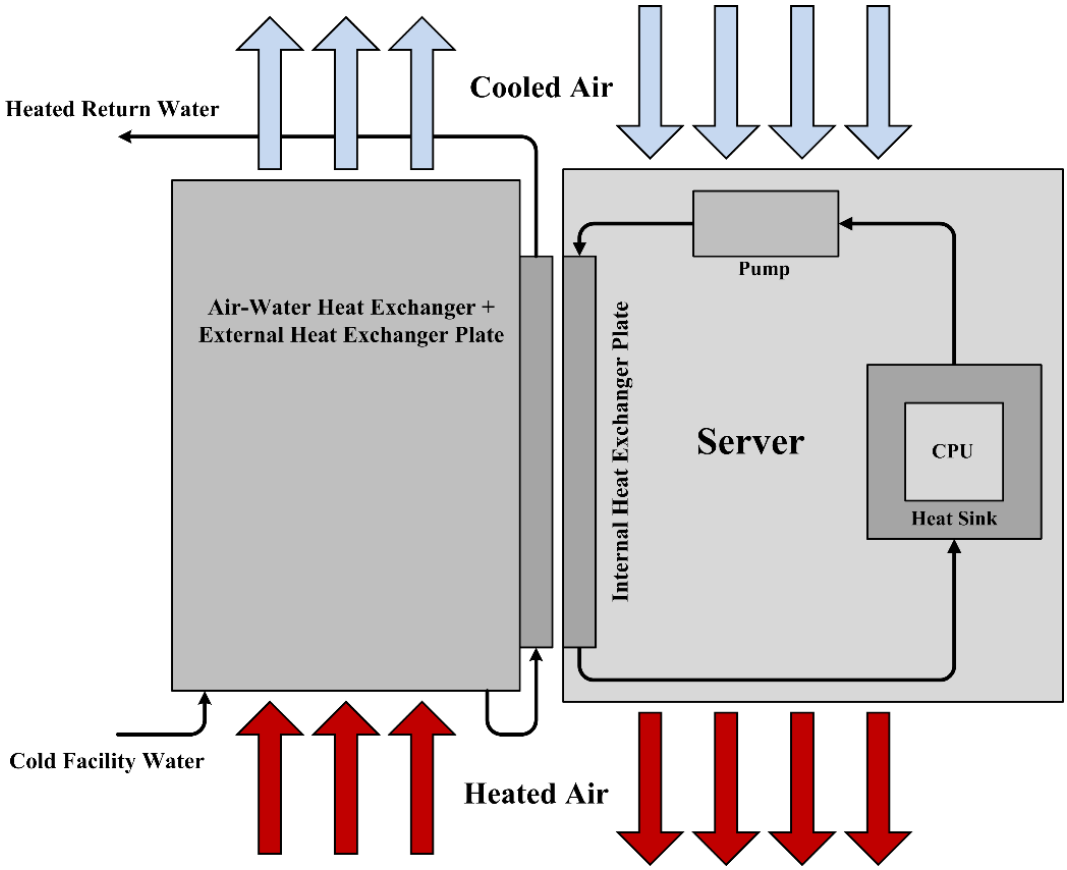

Fig. 8.5 – Schematic of a server cooled using a thermal contact heat exchanger in conjunction with a side car heat exchanger (SCHx)

Unfortunately, predicting the thermal performance of such a system is beyond the scope and capacity of this work. The thermal resistance of the heatsink and thermal contact

heat exchanger are certainly crucial for performing such an analysis; however, so are the intricate geometric and thermal properties of the remaining low heat flux server components that require air cooling. The performance of such a system may only be properly characterize by means of an experimental setup consisting of an operational server in which processors are liquid cooling while remaining components are air cooled. Given the cost savings individually attributed to a thermal contact liquid cooling system and a side car heat exchanger, however, the advantages in combining these technologies are nonetheless evident.

8.5 Concluding Remarks

Presented in this chapter was an attempt to quantify the cost savings associated with a conventional water cooling system relative to the proposed thermal contact liquid cooling system. Three possible scenarios were discussed. The first was a scenario is which both conventional and proposed systems were free cooled. The second described a narrow range of ambient temperatures over which the conventional system would be free cooled while the proposed system would not. The third involved sufficiently high ambient temperatures such that neither system would be free cooled. In this latter case, the cost of operating a conventional cooling system was estimated to be as much as 30 % less than the cost of operating the proposed system. This calculation was based upon calculations of compressor loads within vapor-compression refrigeration cycles.

A discussion concerning the pumping capacity of miniature centrifugal pumps was also presented. The performance of a miniature 24 V solar pump developed by TOPSFLO was examined and it was established that this pump is capable of delivering the head and flowrate necessary for operating the proposed cooling system. At a flowrate of 1.0 gal/min (3.8 L/min) – which corresponds to the high pump load scenario described in this study – the miniature pump in question delivers a head capacity of 62.4 kPa. This substantially exceeds the 22.5 kPa pressure drop across the proposed system at a high pump load and leaves ample room for pressure losses across piping and other manifolds.

Next, the benefits and drawbacks of series versus parallel cooling system configurations were examined in the context of servers containing multiple processors. It was shown that system pressure losses roughly 10 % lower when employing a series configuration. However, the overall thermal performance of the system was substantially

improved when employing a parallel configuration. Specifically, the required system inlet temperature was reduced by 8.5 ºC when transitioning from a series configuration to a parallel configuration while heat was generated at a rate of 600 W across a total of four processors. In this regard, the parallel configuration was deemed preferable for thermal contact cooling systems.

Finally, recommendations were made concerning the integration of the proposed thermal contact liquid cooling system within existing server racks. It was suggested that the design be implemented in conjunction with existing rack-level air-water heat exchangers that have been proven to reduce the cost of air cooling. Although, further experimentation is necessary to quantify the cost savings associated with integrating these technologies.

Chapter 9 - Conclusion

This final chapter revisits the major findings expressed throughout this thesis and relates them to the main project objectives laid out in the introductory chapter. Subsequently, final recommendations are made in regards to industry implementation and future research.

9.1 Conclusions of conducted Research

As laid out in the introduction of this thesis, the first objective of this project was to identify a cooling strategy ideal for military applications. After an extensive review of available cooling technologies, the recommended cooling solution was a thermal contact liquid cooling system. This system eliminated the leakage risks present in conventional water cooling systems by replacing their fluidic connectors with a thermal contact heat exchanger. The added drawback was supplemental heat transfer interfaces which served to increase the overall thermal resistance of the system. A review of available patents filed within the past 15 years indicated that members of industry have expressed interest in such a cooling system design. Although, no experimental evaluation of a thermal contact liquid cooling system has been discovered by the authors.

In order to ascertain the influence of the thermal contact heat exchanger upon the system thermal resistance, the second and third objectives were to design specific embodiments of the proposed cooling system and to then experimentally and numerically evaluate their thermal performances. These embodiments comprised the straight channel, serpentine, and mixed plate heat exchangers. A numerical unit cell model was presented and utilized for designing and optimizing a heatsink and the straight channel TCHx plate for experimentation. This numerical model was validated against experimental results and was found to be accurate to within 14.5 %. Based on the numerical results, the heatsink channel width and height were set to 0.5 and 2.3 mm, respectively, while the straight channel TCHx plate channel width and height were set to 1 and 4 mm, respectively. These dimensions were necessary for maintaining the heat source temperature below the allowable 85 ºC limit while dissipating heat at a rate of 300 W.

The process of experimentation revealed that of the three suggested embodiments, the straight channel TCHx plate design was most preferable due to its reduced pressure

losses and comparable thermal performance relative to those of the remaining designs. Specifically, the straight channel TCHx plate required a pump load of 0.34 W in order to deliver a flowrate of 0.9 gal/min (3.4 L/min) and maintain the maximum wall temperature at 68 ºC under a heat load of 330.4 W. Under the same heat load, the serpentine TCHx plate required a 2.7 W pump load (which is roughly an order of magnitude greater than 0.34 W) in order to deliver a flowrate of 0.7 gal/min (2.6 L/min) and maintain the maximum wall temperature at 68 ºC. The mixed TCHx plate design was intermediary with regards to both pressure losses and thermal performance.

Based upon thermal resistances calculated from experimental results, it was revealed that the proposed thermal contact liquid cooling system requires inlet water temperatures that are 10.5 and 6.3 ºC lower than those required by a conventional water cooling system at low and high pump loads, respectively, and a heat load of 300 W. That is to say, a conventional water cooling system requires inlet water at 53.5 and 59.9 ºC while operating at low and high pump loads; while the proposed system requires inlet water at 43 and 53.2 ºC under the same circumstances. These temperatures differences yielded estimated cost savings of up to 30 % when operating a conventional water cooling system instead of the proposed system under warm ambient conditions.

The final objective of this project was to recommend methods of industry implementation. In this regard, it was suggested that the proposed thermal contact liquid cooling be integrated with existing air-water rack heat exchanger technology that has been proven to reduce the operating costs of air cooling systems. Examples of such air-water heat exchangers include rear door heat exchangers (RDHx) and side car heat exchangers (SCHx). Furthermore, a parallel cooling system configuration was recommended for server containing multiple processors. It was shown that, relative to a series configuration, the required system inlet temperature could be reduced by an additional 8.5 ºC when employing a parallel configuration.

9.2 Recommendations and Future Work

Based on the work presented in this thesis, the proposed thermal contact liquid cooling system is recommended for used in military applications. Its heat transfer performance is comparable to that of a conventional water cooling system and its closed loop liquid cooling design mitigates issues pertaining to coolant leakage and contaminant

infiltration while hot swapping components. As a result, it delivers the enhanced reliability characteristics sought by Raytheon Canada. Meanwhile, the additional costs of operating such a system in lieu of a conventional water cooling system are moderate enough to be deemed a fit trade-off.

Should such a thermal contact liquid cooling system be developed for industrial applications, thermal engineers should bear in mind certain considerations. First, a straight channel heat exchanger plate would be the ideal choice among the designs tested for the thermal contact heat exchanger plates. This conclusion stems from the fact that its pressure losses remain moderate even at higher flowrates while its thermal performance is on par with those of the serpentine and mixed channel heat exchanger plates.

Second, the thermal contact heat exchanger plates should be longer than those experimented with in this study. The size of the plates tested in the current work was limited by the coverage area of the CNC machine employed. An industrial product may extend the heat exchanger plate lengths threefold based on the size of standard rackmount servers. This extension would substantially reduce the thermal resistance of the thermal contact heat exchanger. On a side note, an additional benefit of the straight channel heat exchanger plate is that numerically modelling the impact of length changes would be an effortless task.

Third, alternative manufacturing methods should be employed in order increase the height of both the heatsink and heat exchanger plate channels. Miniature mill bits are limited to at most a one-to-four diameter-to-height ratio whereas greater channel heights would be possible through the use of, for instance, slitting saws. Increasing the height of heatsink and heat exchanger channels would dramatically reduce pressure losses across these components while at the same time increasing their convective heat transfer areas (which would in turn further reduce thermal resistances).

Fourth, the thermal contact liquid cooling system should be setup in a parallel configuration within servers consisting of multiple processors. A comparison of the heat transfer characteristics of series and parallel configurations has shown the latter configuration to require larger inlet temperatures for adequate thermal management. Warmer fluid, in turn, reduces vapor-compression refrigeration cooling costs. In order to overcome the additional pressure losses engendered within multi-processor system, it is

recommended that the common approach of integrating miniature pumps within each heatsink be practiced. This approach will ensure adequate pumping capacity in all cases.

Finally, liquid cooling processors (which are the most concentrated sources of heat within servers) reduces the cooling load incurred by the air cooling system which is tasked with cooling the remaining low heat flux server components. This reduction in the air cooling load authorizes the use of higher temperature air which, in turn, facilitates the process of cooling the circulating air using air-water heat exchangers. Combining the thermal contact liquid cooling system with an air-water heat exchanger embedded within a server rack would potentially yield a fully water cooled system. The key advantage here would be the elimination of costly computer room air conditioning units from the cooling process.

In this regard, it is recommended that future studies be undertaken to examine the performance of such an integrated system. The primary aim of such work would be to assess whether sufficiently warm air will adequately cool low heat flux server electronics; thus permitting high temperature water cooling of the air itself. More importantly, these studies should estimate the cost savings associated with such a cooling system and assess whether the additional capital expenses of embedding air-water heat exchangers within server racks are appropriate.

References

Ali, A. F., & El-Genk, M. S. (2012). Effect of inclination on saturation boiling of PF-5060 dielectric liquid on 80- and 137-μm thick copper micro-porous surfaces. *International Journal of Thermal Sciences, 53*, 42-48.

Asadi, M., Xie, G., & Sunden, B. (2014). A review of heat transfer and pressure drop characteristics of single and two-phase microchannels. *International Journal of Heat and Mass Transfer, 79*, 34-53.

ASHRAE. (2012). *Datacom equipment power trends and cooling applications* (Second ed.): American Society of Heating, Refrigerating and Air-Conditioning Engineers, Inc.

Bear, D. B. (2004). United States Patent No. US 6796372 B2.

Belady, C., & Womack, C. (2004). United States Patent No. US 6829142 B2. H.-P. D. Company.

Branton, S. B. (2014). United States Patent No. US 8749968 B1. A. A/S.

Brewer, R. G., Chow, L. C., & Hom, J. (2010). United States Patent No. US 7715194 B2.

Brown, T. G. (2003). *Harsh military environments and microelectromechanical (MEMS) devices*. Paper presented at the IEEE.

Campbell, L. A., Chu, R. C., Ellsworth, M. J., Iyengar, M., & Simons, R. E. (2012). United States Patent No. US 8094453.

Carbó, A., Oró, E., Salom, J., Canuto, M., Macías, M., & Guitart, J. (2016). Experimental and numerical analysis for potential heat reuse in liquid cooled data centres. *Energy Conversion and Management, 112*, 135-145.

Chu, R. C., Ellsworth, M. J., Schmidt, R., & Simons, R. E. (2006). United States Patent No. US 7012807 B2. I. B. M. Corporation.

Ebrahimi, K., Jones, G. F., & Fleischer, A. S. (2014). A review of data center cooling technology, operating conditions and the corresponding low-grade waste heat recovery opportunities. *Renewable and Sustainable Energy Reviews, 31*, 622-638.

Fakhim, B., Behnia, M., Armfield, S. W., & Srinarayana, N. (2011). Cooling solutions in an operational data centre: A case study. *Applied Thermal Engineering, 31*(14-15), 2279-2291.

Fried, S. (2011). United States Patent No. US 7959132 B2.

Gao, T., David, M., Geer, J., Schmidt, R., & Sammakia, B. (2015). Experimental and numerical dynamic investigation of an energy efficient liquid cooled chiller-less data center test facility. *Energy and Buildings, 91*, 83-96.

Garimella, S. V., Yeh, L.-T., & Persoons, T. (2012). Thermal management challenges in telecommunication systems and data centers. *IEEE Transactions on Components, Packaging and Manufacturing Technology, 2*(8), 1307-1316.

Garner, S. D. (2003). United States Patent No. US 6657121 B2.

Geisler, K. J. L., & Straznicky, I. (2004). *Immersion cooling module for military COTS applications*. Paper presented at the International Society Conference on Thermal Phenomena.

Geng, H. (2015). *Data center handbook*. New Jersey: John Wiley & Sons, Inc.

Goth, G. F. (2012). An Overview of the IBM Power 775 Supercomputer Water Cooling System. *Journal of Electronic Packaging, 134*(2), 020906.

Grimshaw, J., McSweeney, M., Novotny, S., & Gagnon, M. (2011). *Data center rack level cooling utilizing water-cooled, passive rear door heat exchangers (RDHx) as a cost effective alternative to CRAH air cooling*: Coolcentric.

Hom, J., Brewer, R. G., & Choi, H. (2009). United States Patent No. US 2009/0225515.

IAPWS. (2007). *Revised release on the IAPWS industrial formulation 1997 for the thermodynamic properties of water and steam*. Lucerne, Switzerland: The International Association for the Properties of Water and Steam.

Ishimine, J. (2008). United States Patent No. US 2008/0068793.

Johnston, A., Stone, D., & Cader, T. (2008). *SprayCool command post platform for harsh military environments*. Paper presented at the Twenty-fourth Annual IEEE Semiconductor Thermal Measurement and Management Symposium.

Kadam, S. T., & Kumar, R. (2014). Twenty first century cooling solution: Microchannel heat sinks. *International Journal of Thermal Sciences, 85*, 73-92.

Kant, K. (2009). Data center evolution. *Computer Networks, 53*(17), 2939-2965.

Kheirabadi, A. C., & Groulx, D. (2016a). *A comparison of numerical strategies for optimal liquid cooled heat sink design.* Paper presented at the Proceedings of the ASME 2016 Summer Heat Transfer Conference, Washington, DC, USA.

Kheirabadi, A. C., & Groulx, D. (2016b). Cooling of server electronics: A design review of existing technology. *Applied Thermal Engineering, 105*, 622-638.

Koenen, D. (2002). United States Patent No. US 6349035 B1.

Kondo, Y., Ohashi, S., Minamitani, R., Naganawa, T., Yoshitomi, Y., Nakanishi, M., et al. (2004). United States Patent No. US 6807056 B2.

Konshak, M. (2007). United States Patent No. US 2007/0297123 A1. S. Microsystems.

Koo, J., & Kleinstreuer, C. (2004). Viscous dissipation effects in microtubes and microchannels. *International Journal of Heat and Mass Transfer, 47*(14-16), 3159-3169.

Ku, J. (1999). *Operating characteristics of loop heat pipes*. Paper presented at the 29th International Conference on Environmental Systems.

Martin, J. K., McMaster, M., Chow, N., Conway, B. R., Brewer, R. G., Upadhya, G., et al. (2010). United States Patent No. US 2010/0085708.

Maydanik, Y. F., Chernysheva, M. A., & Pastukhov, V. G. (2014). Review: Loop heat pipes with flat evaporators. *Applied Thermal Engineering, 67*(1-2), 294-307.

McCoy, S. (2009). United States Patent No. US 2009/0027856.

McGlen, R. J., Jachuck, R., & Lin, S. (2004). Integrated thermal management techniques for high power electronic devices. *Applied Thermal Engineering, 24*(8-9), 1143-1156.

Memory, S., Ganaway, F., Rogers, C., DeVuono, A., Phillips, A. L., & Zuo, Z. (2004). United States Patent No. US 6828675 B2.

Morini, G. L. (2005). Viscous heating in liquid flows in micro-channels. *International Journal of Heat and Mass Transfer, 48*(17), 3637-3647.

Pflueger, J. C. (2008). United States Patent No.

Phillips, A. L., Khrustalev, D., Wert, K., Wilson, M., Wattelet, J., & Broadbent, J. (2004). United States Patent No. US 6804112 B2.

Qiu, L., Dubey, S., Choo, F. H., & Duan, F. (2015). Recent developments of jet impingement nucleate boiling. *International Journal of Heat and Mass Transfer, 89*, 42-58.

Shabgard, H., Allen, M. J., Sharifi, N., Benn, S. P., Faghri, A., & Bergman, T. L. (2015). Heat pipe heat exchangers and heat sinks: Opportunities, challenges, applications, analysis, and state of the art. *International Journal of Heat and Mass Transfer, 89*, 138-158.

Siedel, B., Sartre, V., & Lefèvre, F. (2015). Literature review: Steady-state modelling of loop heat pipes. *Applied Thermal Engineering, 75*, 709-723.

Sonntag, R. E., Borgnakke, C., & Van Wylen, G. J. (2003). *Fundamentals of thermodynamics*. New York: John Wiley & Sons.

Spearing, I., & Schrader, T. (2012). United States Patent No. US 8289710 B2. L. Corporation.

Suhir, E. (2013). Could electronics reliability be predicted, quantified and assured? *Microelectronics Reliability, 53*(7), 925-936.

Tuma, P. E. (2010). *The merits of open bath immersion cooling of datacom equipment*. Paper presented at the 26th Annual IEEE Semiconductor Thermal Measurement and Management Symposium.

Tuma, P. E. (2011). *Design considerations relating to non-thermal aspects of passive 2-phase immersion cooling*. Paper presented at the 27th Annual IEEE Semiconductor Thermal Measurement and Management Symposium (SEMI-THERM).

Upadhya, G., Munch, M., Chow, N., Tsao, P., Werner, D., McMaster, M., et al. (2009). United States Patent No. US 7599184 B2. C. Inc.

Zhang, H., Shao, S., Xu, H., Zou, H., & Tian, C. (2014). Free cooling of data centers: A review. *Renewable and Sustainable Energy Reviews, 35*, 171-182.

Zimmermann, S., Meijer, I., Tiwari, M. K., Paredes, S., Michel, B., & Poulikakos, D. (2012). Aquasar: A hot water cooled data center with direct energy reuse. *Energy, 43*(1), 237-245.

Zimmermann, S., Tiwari, M. K., Meijer, I., Paredes, S., Michel, B., & Poulikakos, D. (2012). Hot water cooled electronics: Exergy analysis and waste heat reuse feasibility. *International Journal of Heat and Mass Transfer, 55*(23-24), 6391-6399.

Appendix A – Mesh Convergence Plots for Numerical Study

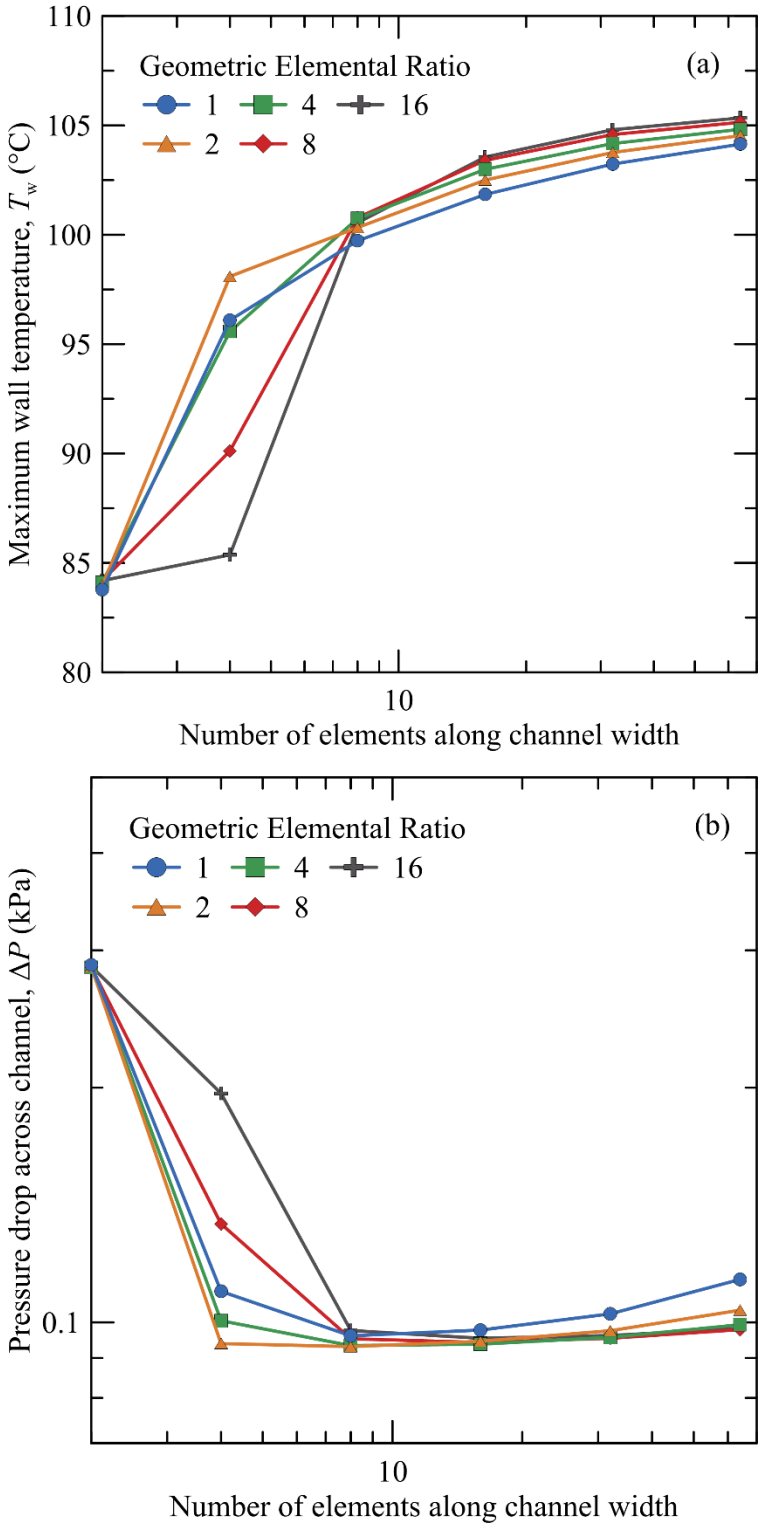

Fig. A.1 – Convergence of geometric distribution ratio, W_{ch} = 1 mm, H_{ch} = 4 mm, L_{ch} = 2 cm, T_{in} = 60 °C, q_{total} = 300 W, Q_{in} = 1 L/min, $R"_{TIM}$ = 0.1 K·cm²/W

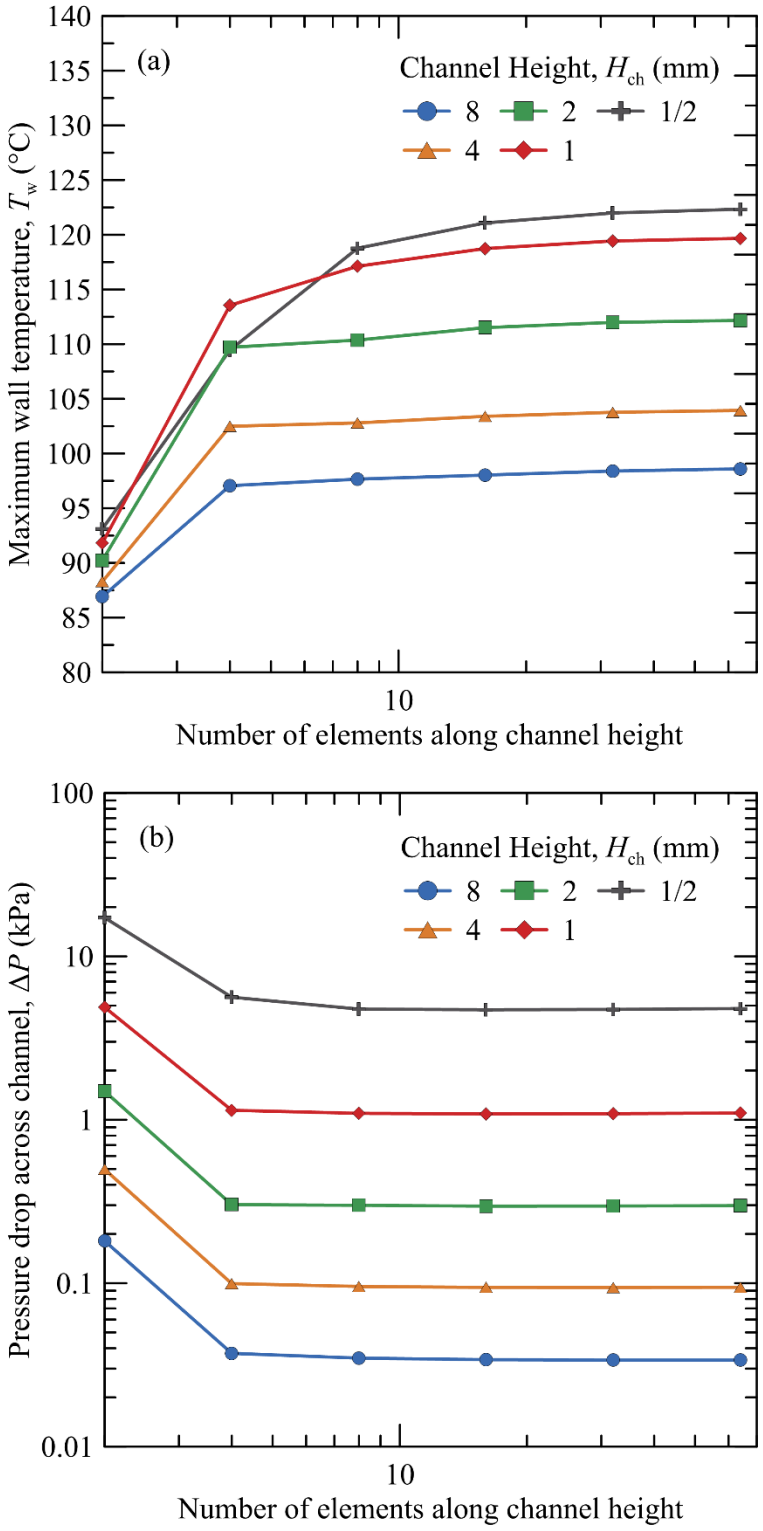

Fig. A.2 – Mesh convergence study along channel height, W_{ch} = 1 mm, L_{ch} = 2 cm, T_{in} = 60 °C, q_{total} = 300 W, Q_{in} = 1 L/min, $R"_{TIM}$ = 0.1 K·cm²/W

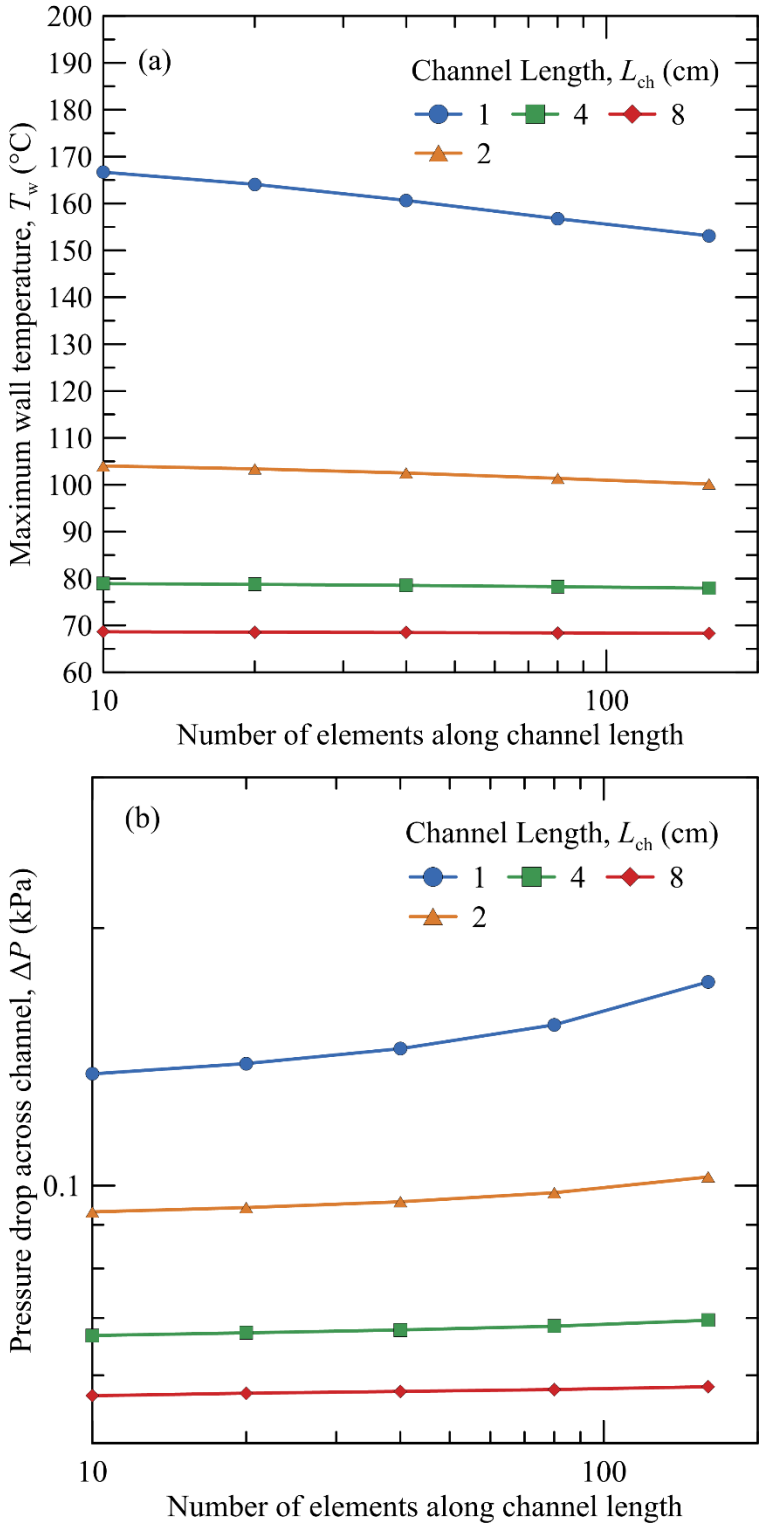

Fig. A.3 – Mesh convergence study along channel length, W_{ch} = 1 mm, H_{ch} = 4 mm, T_{in} = 60 °C, q_{total} = 300 W, Q_{in} = 1 L/min, $R"_{TIM}$ = 0.1 K·cm²/W

Appendix B – Supplemental Experimental Data

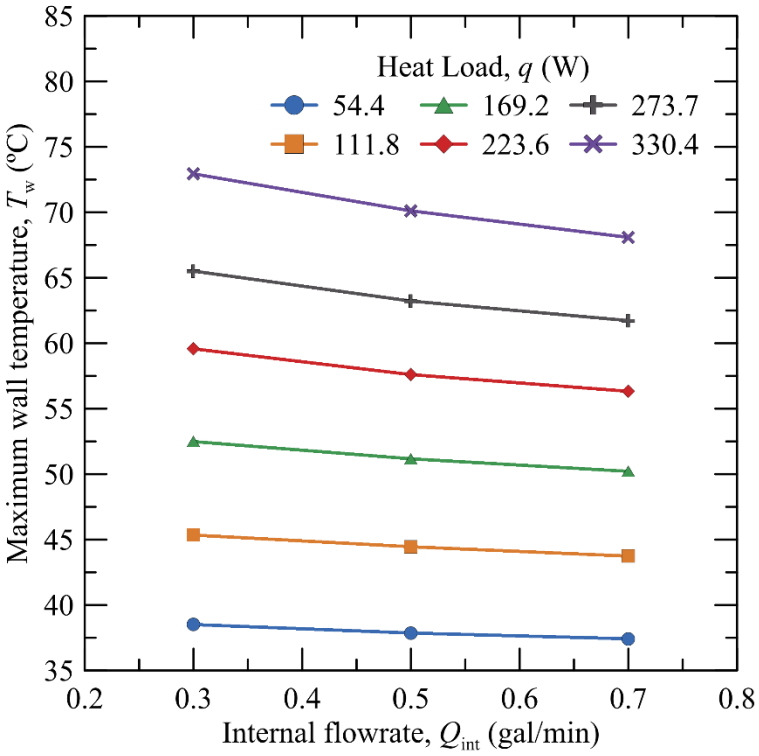

Fig. B.1 – Effect of internal flowrate Q_{int} on maximum wall temperature for various heat loads q, $T_{in,ext}$ = 30 °C, Q_{ext} = 1.0 gal/min, serpentine TCHx

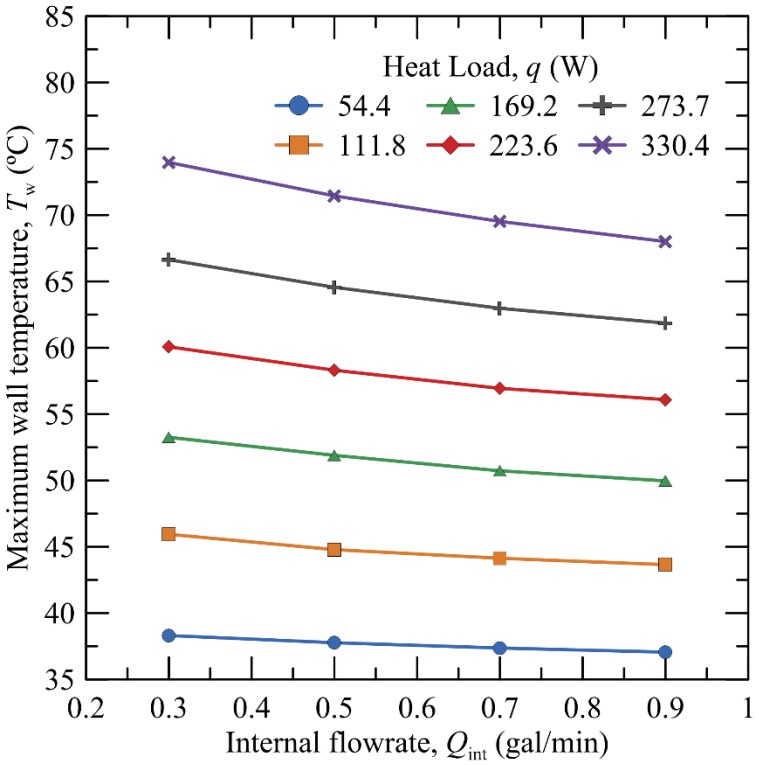

Fig. B.2 – Effect of internal flowrate Q_{int} on maximum wall temperature for various heat loads q, $T_{in,ext}$ = 30 °C, Q_{ext} = 1.0 gal/min, mixed TCHx

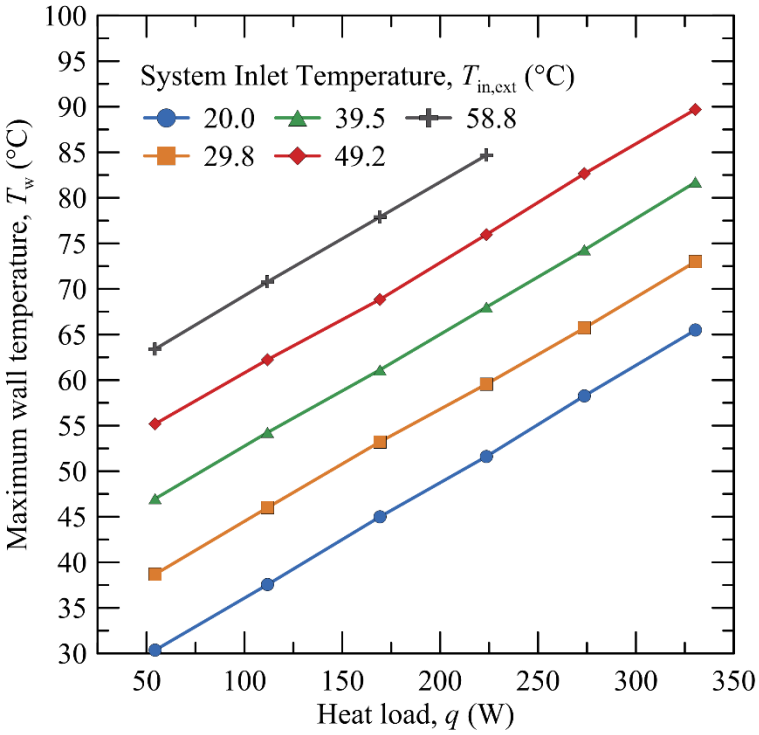

Fig. B.3 – Effect of system inlet temperature $T_{in,ext}$ on the maximum wall temperature T_w at low pump loads, Q_{int} = Q_{ext} = 0.3 gal/min, serpentine TCHx

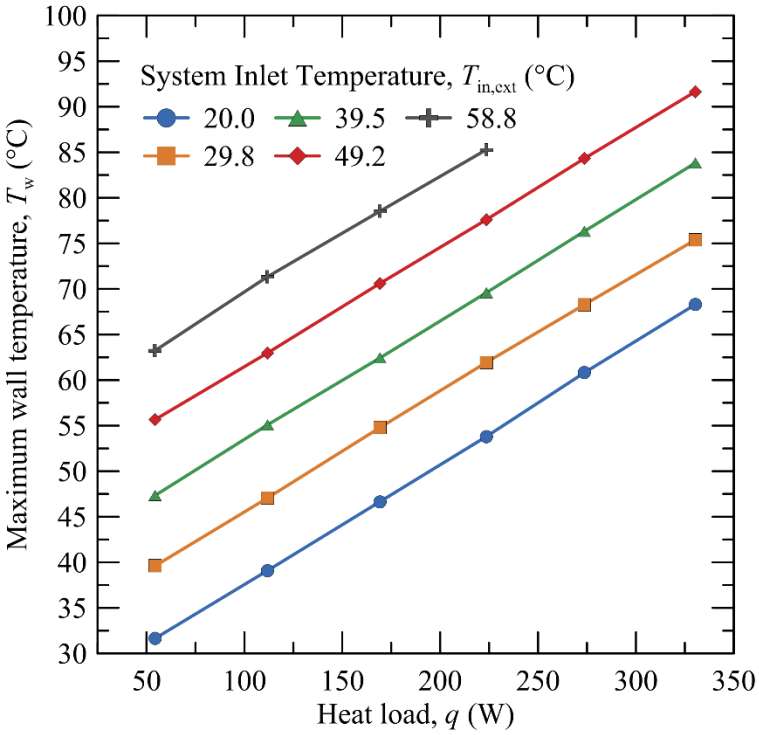

Fig. B.4 – Effect of system inlet temperature $T_{in,ext}$ on the maximum wall temperature T_w at low pump loads, Q_{int} = Q_{ext} = 0.3 gal/min, mixed TCHx

Appendix C – MATLAB Code for Refrigeration Cycle Analysis

```
%% Setup Workspace
clear;
clc;
format short;

%% Identify Parameters
% Solver parameters
n = 3;      % Order of polynomial regressions

% Refrigeration cycle parameters
T_air  = 60;        % Ambient air temperature
R_conv = 0.085;     % Conventional system thermal resistance
R_prop = 0.106;     % Proposed system thermal resistance
q = [0:1:300]';     % Range of heat loads to simulate
T_die = 60;         % Maximum allowable die temperature
delta_T = 10;       % Temperature diff. required for adequate heat
                    % transfer from evaporator and condenser
eff = 0.8;          % Compressor isentropic efficiency

% Resulting cycle temperatures
T_sys_conv = T_die-q*R_conv;
T_sys_prop = T_die-q*R_prop;
T1_conv = T_sys_conv-delta_T;
T1_prop = T_sys_prop-delta_T;
T3      = T_air+delta_T;

% Miscellaneous parameters
N = length(q);

%% Digitization of R134a Properties
% Saturated vapor properties
T     = [0:5:75];
P_sat = [294 350.9 415.8 489.5 572.8 666.3 771.0 887.6 1017.0...
         1160.2 1318.1 1491.6 1681.8 1889.9 2117.0 2364.4];
hg    = [398.36 401.32 404.23 407.07 409.84 412.52 415.08 417.52...
        419.82 421.96 423.91 425.65 427.13 428.30 429.11 429.45];
sg    = [1.7262 1.7239 1.7218 1.7200 1.7183 1.7168 1.7153 1.7139...
        1.7123 1.7106 1.7088 1.7066 1.7040 1.7008 1.6970 1.6923];
p_P_sat = polyfit(T,P_sat,n);
p_hg = polyfit(T,hg,n);
p_sg = polyfit(T,sg,n);

% Superheated vapor properties, P = 1000 kPa
T      = [39.37 40 50 60 70 80 90 100];
h_1MPa = [419.54 420.25 431.24 441.89 452.34 462.7 473.03 483.36];
s_1MPa = [1.7125 1.7148 1.7494 1.7818 1.8127 1.8425 1.8713 1.8994];
p_h_1MPa = polyfit(T,h_1MPa,n);
p_s_1MPa = polyfit(T,s_1MPa,n);

% Superheated vapor properties, P = 1200 kPa
T      = [46.31 50 60 70 80 90 100];
h_12MPa = [422.49 426.84 438.21 449.18 459.92 470.55 481.13];
s_12MPa = [1.7102 1.7237 1.7584 1.7908 1.8217 1.8514 1.8801];
p_h_12MPa = polyfit(T,h_12MPa,n);
p_s_12MPa = polyfit(T,s_12MPa,n);
```

```
% Superheated vapor properties, P = 1400 kPa
T      = [52.42 60 70 80 90 100];
h_14MPa = [424.78 434.08 445.72 456.94 467.93 478.79];
s_14MPa = [1.7077 1.736 1.7704 1.8026 1.8333 1.8628];
p_h_14MPa = polyfit(T,h_14MPa,n);
p_s_14MPa = polyfit(T,s_14MPa,n);

% Superheated vapor properties, P = 1600 kPa
T      = [57.9 60 70 80 90 100];
h_16MPa = [426.54 429.32 441.89 453.72 465.15 476.33];
s_16MPa = [1.7051 1.7135 1.7507 1.7847 1.8166 1.8469];
p_h_16MPa = polyfit(T,h_16MPa,n);
p_s_16MPa = polyfit(T,s_16MPa,n);

% Superheated vapor properties, P = 2000 kPa
T      = [67.48 70 80 90 100 110 120];
h_2MPa = [428.75 432.53 446.30 458.95 471.00 482.69 494.19];
s_2MPa = [1.6991 1.7101 1.7497 1.7850 1.8177 1.8487 1.8783];
p_h_2MPa = polyfit(T,h_2MPa,n);
p_s_2MPa = polyfit(T,s_2MPa,n);

% Superheated vapor properties, P = 3000 kPa
T      = [86.2 90 100 110 120];
h_3MPa = [427.67 436.19 453.73 468.50 482.04];
s_3MPa = [1.6759 1.6995 1.7472 1.7862 1.8211];
p_h_3MPa = polyfit(T,h_3MPa,n);
p_s_3MPa = polyfit(T,s_3MPa,n);

% Superheated vapor properties, P = P2
P3 = polyval(p_P_sat,T3);
P2 = P3;
if((P2>=1000)&&(P2<=1200))
    p_h_a = p_h_1MPa;
    p_h_b = p_h_12MPa;
    p_s_a = p_s_1MPa;
    p_s_b = p_s_12MPa;
elseif((P2>1200)&&(P2<=1400))
    p_h_a = p_h_12MPa;
    p_h_b = p_h_14MPa;
    p_s_a = p_s_12MPa;
    p_s_b = p_s_14MPa;
elseif((P2>1400)&&(P2<=1600))
    p_h_a = p_h_14MPa;
    p_h_b = p_h_16MPa;
    p_s_a = p_s_14MPa;
    p_s_b = p_s_16MPa;
elseif((P2>1600)&&(P2<=2000))
    p_h_a = p_h_16MPa;
    p_h_b = p_h_2MPa;
    p_s_a = p_s_16MPa;
    p_s_b = p_s_2MPa;
elseif((P2>2000)&&(P2<=3000))
    p_h_a = p_h_2MPa;
    p_h_b = p_h_3MPa;
    p_s_a = p_s_2MPa;
```

```
    p_s_b = p_s_3MPa;
else
    error('P2 out of bounds!');
end
h_P2 = ((P2-2000)/(3000-2000))*(polyval(p_h_b,T)-...
       polyval(p_h_a,T))+polyval(p_h_a,T);
s_P2 = ((P2-2000)/(3000-2000))*(polyval(p_s_b,T)-...
       polyval(p_s_a,T))+polyval(p_s_a,T);
p_h_P2 = polyfit(T,h_P2,n);
p_s_P2 = polyfit(T,s_P2,n);

%% Refrigeration Cycle Thermodynamic Calculations
% State 1
h1_conv = polyval(p_hg,T1_conv);
s1_conv = polyval(p_sg,T1_conv);
h1_prop = polyval(p_hg,T1_prop);
s1_prop = polyval(p_sg,T1_prop);

% State 2
s2s_conv = s1_conv;
s2s_prop = s1_prop;

p_s_P2_conv = ones(N,1)*p_s_P2;
p_s_P2_prop = ones(N,1)*p_s_P2;
p_s_P2_conv(:,n+1) = p_s_P2_conv(:,n+1)-s2s_conv;
p_s_P2_prop(:,n+1) = p_s_P2_prop(:,n+1)-s2s_prop;

T2_conv = zeros(N,1);
T2_prop = zeros(N,1);
for i = [1:1:N]
    T2_conv_tmp = roots(p_s_P2_conv(i,:));
    T2_conv(i)  = T2_conv_tmp(imag(T2_conv_tmp)==0);
    T2_prop_tmp = roots(p_s_P2_prop(i,:));
    T2_prop(i)  = T2_prop_tmp(imag(T2_prop_tmp)==0);
end

h2s_conv = polyval(p_h_P2,T2_conv);
h2s_prop = polyval(p_h_P2,T2_prop);

% Required compressor loads
Wc_conv = (h2s_conv-h1_conv)/eff;
Wc_prop = (h2s_prop-h1_prop)/eff;

% Compressor work ratio
wr = Wc_conv./Wc_prop*100;

% Eliminate numerical anomalies from wr vector
wr = wr.*(wr>=0).*(wr<100);
```